

UNIVERSITÀ DEGLI STUDI DI CAGLIARI



FACOLTÀ DI SCIENZE
SCUOLA DI DOTTORATO IN FISICA
XXIX CICLO

**MEASUREMENTS OF
THE ABSOLUTE BRANCHING FRACTION OF
 $\Lambda_c^+ \rightarrow pK^-\pi^+$
AND
THE RELATIVE BRANCHING FRACTION OF
 $B_u^+ \rightarrow p\pi^+\pi^+\bar{\Sigma}_c(2520)^{--}$**

SETTORE SCIENTIFICO DISCIPLINARE DI AFFERENZA: FIS/01

COORDINATORE DOTTORATO:
PROF. ALESSANDRO DE FALCO

PRESENTATA DA:
CLAUDIA VACCA

RELATORE:
PROF. BIAGIO SAITTA

ANNO ACCADEMICO 2015/2016

ABSTRACT

The baryonic decay $B_u^+ \rightarrow p\pi^+\pi^+\bar{\Sigma}_c(2455)^{--}$ is exploited in this thesis for two different measurements and constitutes their common element.

A measurement of the absolute $\Lambda_c^+ \rightarrow pK^-\pi^+$ branching fraction was performed, in a model independent way and for the first time in a hadronic environment, on data recorded by the LHCb experiment during the years 2011 and 2012, corresponding to an integrated luminosity of 3fb^{-1} . The branching fraction is measured to be

$$\mathcal{B}(\Lambda_c^+ \rightarrow pK^-\pi^+) = 0.079 \pm 0.015(\text{stat}) \pm 0.008(\text{syst})$$

In addition, the first observation of the decays $B_u^+ \rightarrow p\pi^+\pi^+\bar{\Sigma}_c(2520)^{--}$ and $B_u^+ \rightarrow p\pi^+\pi^-\bar{\Sigma}_c(2520)^0$ are reported using the same data sample. The branching fraction of the $B_u^+ \rightarrow p\pi^+\pi^+\bar{\Sigma}_c(2520)^{--}$ decay is measured with respect to the $B_u^+ \rightarrow p\pi^+\pi^+\bar{\Sigma}_c(2455)^{--}$ mode to be

$$\mathcal{B}(B_u \rightarrow p\pi^+\pi^+\bar{\Sigma}_c(2520)^{--}) = (2.4 \pm 0.78(\text{stat}) \pm 0.64(\text{syst})) \cdot 10^{-4}$$

CONTENTS

Preface	1
1 The LHCb experiment	3
1.1 The LHC accelerator	3
1.2 LHCb	4
1.2.1 VERTeX LOcator	6
1.2.2 Dipole magnet	7
1.2.3 Silicon Tracker	8
1.2.4 RICH	9
1.2.5 Calorimeters	10
1.2.6 Muon System	12
1.2.7 Trigger	13
1.2.8 Online system and computing	14
1.2.9 LHCb software	16
1.3 Global performance	18
2 Absolute branching fraction of $\Lambda_c \rightarrow pK\pi$	19
2.1 Analysis strategy	20
2.1.1 Determination of the absolute branching fraction	20
2.1.2 A novel method for Λ_c reconstruction	22
2.1.3 Advantages of the proposed decay chain	25
2.1.4 A two-fold ambiguity	25
2.2 Selection of signal events	27
2.2.1 Samples	27
2.2.2 Background contributions	29
2.2.3 Selection strategy	31
2.3 Signal extraction	40

2.3.1	Strategy	40
2.3.2	Fit	41
2.4	Efficiencies	53
2.4.1	Reconstruction efficiency of the Λ_c decay into $pK\pi$	57
2.4.2	PID efficiency	58
2.5	Systematic uncertainties	61
2.6	Results	62
2.6.1	Dependence on background lineshape	63
2.7	Conclusions	66
3	Relative BF of $B_u^+ \rightarrow p\pi^+\pi^+\bar{\Sigma}_c(2520)^{-}$	71
3.1	Analysis strategy	72
3.1.1	Determination of the relative branching ratio	72
3.2	Selection of signal events	73
3.2.1	Samples	73
3.2.2	Background contributions	75
3.2.3	Selection strategy	76
3.2.4	Data selected	81
3.3	Signal extraction	82
3.3.1	Strategy	82
3.3.2	Fit	82
3.4	Efficiencies	94
3.4.1	Acceptance, reconstruction and stripping efficiency	95
3.4.2	Selection efficiencies	95
3.5	Systematic uncertainties	98
3.5.1	L0 trigger	98
3.5.2	PID	98
3.5.3	Decay model	99
3.6	Results	100
3.7	Conclusions	101
A	LHCb variables definition	103
B	Boosted Decision Tree	105
C	Relativistic Breit Wigner function	125
D	Study on the low mass background region	127

LIST OF FIGURES

1.1	An illustration of the LHC ring.	3
1.2	The LHCb detector in the yz plane. The right-handed coordinate system used has the z axis along the beam direction pointing from the interaction point into the experiment, the y axis vertically upwards and the x axis pointing towards the outside of the LHC ring.	5
1.3	The VELO detector.	6
1.4	a) View of the LHCb dipole magnet (mm); b) Measured main parameters of the LHCb magnet.	7
1.5	The Tracker Turicensis and the T1-T3 stations. The Silicon Tracker is in purple, constituted by the TT and the IT, and the OT is in green.	9
1.6	Illustration of HCAL design.	11
1.7	Side view of the LHCb muon system.	13
1.8	The LHCb trigger.	13
1.9	The LHCb Computing Model.	16
1.10	Illustration of the classification of tracks.	16
2.1	Feynmann diagram for the decay $B_u(5279)^+ \rightarrow \bar{\Sigma}_c(2455)^{--} p \pi^+ \pi^+$	21
2.2	Scheme of the $B_u(5279)^+ \rightarrow \bar{\Sigma}_c(2455)^{--} p \pi^+ \pi^+$ total decay.	23
2.3	Distribution of m_3 VS m_4 for signal events.	26
2.4	$p\pi_1\pi_\Sigma$ invariant mass spectrum under the kaon mass hypothesis for the π_Σ , in 2011 sample.	30
2.5	$p\pi_1\pi_\Sigma$ invariant mass spectrum under the kaon mass hypothesis for the π_Σ , in 2012 sample.	31
2.6	ROC curve for 2011 [a] and 2012 [b] BDTs.	37
2.7	Comparison between $\Lambda_c\pi_\Sigma$ invariant mass spectrum obtained through the method presented before [a] and after reducing multiplicity to 1 [b] for 2011 sample.	39

2.8	Comparison between $\Lambda_c\pi\Sigma$ invariant mass spectrum obtained through the method presented before [a] and after reducing multiplicity to 1 [b] for 2012 sample.	40
2.9	Fit result obtained on Σ_c calculated mass spectrum for the $B_u^+ \rightarrow p\pi^+\pi^+\bar{\Sigma}_c(2455)^{--}$ 2011 [a] and 2012 [b] Montecarlo samples.	43
2.10	Fit result obtained on Σ_c calculated mass spectrum for the $B_u^+ \rightarrow p\pi^+\pi^+\bar{\Sigma}_c(2520)^{--}$ 2011 [a] and 2012 [b] MonteCarlo samples.	46
2.11	Fit result for PartReco line of MagUp [a] and MagDown [b] 2011 subsamples.	48
2.12	Fit result for PartReco line of MagUp [a] and MagDown [b] 2012 subsamples.	49
2.13	Fit result for PartReco line of 2011 [a] and 2012 [b] samples.	51
2.14	$\Lambda_c\pi\Sigma$ invariant mass spectrum obtained when the proposed method is applied to the FullReco line for the 2011+2012 sample, regardless of magnet polarity.	52
2.15	Fit result for FullReco line of MagUp [a] and MagDown [b] 2011 subsamples.	54
2.16	Fit result for FullReco line of MagUp [a] and MagDown [b] 2012 subsamples.	55
2.17	Fit result for FullReco line of 2011 [a] and 2012 [b] samples.	56
2.18	Proton P_T distribution for PartReco and FulReco samples in 2011 [a] and 2012 [b].	59
2.19	Proton η distribution for PartReco and FulReco samples in 2011 [a] and 2012 [b].	60
2.20	Fit result for PartReco line of MagUp [a] and MagDown [b] 2011 subsamples in the reduced mass range.	68
2.21	Fit result for PartReco line of MagUp [a] and MagDown [b] 2012 subsamples in the reduced mass range.	69
2.22	Fit result for PartReco lines of 2011 [a] and 2012 [b] samples in the reduced mass range quoted in the test.	70
3.1	ROC curve for 2011 [a] and 2012 [b] BDTs.	79
3.2	$p\pi^+\pi^+\bar{\Lambda}_c^-\pi^-$ invariant mass spectrum for the 2011+2012 data sample.	82
3.3	$\Lambda_c^+\pi^+$ invariant mass spectrum for the 2011+2012 data sample.	83
3.4	$\Lambda_c^+\pi^-$ invariant mass spectrum for the 2011+2012 data sample.	83
3.5	Fit result obtained on $p\pi^+\pi^+\bar{\Lambda}_c^-\pi^-$ invariant mass spectrum for the 2011+2012 Montecarlo sample.	84
3.6	Fit results on the $p\pi^+\pi^+\bar{\Lambda}_c^-\pi^-$ invariant mass spectrum for the 2011 and 2012 data samples.	85
3.7	Fit result obtained on $\bar{\Lambda}_c^-\pi^-$ invariant mass spectrum for the $B_u^+ \rightarrow p\pi^+\pi^+\bar{\Sigma}_c(2520)^{--}$ 2011+2012 Montecarlo sample.	87
3.8	$\bar{\Lambda}_c^-\pi^-$ invariant mass spectrum for the $B_u^+ \rightarrow p\pi^+\pi^+\bar{\Sigma}_c(2520)^{--}$ MonteCarlo events before (in red) and after (in blue) the application of Decay-Tree Fitter.	88
3.9	Fit result obtained on $\bar{\Lambda}_c^-\pi^-$ invariant mass spectrum for the $B_u^+ \rightarrow p\pi^+\pi^+\bar{\Sigma}_c(2455)^{--}$ 2011+2012 Montecarlo sample.	89

3.10	Fit result obtained on $\Lambda_c^+ \pi^+ \pi^- \bar{\Lambda}_c^-$ invariant mass spectrum for the $B_u^+ \rightarrow p\pi^+\pi^+\pi^-\bar{\Lambda}_c^-$ 2011+2012 Montecarlo sample.	90
3.11	Fit result obtained on $\Lambda_c^+ \pi^+ \pi^+$ invariant mass spectrum for the $B_u^+ \rightarrow p\pi^+\pi^+\bar{\Sigma}_c^0(2455)^0$ 2011+2012 Montecarlo sample.	91
3.12	Fit result obtained on $\Lambda_c^+ \pi^+ \pi^+$ invariant mass spectrum for the $B_u^+ \rightarrow p\pi^+\pi^+\bar{\Sigma}_c^0$ 2011+2012 Montecarlo sample.	91
3.13	Fit results for 2011 and 2012 samples.	93
3.14	Fit results for 2011 and 2012 samples shown in the reduced mass range [2420:2800] MeV/c ²	94
B.1	$\log(\pi_\Sigma$ impact parameter χ^2) distribution for PartReco and FulReco samples in 2011 [a] and 2012 [b].	106
B.2	$\log(p$ impact parameter χ^2) distribution for PartReco and FulReco samples in 2011 [a] and 2012 [b].	107
B.3	$\log(\pi_1$ impact parameter χ^2) distribution for PartReco and FulReco samples in 2011 [a] and 2012 [b].	108
B.4	$\log(\pi_2$ impact parameter χ^2) distribution for PartReco and FulReco samples in 2011 [a] and 2012 [b].	109
B.5	π_Σ P_T distribution for PartReco and FulReco samples in 2011 [a] and 2012 [b].	110
B.6	π_1 P_T distribution for PartReco and FulReco samples in 2011 [a] and 2012 [b].	111
B.7	π_2 P_T distribution for PartReco and FulReco samples in 2011 [a] and 2012 [b].	112
B.8	p P_T distribution for PartReco and FulReco samples in 2011 [a] and 2012 [b].	113
B.9	$\log(0.01+\text{acos}(p\pi\pi\pi_\Sigma \text{ DIRA}))$ distribution for PartReco and FulReco samples in 2011 [a] and 2012 [b].	114
B.10	$\log(0.01+\text{acos}(p\pi\pi \text{ DIRA}))$ distribution for PartReco and FulReco samples in 2011 [a] and 2012 [b].	115
B.11	$\log(3.5+\text{acos}(p\pi\pi\pi_\Sigma \text{ DIRA})-\text{acos}(p\pi\pi \text{ DIRA}))$ for PartReco and FulReco samples in 2011 [a] and 2012 [b].	116
B.12	$p\pi\pi\pi_\Sigma$ distance from primary vertex distribution on z-direction for PartReco and FulReco samples in 2011 [a] and 2012 [b].	117
B.13	$p\pi\pi$ distance from primary vertex distribution on z-direction for PartReco and FulReco samples in 2011 [a] and 2012 [b].	118
B.14	$\log(p\pi\pi\pi_\Sigma$ impact parameter χ^2) distribution for PartReco and FulReco samples in 2011 [a] and 2012 [b].	119
B.15	$p\pi\pi\pi_\Sigma$ vertex χ^2 distribution for PartReco and FulReco samples in 2011 [a] and 2012 [b].	120
B.16	$p\pi\pi$ vertex χ^2 distribution for PartReco and FulReco samples in 2011 [a] and 2012 [b].	121

B.17	$p\pi_1\pi_2 \chi^2$ flight distance distribution for PartReco and FulReco samples in 2011 [a] and 2012 [b].	122
B.18	$p\pi_1\pi_2 \chi^2$ flight distance from primary vertex distribution for PartReco and FulReco samples in 2011 [a] and 2012 [b].	123
B.19	$\log(p\pi_1\pi_2 \chi^2)$ flight distance from primary vertex distribution for PartReco and FulReco samples in 2011 [a] and 2012 [b].	124
D.1	Comparison between the $\Lambda_c^+\pi^+$ invariant mass distribution for the low mass background region [a] and the flat background region.	128
D.2	Comparison between the $\Lambda_c^+\pi^-$ invariant mass distribution for the low mass background region [a] and the flat background region.	129
D.3	Comparison between the Λ_c mass distribution for the signal region [a], the low mass background region [b] and the flat background region [c].	130

LIST OF TABLES

2.1	Signal events with relative best solution at stripping level or stripping and triggered selected.	27
2.2	Data samples used in the analysis.	28
2.3	MonteCarlo samples used in the analysis.	29
2.4	Absolute branching fractions of Λ_c with final state $pK\pi$ from PDG. . . .	29
2.5	Cuts applied in the stripping selection for the PartReco and PartReco WS/PartReco WS SC lines. An explanation for variables not defined at this stage and included in this table can be found in Appendix A.	33
2.6	Cuts applied in the stripping selection for the FullReco and FullReco WS/FullReco WS SC lines. An explanation for variables not defined at this stage and included in this table can be found in Appendix A.	34
2.7	Topological HLT2 three-body line efficiencies computed on FullReco line for 2011/2012 MagUp/Down samples. The efficiencies are relative to the number of events selected through PID, mass and pointing criteria.	35
2.8	Trigger selection requirements.	35
2.9	Variables used in the BDT.	36
2.10	Selection applied on PID variables.	38
2.11	Number of candidates per event in PartReco samples.	39
2.12	Fit parameters for 2011 and 2012 MonteCarlo signal events.	42
2.13	$B/(S+B)$, all candidates	44
2.14	Self-generated background after selection, 1 candidate per event	44
2.15	Parameters of the Double Crystal-Ball function for 2011 and 2012 MonteCarlo $\Sigma_c(2520)$ signal events.	45
2.16	Background fitted parameters.	47
2.17	Fit results on yields, obtained from simultaneous fitting.	47
2.18	Fit results on yields obtained on PartReco lines for the total 2011 and 2012 data samples.	50

2.19	Fit results on yields obtained on FullReco lines.	53
2.20	Fit results on yields obtained on FullReco lines for the total 2011 and 2012 samples.	53
2.21	Raw branching fractions.	53
2.22	Efficiencies of reconstruction of Λ_c decay into $pK\pi$ at different steps of the selection and, separately for different yeiers and magnet polarities.	58
2.23	PID efficiencies for three different binning schemes for 2011 subsamples.	61
2.24	PID efficiencies for three different binning schemes for 2012 subsamples.	61
2.25	PID efficiencies for three different binning schemes for 2011 subsamples.	62
2.26	PID efficiencies for three different binning schemes for 2012 subsamples.	62
2.27	Results on $\Lambda_c \rightarrow pK\pi$ branching fraction. The errors reported are purely statistical.	62
2.28	Results on $\Lambda_c \rightarrow pK\pi$ branching fraction. The errors reported are purely statistical.	63
2.29	Final results on branching fractions.	63
2.30	Fit results on yields obtained from simoultaneous fitting of the samples corresponding to different magnet polarities, for each year, in the limited mass range.	64
2.31	Fit results on yields obtained from separate fitting, in the limited mass range.	64
2.32	Background fitted parameters in the limited mass range.	64
2.33	Fit results on yields obtained on PartReco lines in the limited mass range.	64
2.34	Results on $\Lambda_c \rightarrow pK\pi$ branching fraction from fitting a reduced mass range. The errors reported are purely statistical.	65
2.35	Results on $\Lambda_c \rightarrow pK\pi$ branching fraction from fitting a reduced mass range. The errors reported are purely statistical.	65
2.36	Final results on 2011 and 2012 from fitting a reduced mass range.	66
3.1	Integrated luminosity corresponding to data analysed.	74
3.2	Absolute branching fractions of Λ_c with final state $pK\pi$ from PDG.	74
3.3	Signal events in filtered MonteCarlo samples.	75
3.4	Cuts applied in the stripping selection. An exhaustive explanation for variables not yet defined and contained in this table is available in Appendix A.	77
3.5	Trigger selection requirements.	77
3.6	Variables used in the BDT.	78
3.7	PID requirements on the protons.	80
3.8	Parameters of the Double Crystal-Ball function for 2011 and 2012 Monte-Carlo signal events. The first four parameters determine the shape of the tails, while the gaussian core is defined by the m and s parameters.	84
3.9	Yields result from a fit on the $p\pi^+\pi^+\bar{\Lambda}_c^-\pi^-$ invariant mass spectrum (B_u for the 2011 and 2012 samples.	86

3.10	Parameters of the Double Crystal-Ball function for 2011 and 2012 MonteCarlo $\Sigma_c(2520)^{++}$ signal events. The first four parameters determine the shape of the tails, while the gaussian core is defined by the m and s parameters.	87
3.11	Parameters of the Double Crystal-Ball function for 2011 and 2012 MonteCarlo $\Sigma_c(2455)^{++}$ signal events. The first four parameters determine the shape of the tails, while the gaussian core is defined by the m and s parameters.	88
3.12	Fitted parameters for the non resonant contribution.	89
3.13	Background fitted parameters.	90
3.14	Yields and raw relative branching fraction for 2011 and 2012 samples. The errors are from the fit.	92
3.15	Efficiency relative to acceptance, reconstruction and stripping selection for 2011 and 2012.	95
3.16	Relative selection efficiencies in 2011 sample.	96
3.17	Relative selection efficiencies in 2012 sample.	96
3.18	L0 trigger efficiencies extracted from MonteCarlo.	96
3.19	L0 trigger efficiencies extracted through the TISTOS method applied on data.	97
3.20	PID relative efficiencies for the different subsamples.	97
3.21	Trigger efficiencies extracted through the TISTOS method.	98
3.22	L0 trigger systematic uncertainties.	99
3.23	PID relative efficiencies obtained with three different binning schemes.	99
3.24	Relative systematic uncertainties related to PID.	99
3.25	Relative efficiencies computed varying the relative branching fractions of the channels through which the Λ_c is forced to decay into the final state $pK\pi$	100
3.26	Relative branching fraction for the 2011 and 2012 samples after the various corrections have been applied. The errors are purely statistical.	101
D.1	S/(S+B) ratio for the Λ_c mass distribution computed within $\pm 3\sigma$ from the Λ_c nominal mass, where the σ was obtained from the fitting of the distributions themselves.	127

PREFACE

The abundant production of charged B mesons at LHCb allows to analyse in detail many exclusive decay modes, including those containing baryon-antibaryon pairs, which have typical branching fractions of order $10^{-3} - 10^{-6}$.

$B_u^+ \rightarrow p\pi^+\pi^+\pi^-\bar{\Lambda}_c^-$ is the decay involving baryons that has the largest measured branching fraction [1]. This decay can occur through resonant channels involving the charmed baryon Σ_c neutral or doubly charged.

$B_u^+ \rightarrow p\pi^+\pi^+\bar{\Sigma}_c(2455)^{-}$ is the decay exploited in this thesis for two different measurements and constitutes their common element.

The absolute branching fraction of the $\Lambda_c \rightarrow pK\pi$ decay has been measured, in fact, for the first time in a hadronic environment, using a sample of Λ_c 's produced via this resonant decay of the B_u meson, taking advantage of a novel method recently proposed [2].

In addition, a measurement of the branching fraction of the $B_u^+ \rightarrow p\pi^+\pi^+\bar{\Sigma}_c(2520)^{-}$ decay, observed for the first time, has been performed with respect to the $B_u^+ \rightarrow p\pi^+\pi^+\bar{\Sigma}_c(2455)^{-}$.

This thesis is organised in the following manner.

A brief description of the LHC accelerator and of the LHCb detector is given in the Chapter 1.

The various sections of Chapter 2 describe in details the steps that led to the measurement of the absolute branching fraction of the decay $\Lambda_c \rightarrow pK\pi$, including a description of the method proposed, the selection of signal events, the techniques and tools employed, the analysis strategy and the results obtained.

Similarly, the sections of Chapter 3 deal with the measurement of the relative branching fraction of the $B_u^+ \rightarrow p\pi^+\pi^+\bar{\Sigma}_c(2520)^{-}$ decay, starting with the explanation of the analysis strategy, continuing with a description of the selection of the signal events and concluding with the results.

THE LHCb EXPERIMENT

The LHCb detector, its commissioning and performances will be presented in the following chapter.

1.1 The LHC accelerator

LHC - Large Hadron Collider is the world's largest and most powerful particle accelerator. It consists on a 27 km ring of superconducting magnets and accelerating structures, which guide and accelerate two high-energy particle beams (protons or heavy ions) in order to make them collide, at a depth from 50 to 175 m underground. The superconducting electromagnets need to operate at low temperature (-271.3°C), which is maintained by a distribution system of liquid helium.

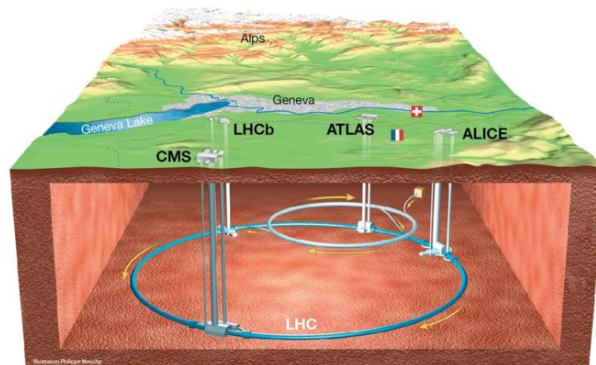


Figure 1.1: An illustration of the LHC ring.

At the design full power, LHC will accelerate protons up to 7 TeV (per beam), with a

collision energy of 14 TeV in the center of mass. Recently, an energy of 6.5 TeV per proton beam has been reached, during the so called Run II, in 2016. The designed luminosity is $10^{34} \text{ cm}^{-2} \text{ s}^{-1}$, with a bunch collision rate of 40 MHz.

Protons are generated at an energy of 50 MeV by a linear accelerator (LINAC2), feeding the Proton Synchrotron Booster (PSB), accelerated up to 1.4 GeV and then injected into the Proton Synchrotron, until they reach an energy of 26 GeV. The Super Proton Synchrotron accelerates them to 450 GeV, before they are finally injected into the main ring and accelerated to final energies.

The beams are made to collide at four locations, corresponding to the four detectors and experiments ATLAS [3], CMS [4], ALICE [5] and LHCb [6] (Fig1.1). At these locations the two adjacent and parallel beamlines, with two beams travelling in opposite directions around the ring, intersect. Each of these experiments has specific features, designed for the particular physics they propose to investigate. The next section will be focused on the LHCb detector and its peculiar aspects, with emphasis given to the subdetectors whose performance would be instrumental to the work described in this thesis.

1.2 LHCb

LHCb is an experiment designed to study the physics of heavy flavour. Its primary goals are precision measurements of the violation of the discrete symmetry CP and rare decays of hadrons containing beauty (b) and charm (c) quarks, in order to be potentially sensitive to effects due to physics beyond the Standard Model, commonly called "new physics".

An efficient and flexible trigger, an excellent vertex and momentum resolution together with good proper-time and invariant mass resolution, a data acquisition system with high bandwidth and powerful online data processing capability are the fundamental features that characterise the LHCb experiment and make its physics goals achievable.

LHCb is a single-arm spectrometer with a forward angular coverage ranging from 10 to 300 mrad in the bending plane and 10 to 250 mrad in the non-bending. High energies b and \bar{b} -hadrons are mostly produced in the same forward or backward cone, thus making natural that choice. A schematic view of the LHCb detector is shown in Figure 1.2.

Through LHCb, exclusive decays of the b- and c-hadrons are fully reconstructed in a variety of leptonic, semi-leptonic and purely hadronic final states. The detector incorporates different sub-detectors specialised to perform specific tasks with the aim to maximise the sensitivity to the physics of interest. On the basis of their primary aims they can be summarily classified into:

- **tracking system**, constituted from a precision vertex detector (the Vertex Locator - VELO), designed to provide a sufficient separation between primary and secondary vertices, and four planar tracking stations: the Tracker Turicensis (TT) located upstream of the dipole magnet and three tracking stations (T1-T3), located downstream of the magnet, which use silicon microstrips only in the region close to the beam (Inner Tracker), while the Outer Tracker is a straw-tubes based detector;

- **particle identification (PID)** system, composed by with two Ring Imaging Cherenkov detectors (RICH1 and RICH2), in order to discriminate between charged hadrons (particularly pions and kaons), the hadronic (HCAL) and electromagnetic (ECAL) calorimeters, and the Muon System, aimed to identify electrons, photons and muons, respectively.

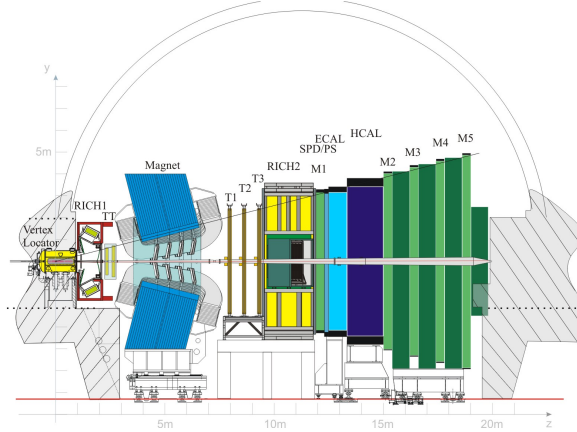


Figure 1.2: The LHCb detector in the yz plane. The right-handed coordinate system used has the z axis along the beam direction pointing from the interaction point into the experiment, the y axis vertically upwards and the x axis pointing towards the outside of the LHC ring.

The tracking system and the calorimeters are also responsible for the excellent invariant mass resolution, through precision energy and momentum estimates of reconstructed charged and neutral tracks, respectively.

- the **trigger and data acquisition system**, characterised by high flexibility in order to be able to comply with different physics aims and rapid changes in running conditions, and reducing the data rate from the initial $\sim 10\text{MHz}$ to about 3 kHz, suitable for offline storage.

As an example, the expected global performance for the reconstruction of B decays in the LHCb experiment is expected to be:

- a primary vertex resolution of $\sim 10\ \mu\text{m}$ in the directions transverse to the beam axis and $\sim 60\ \mu\text{m}$ along the beam axis;
- an invariant mass resolution between 12 and $25\ \text{MeV}/c^2$;
- a proper lifetime resolution of $\sim 40\ \text{fs}$, depending on the decay channel studied.

In the following subsections, a brief overview for each sub-system is presented, following their geometrical position starting from and downstream of the interaction point.

All the information reported has been taken from [6].

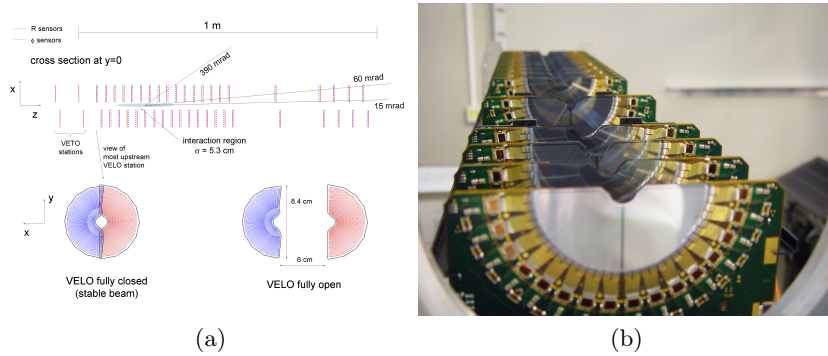


Figure 1.3: The VELO detector.

1.2.1 VERTeX LOcator

The VERTeX LOcator-VELO is a detector made of 21 planar modules placed perpendicularly to the beam line (lying within the xy plane), in a cylindrical symmetry environment, which use the silicon microstripes technology for precise measurements of track coordinates, very close to the interaction region. Its most important purpose is the identification of the displaced secondary vertices.

Each module provides a measurement of r and ϕ coordinates and the detectors are mounted in a vessel that maintains the same vacuum as the LHC beam pipe (10^{-8} mbar), in order to minimize the material traversed by particles prior to detection. Two additional sensor planes, the pile-up veto system, are located upstream of the VELO to provide information to allow rejection of events with multiple proton-proton interactions (pile-up veto system).

Detectors and readout electronics need to operate at low temperatures and also silicon modules need to be protected from radiation damage and kept at temperatures below -5°C , with a two-phase CO_2 cooling system. Being the environment where it operates only 8 mm from the LHC beam axis, the entire technology has been designed to be radiation tolerant. In fact, this radial distance from the beam is smaller than the one covered by the beam during injection. For this reason, it is possible to retract the two halves of the detector during the beams injection and ramping energy steps by 30 mm, until a condition of stable beams is achieved, thus protecting these fundamental delicate sensors. The positioning system can move the two halves with an accuracy of $10\ \mu\text{m}$ in order for the sensor positions to be optimised, on an individual fill basis, around the beam.

All tracks inside the LHCb acceptance ($1.6 < \eta < 4.9$, where η is the pseudorapidity) pass through at least three modules. The reconstruction in the VELO aimed for an initial S/N greater than 14 and an efficiency of 99% for a signal-to-noise ratio greater than 5. The best resolution obtained is $7\ \mu\text{m}$.

The VELO provides precision reconstruction of production and decay vertices of b - and c -hadrons and measurement of lifetimes and impact parameter of particles. The raw

VELO data are processed by a specific software, which also identifies clusters for use in the trigger and for off-line physics analysis.

1.2.2 Dipole magnet

A dipole magnet is placed downstream the VELO to allow the measurement of the momentum of charged particles, with a forward acceptance of ± 250 mrad vertically and ± 300 mrad horizontally. The field orientation is such that the deflection imposed by the Lorentz force bends tracks in the horizontal (xz) plane.

Since the aim of the LHCb experiment is to perform precision measurements of CP violation, it is essential to control the systematic introduced by the detector and its potential response asymmetries. This is partially achieved by changing periodically the direction of the magnetic field.

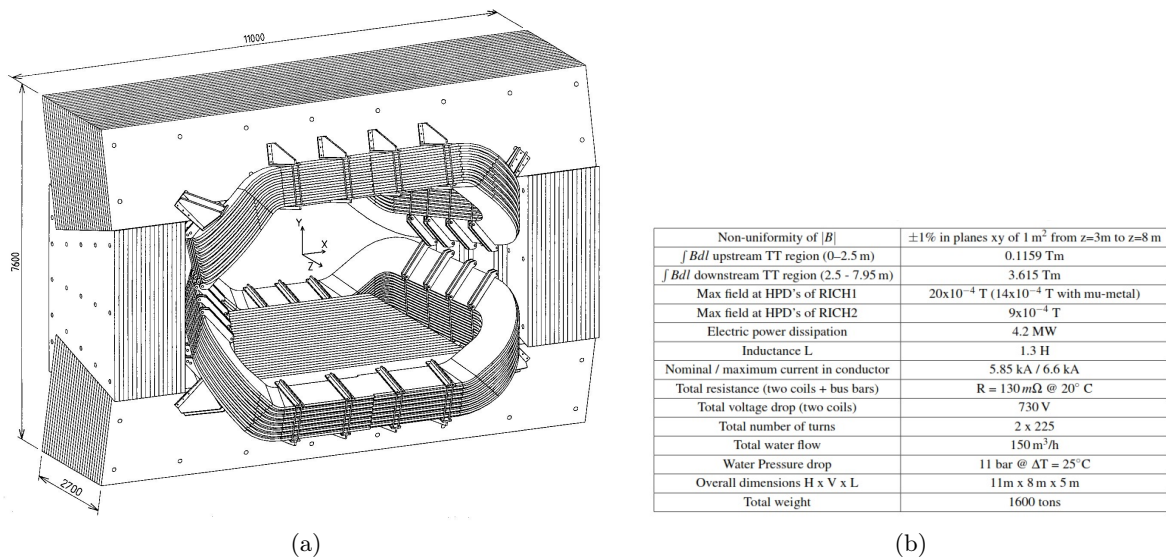


Figure 1.4: a) View of the LHCb dipole magnet (mm); b) Measured main parameters of the LHCb magnet.

It is a warm magnet constructed with conical saddle-shaped coils placed symmetrically to each other in a window-frame yoke. The coils are produced of pure Al-99.7 hollow conductor (single-length of about 320 m).

Its nominal current is of 5.85 kA and its total resistance is of $130 \text{ m}\Omega$ (20° C). The field whose maximum value is 1.1 T (on axis). The field has been finally measured in the tracking volume with a relative precision of $4 \cdot 10^{-4}$. Measured main parameters of the LHCb magnet are given in Figure 1.4-b.

1.2.3 Silicon Tracker

The Silicon tracker consists of the Tracker Turicensis (TT) and of the Inner Tracker (IT), with common readout electronics, power distribution, detector control and monitor systems. They exploit a technology based on a silicon microstrips, with a strip pitch of about $200\ \mu\text{m}$, in order to fulfil the high precision timing and resolution requirements due to high particles density in these regions.

Full particle detection efficiency is about 99.8% for signal-to-noise ratio above 10 and spatial resolution is about $50\ \mu\text{m}$ for both TT and IT.

TT

The Tracker Turicensis has an active area of $8.4\ \text{m}^2$, covers the entire acceptance of LHCb and is located upstream of the magnet. Four detection layers are maintained at temperatures below 5°C and in a light-tight, thermally and electrically insulated detector volume.

Hits in this detector are used to reconstruct trajectories of long-lived neutral particles that decay outside the fiducial volume of the VELO. Low momentum tracks steered out of the detector acceptance by the magnet before reaching the downstream tracking stations are also reconstructed through this detector.

IT The Inner Tracker constitutes the inner area of the T1-T3 stations, where particle flux is higher ($\sim 5 \cdot 10^5\ \text{cm}^{-2}\text{s}^{-1}$), downstream of the magnet. In fact, although this detector only covers 1.3% of the total active area of each tracking station, it is crossed by almost 20% of all charged tracks produced close to the interaction point and traversing the full tracking system.

Each of the three IT stations consists of four individual detector boxes arranged around the beam pipe. It has an active area of $4.0\ \text{m}^2$. Detectors are kept in the same light, thermal and electrical conditions as TT.

1.2.3.1 Outer Tracker

The Outer Tracker is a drift-time detector for the tracking of charged particles and the measurement of their momentum over a large acceptance area. This requires a momentum resolution of $\delta p/p \simeq 0.4\%$, that is essential for precision measurement of invariant mass, and an high tracking efficiency.

It is constituted by three stations of straw-tube modules, supported by aluminium structures. The tiny drift tube diameter (4.9 mm) and the gas mixture (70% Ar, 30% CO_2) allow for a drift time across the tube of less than 50 ns (two bunch crossings) which is the performance required by the tracking algorithms.

The greatest efficiencies and spatial resolutions are obtained for high voltage values above 1550 V (respectively larger than 99% and below $200\ \mu\text{m}$).

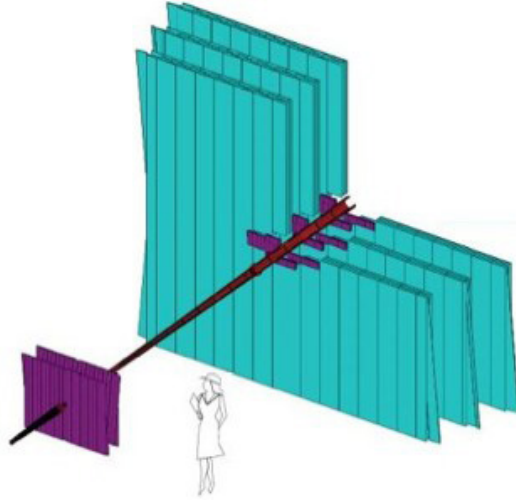


Figure 1.5: The Tracker Turicensis and the T1-T3 stations. The Silicon Tracker is in purple, constituted by the TT and the IT, and the OT is in green.

1.2.4 RICH

Particle identification is one of the main requirements and high performance features of the LHCb experiment. It plays an extremely important role in the separation of protons and pions from kaons in B hadron decays.

The two Ring Imaging Cherenkov (RICH) detectors exploit the Cherenkov effect to discriminate between charged particles, which emit photons passing through a medium of refraction index n with a velocity, v , larger than the speed of light in that medium ($v_{light} = c/n$). Photons are emitted along a cone with the opening angle, θ_c , given by $\cos\theta_c = 1/(\beta n)$, where $\beta = v/c$. Combining the measurement of the opening angle with the momentum measured by the tracking system, it is possible to calculate the particles' mass.

Since the response of these detectors depends on the medium, the two RICHs are filled with different materials, in order to cover the whole spectrum. The upstream one (RICH1) provides particle identification (PID) from $\sim 1\text{GeV}/c$ up to $60\text{GeV}/c$, while the spectrum range from $\sim 15\text{GeV}/c$ up to $100\text{GeV}/c$ is covered by the downstream detector RICH2.

In both RICH detectors Cherenkov light is focused by spherical and flat mirrors that reflect the image out of the spectrometer acceptance.

The RICH electronics system reads out data from about $5 \cdot 10^5$ channels of Hybrid Photon Detectors (HPDs), located either on-detector or housed behind the radiation-shield wall. The first group therefore must be radiation tolerant.

The system provides a resolution of 1.66 ± 0.03 mrad on the Cherenkov angle and as an example of its excellent performance, the average efficiency for K identification ($2\text{GeV}/c < p < 100\text{GeV}/c$) is $\simeq 95\%$ (97% around $30\text{GeV}/c$), with a corresponding average

pion misidentification rate ($\pi \rightarrow K$) $\simeq 5\%$.

The baseline algorithm matches the observed pattern of hit pixels in the RICH photodetectors to that expected from the reconstructed track under a given particle hypothesis. It is necessary to calculate the effective emission angle for all pixel-track combinations which could be associated through Cherenkov radiation. The likelihood is maximised by varying the particle hypothesis of each track. This method is known as the global-pattern recognition and its output is the best hypothesis for each track.

RICH1

The RICH1 detector covers the entire acceptance of LHCb. It contains aerogel (to cover the very difficult range of refractive indices between gas and liquid) and fluorobutane gaseous radiator. Cherenkov photons generated along the length of the trajectory of the charged particles are detected by HPDs, characterized by high speed and low dark-count rate, which detect visible light (200-600 nm). Since they operate in the fringe field of the LHCb dipole which is about 60 mT, a shielding structure is necessary to attenuate the field by a factor of about 20 to allow the HPDs to be fully efficient. In the HPDs, photoelectrons coming from conversion of an incident photon are accelerated by high voltages (10-20 kV) in vacuum.

RICH2

The RICH2 detector is located downstream of the last tracking station. It contains a tetrafluoromethane gas radiator and covers a limited acceptance of ± 120 mrad (horizontal) and ± 100 mrad (vertical). The HPDs need to be shielded as for the RICH1.

1.2.5 Calorimeters

The information coming from the two RICH detectors are combined with those coming from calorimeters and muon system to optimize identification of charged particles as e, μ, π, K, p , while photons and neutral pions are identified by the electromagnetic calorimeter.

The calorimeter system measures the transverse energy of hadron, electron, and photon candidates and is used in the first trigger level (L0). It identifies electrons, photons, and hadrons and provides measurements of their energies and positions. Its functions are essential for the study of B-meson hadronic decays. Because of the requirement of a good background rejection and reasonable efficiency, the detector has to have good resolution and electron-photon shower separation.

It is composed of an Electromagnetic Calorimeter (ECAL) to detect electrons and photons, followed by an Hadronic Calorimeter (HCAL) for charged and neutral hadrons. A pre-shower (PS) and scintillator pad detector (SPD) are located before the ECAL to discriminate electrons from the background of charged and neutral pions. All the detectors adopt a variable lateral segmentation since the hit density varies by two orders of magnitude over the whole surface. While ECAL and PS/SPD are segmented into three different sections, only two segmentations with larger cell sizes have been chosen

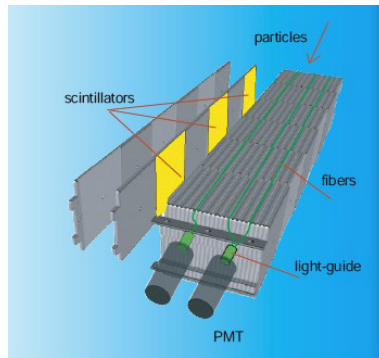


Figure 1.6: Illustration of HCAL design.

for HCAL, due to the dimensions of the hadronic showers. The whole calorimeter system is designed in order to achieve a one-to-one projective correspondence between single detectors segmentation in the x-y plane.

A schematic of this segmentation is shown in Figure 1.6

All calorimeters are of the sampling type, with alternating plates of absorbing material, lead or iron, and scintillating plates, with light transmitted by wavelength-shifting fibers to photomultipliers. A particle passing through or stopped in the absorber material deposits parts of its energy, released in the form of charged particles and photons and converted to photons in the scintillating material. The photons, proportional to the original particle's energy, conducted through wavelength-shifting fibres (WLS), are detected by photomultipliers.

SPD/PS

The SPD/PS detector consists of a $2.5 X_0$ lead converter between two planes of 15 mm-thick scintillator tiles. It is placed between the first muon station and the ECAL and has a sensitive area of 7.6 m x 6.2 m. The sizes of the PS are larger than the SPDs ones, owing to projectivity requirements. The information provided by SPD is used in order to separate electrons and photons at Level-0 trigger. Three main processes can contribute to photons mis-identification:

- photon conversion in the detector before SPD
- interactions in the SPD producing charged particles
- back-splash, charged particles generated in the lead or in the ECAL moving backward, with a measured probability of almost 1% of photon mis-identification for this effect.

The performance for electron/pion separation was tested at the CERN SPS with electron and pion beams of momenta of 10, 20 and 50 GeV/c and 91%, 92% and 97% electron retention were achieved, respectively, with corresponding 99.6%, 99.6% and 99.7% pion rejection factors.

ECAL

The ECAL is a sampling calorimeter formed of 66 alternating layers of lead absorber and scintillator (polystyrene) 2 mm and 4 mm thick, respectively, coupled to WLS fibres. The scintillator light is read out by phototubes. Each cell corresponds to a total thickness of $25 X_0$ in order to be able to fully contain showers of high energy photons.

It is placed at 12.5 m from the interaction point and covers an acceptance ± 300 mrad wide and ± 250 mrad high

HCAL

The HCAL is a sampling calorimeter made of iron and scintillating tiles, which run parallel to the beam axis and have a length equal to the hadron interaction length in steel in the longitudinal direction. The length of HCAL was chosen to be 5.6 interaction lengths. HCAL covers the same acceptance as ECAL. It is positioned at a distance of 13.3 m from the interaction point. The readout system is similar to ECAL's and it is equipped with a special device for calibration, capable to move a Cs^{137} gamma source of 10 mCi activity in front of each module. An absolute energy calibration and a cross-check of the ECAL calibration can also be performed.

1.2.6 Muon System

To be thorough, although the analyses presented in this dissertation do not deal with muons and information provided from the muon system, in this paragraph an overview of this sub-detector is briefly presented.

Since muons are present in the final states of many CP- and New Physics-sensitive B decays, the LHCb muon system provides essential information, such as muon triggering and offline identification.

The detector is composed of five stations (M1-M5), with M1 placed in front of the calorimeters and M2-M5 downstream, with angular acceptance ramping from 20 (16) mrad to 306 (258) mrad in the bending (non bending) plane. Stations M2-M5 are interleaved with 80 cm thick iron absorbers to select penetrating muons, which need to have a minimum momentum of 6 GeV/c to cross all the five stations.

The muon system provides space point measurements, through a rectangular partitioning in logical pads which define the resolution. Each station is divided into four regions with increasing distance from the beam, in order to obtain a particle flux and occupancy similar for all of them.

Multiwire proportional chambers (MWPC) are employed in all the regions except for the inner region of M1, where the MWPCs would suffer from ageing due to the high particles rate. This specific region uses instead triple-GEM detectors. The efficiency measured through specific test of this subdetector easily reaches and exceeds 98% in normal working conditions.

The muon trigger requires aligned hits in all five station and is based on single tracks.

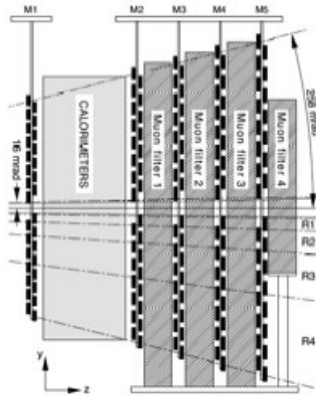


Figure 1.7: Side view of the LHCb muon system.

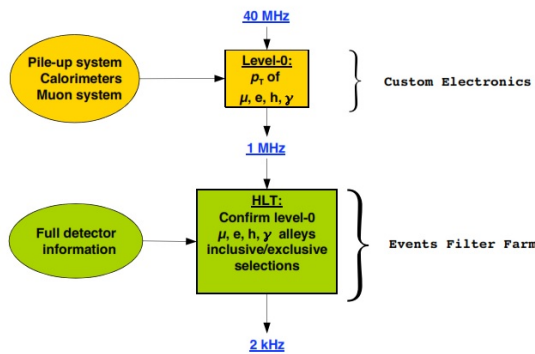


Figure 1.8: The LHCb trigger.

1.2.7 Trigger

The LHCb experiment operates at an average luminosity much lower than the maximum luminosity of the LHC. Moreover, it deals mostly with single interactions per bunch-crossing and this fact facilitates triggering and reconstruction. The crossing frequency with visible interactions (interactions are visible if produce at least two charged particles reconstructible by VELO and T1-T3) is about 10 MHz, but has to be reduced to the rate at which the events are written to storage for offline analysis (5 kHz). This function is fulfilled by a two level trigger.

Level-0 Trigger

Level-0 operates fully synchronously with the bunch crossing frequency(40 MHz). Its purpose is to reduce the beam crossing rate to the rate the entire detector can be read out (1 MHz). It attempts to reconstruct the highest transverse energy E_T hadron, electron and photon clusters and the two highest p_T muons. In particular, the Level-0 Trigger is

divided into three components:

- the L0-calorimeter trigger, which looks for high E_T electrons, photons, π^0 s or hadrons. It adds the energy of 2x2 cells and selects the clusters with the highest E_T , identifying them as electron, γ or hadron on the basis of the information produced by SPD/PS, ECAL and HCAL;

- the L0-muon trigger, selecting the two muons with the highest transverse momentum p_T for each quadrant of the muon detector;

- a pile-up system in the VELO estimates the number of the pp primary interactions for bunch crossing, while the calorimeters calculate the total observed energy and provide an estimate for the number of total track. It allows to reject events which would occupy an enormous fraction of the data-flow bandwidth and processing power.

If one of the above L0 trigger decisions is positive, the information of all sub-detectors is read out by the data acquisition system (DAQ). The L0-muon efficiency, estimated for $B \rightarrow J/\psi(\rightarrow \mu\mu)X$ decays, is around 70% for $p_T(J/\psi) \simeq 1$ GeV/c and more than 95% at $p_T(J/\psi) \simeq 4$ GeV/c.

The entire electronics of Level-0 is custom-designed to make the necessary calculations with sufficient speed.

High Level Trigger The second level, HTL (High Level Trigger), uses commercially available equipment instead and operates asynchronously on a processor farm. The HTL is fully implemented in software, very flexible and allows real data and physics driven modifications.

It reduces the rate to 3-5 kHz and processes all the events that pass the L0 trigger. It refines candidates selected by Level-0, requiring tracks with a combination of high p_T and/or large impact parameter.

It is divided into two subsequent stages, the HLT1 and the HLT2. The HLT1 performs a partial event reconstruction (L0-confirmation) to reduce the rate to 40-80 kHz and allow for full pattern reconstruction on the remaining events. The HLT2 reduces the rate to about 3 kHz in 2011 and about 5 kHz in 2012 by performing a combination of trigger algorithms to reconstruct partially or completely B decay events. The HLT2 output rate is the rate at which data are written to storage-media for offline physics analyses. It uses reconstruction algorithms close to the off-line reconstruction even though the timing requirements force them to be simplified.

Moreover, the physics analyses performed at LHCb exploit a variety of different and specific trigger configurations, called trigger lines, characterized by peculiar reconstruction methods and selection criteria.

1.2.8 Online system and computing

A relevant aspect of the LHCb experiment is the transfer of data from the front-end electronics to permanent storage. The online system serves this task and configures and monitors all operational and environmental parameters such as pressure or temperature. It must also ensure that all detector channels are properly synchronized with the LHC clock.

It consists of:

- the Data Acquisition (DAQ) system, which transport the data belonging to a precise bunch crossing identified by the trigger to permanent storage. It has a small number of components with simple functionalities, is able to react to changing system parameters;

- the Timing and Fast Control (TFC) system, which drives all stages of the data read-out of the detector between the front-end electronics and the online processing farm by distributing the L0 trigger, synchronous resets and fast control commands;

- the Experiment Control System (ECS), which controls and monitors the operational state of the entire detector.

The online system produces the raw data. The first step is to collect data. The raw data are transferred to the CERN Tier-0 centre for processing and archiving. Then they are reconstructed to provide physical quantities and the event reconstruction leads to the generation of new data, the Data Summary Tape, DST, to allow the physics pre-selection algorithms to be run at the next stage (reduced DST, rDST). Data are centrally reprocessed after the end of data taking for that year and then periodically as required, in order to produce streams of selected events for further individual analysis ("stripping").

The rDST informations are used to reconstruct the four-momentum vectors of measured particles, locate primary and secondary vertices and reconstruct composite particles. A pre-selection algorithm will be provided for each channel of interest. The events that pass the selection criteria will be fully reconstructed once more, in order to obtain the full information associated with each event. The output of the stripping stage contains more information than the rDST. Before storage, the selected events will have their raw data added in order to have more detailed event information for the analysis.

The events are also tagged for faster reference. The tag contains a brief summary of the characteristics of each event as well as the results of pre-selection algorithms and a reference to the actual DST record.

CERN is responsible for distributing the raw data to the Tier-1 centres. The raw data will be stored entirely at CERN with another copy distributed across the other 6 TIER-1 centres (CERN itself is a Tier-1 centre). The majority of the distributed analysis will be performed at CERN and the Tier-1 centres. Reconstruction and first stripping data will follow the production with a maximum delay of a few days. The DST output will remain on disk for analysis and distributed to the other Tier-1 centres and CERN. The raw and rDST are migrated to a mass storage system instead. The reprocessing of data will occur over a two-month period. During reprocessing the raw data are accessed from the mass storage at CERN and the Tier-1 centres. The Tier-2 centres are principally MonteCarlo production centres. The MonteCarlo production is expected to be ongoing throughout the year. The whole of the current year's MC production DST will be available on disk at CERN and another three copies distributed amongst the other Tier-1 centres.

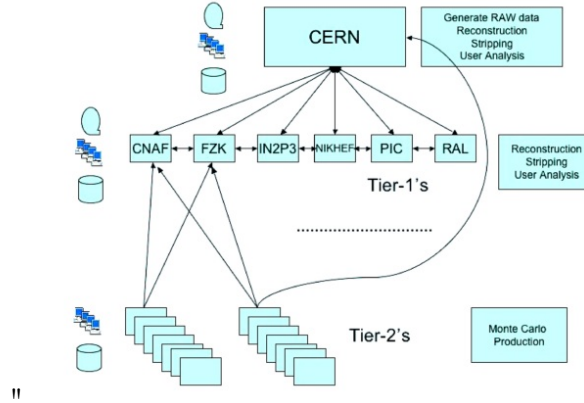


Figure 1.9: The LHCb Computing Model.

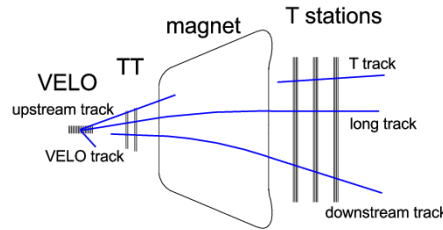


Figure 1.10: Illustration of the classification of tracks.

1.2.9 LHCb software

In the following, a brief description of the procedures for the very important tasks, such as tracking and particle identification within LHCb, is presented.

1.2.9.1 Tracking

In the tracks reconstruction software, the hits in the VELO, TT, IT and OT detectors are combined to form particle trajectories from VELO to calorimeters.

The track reconstruction starts with searching of the initial track candidates in the VELO and the T stations, where the magnetic field is low, allowing for a linear approximation. Their trajectories are then refitted with a Kalman filter, in order to account for multiple scattering and correct for the energy loss. The χ^2 of the fit is used to assess the track quality.

Tracks are classified as:

-**Long tracks**, traversing the full tracking setup. They are the most important tracks, with the most accurate momentum determination and will be the only used in this thesis.

-**Upstream tracks**, traversing only the VELO and the TT stations. They are generally lower momentum tracks bent out of the detector acceptance by the magnetic field.

They pass through RICH 1 detector and may generate photons. Their importance is linked to understanding backgrounds in the RICH particle identification algorithm.

-**Downstream tracks**, traversing only the TT and T stations (decay products of K_S^0 and Λ decaying outside the VELO acceptance).

The pattern recognition performance is evaluated on efficiencies (normalized to the reconstructible track samples) and ghost rates. A track is defined reconstructible if it presents a minimum number of hits in the subdetectors. If a track has at least 70% of its associated hits originating from a single MonteCarlo particle. The reconstruction efficiency is defined as the fraction of reconstructible tracks successfully reconstructed and the ghost rate is the fraction of reconstructed tracks not matched to a MonteCarlo particle.

The efficiency to find as a long track the trajectory of a particle with momentum larger than 10GeV/c is on average $\simeq 94\%$ and the ghost rate is $\simeq 9\%$. The momentum resolution of the reconstructed long tracks increases with momentum from $\delta p/p \simeq 0.35\%$ to 0.55%.

The efficiency of the upstream track finding for $p > 1$ GeV/c is approximately 75% and the momentum resolution is only of about 15%, while the ghost rate is 15%.

For downstream tracks above 5GeV/c efficiency is about 80% and the momentum resolution is good (0.43%).

-**VELO tracks**, measured in the VELO only, useful for the primary vertex reconstruction, typically large angle or backward tracks.

-**T tracks**, measured in the T stations, mainly produced in secondary interactions.

1.2.9.2 Particle identification

In LHCb charged particles (e, μ, π, K, p) are identified by combining the information from the RICH detectors, the calorimeters and the muon system, while neutrals and photons by using the electromagnetic calorimeter.

The hadron identification is performed with the RICH system, with a log-likelihood approach which matches the observed pattern of hits to that expected under a set of different particle hypotheses. This likelihood is maximised for each track by varying the hypothesis (global pattern-recognition).

Muons are instead identified by extrapolating well reconstructed tracks ($p > 3$ GeV/c).

For each track, hits are searched around the extrapolation point of the track in each station. A track is a candidate if it has suitable hits in a minimum number of stations (2-4 depending on momentum).

Concerning electrons, the identification is performed through the electromagnetic calorimeter, providing information on track momentum and energy of the charged cluster and the barycentre of the cluster itself corrected with the extrapolated track impact point. Moreover, bremsstrahlung photons are emitted by electrons, which are expected to create neutral clusters in well defined positions in ECAL, depending on the tracks extrapolation itself from before the magnet. Information provided by the PS and HCAL improve electron identification efficiencies, as well as RICH and muon detectors.

Photons are reconstructed and identified through ECAL information, as well as neutral pions.

1.3 Global performance

In summary, LHCb has:

- a primary vertex resolution of $\sim 10\mu m$ and $\sim 60\mu m$ transverse to and along the beam axis, respectively;

- an energy resolution of $\sigma_E/E = 10\%/E(\text{GeV}) \oplus 1\%$ for ECAL and $\sigma_E/E = (69 \pm 5)\%/E(\text{GeV}) \oplus (9 \pm 2)\%$ for HCAL, giving an invariant mass resolution between 12 and 25 MeV/c for B decays;

- a proper lifetime resolution of ~ 40 fs, depending on the decay channel.

ABSOLUTE BRANCHING FRACTION OF THE DECAY
 $\Lambda_c \rightarrow pK\pi$

Knowing the value of the absolute branching fraction of the $\Lambda_c \rightarrow pK\pi$ decay with good precision has become increasingly important with time.

In fact, not only all the other decay modes of the Λ_c , i.e. $\Lambda_c \rightarrow \Lambda e^+ \nu_e$, $\Lambda_c \rightarrow \Lambda \pi^+$, $\Lambda_c \rightarrow \Lambda \pi^+ \pi^+ \pi^-$, $\Lambda_c \rightarrow p \bar{K}^0$, are measured with respect to this, but also, since most of Λ_b decays contain a Λ_c in the final state (e.g. $\Lambda_b \rightarrow \Lambda_c^+ l^- \bar{\nu}_l$ or $\Lambda_b \rightarrow \Lambda_c^+ \pi^-$), the uncertainty on this value affects the measurements of these relative branching fractions.

Furthermore, it constitutes the major source of systematic error of many important measurements.

For instance, the results presented by the LHCb collaboration [7] in 2014 on b-hadron production fractions depend significantly on the value of $\Lambda_c \rightarrow pK\pi$ branching fraction, which causes an uncertainty on the final result one order of magnitude larger than those coming from the other statistical and systematic uncertainties.

Recently, a measurement of the CKM matrix element V_{ub} [8], which expresses the coupling strength of the u to the b quark, has received lots of attention. This measurement was carried out using the branching fraction of the decay $\Lambda_b^0 \rightarrow p \mu^- \bar{\nu}_\mu$ relative to $\Lambda_b^0 \rightarrow \Lambda_c^+ \mu^- \bar{\nu}_\mu$ and suffers from the poor knowledge (at the time, presently much better) of $\Lambda_c \rightarrow pK\pi$ branching fraction.

From an experimental point of view, until 2014 the results obtained were model dependent and the value quoted in the PDG [1] until that year was an average of two different results with an error of $\sim 26\%$.

Only recently, the Belle collaboration presented the first model independent measurement [9], performed by exploiting the recoil of the $D(*) \rightarrow \bar{p}\pi^+$ system in events of the type $e^+e^- \rightarrow D(*) \rightarrow \bar{p}\pi^+\Lambda_c^+$, with an accuracy of $\sim 4\%$.

In 2016, the Bes III collaboration measured the $\Lambda_c \rightarrow pK\pi$ branching fraction with a

precision of $\sim 5\%$. However, a discrepancy exists between the two central values given, whose average constitutes the value quoted in the current version of the PDG [1].

Given the importance of measuring accurately this branching fraction, a new method was proposed in 2014 [2], applicable in a hadronic environment.

Provided that a sufficient statistical precision can be reached, the result would be a valuable addition to the most recent measurements, since it is model independent as well.

Even though the measured branching fraction of the decay $B_u^+ \rightarrow \bar{\Sigma}_c(2455)^{--} p \pi^+ \pi^+$ is only $\sim 2.34 \cdot 10^{-4}$ the abundant production of charged B-mesons at LHC makes it possible to obtain samples containing $\mathcal{O}(10^7 - 10^8)$ decays of this type.

Taking advantage of the decay $\Sigma_c \rightarrow \Lambda_c \pi$, a measurement of the $\Lambda_c \rightarrow pK\pi$ absolute branching fraction could be obtained. This chapter describes the first application of the proposed method to real data and the results obtained.

2.1 Analysis strategy

The following sections will be dedicated to the explanation of the method and the strategy used for the determination of the absolute branching fraction.

2.1.1 Determination of the absolute branching fraction

The measurement presented exploits the decay $B_u(5279)^+ \rightarrow \bar{\Sigma}_c(2455)^{--} p \pi^+ \pi^+$, in which the baryon $\bar{\Sigma}_c^-$ decays via strong interactions into $\bar{\Lambda}_c^- \pi^-$, to obtain an unbiased sample of initial Λ_c s.

In particular, it is assumed that all charged particles in the decay are observed with the exception of the Λ_c . This assumption allows to infer the Λ_c and determine its momentum without need for actually reconstructing it by its decay products and thus obtain an unbiased sample of regardless of their decay mode.

In fact, the strong decay of the Σ_c into $\Lambda_c \pi$ is characterized by two important features listed below:

- the short life of the Σ_c , whose decay vertex is not detached with respect to B's one and allows to attach the π coming from its decay to the B vertex;
- the decay mode $\Sigma_c \rightarrow \Lambda_c \pi$, which is the only allowed, fix an univocal correspondence between the number of Σ_c s observed and the available sample of initial Λ_c s.

Once selected the sample of unbiased Λ_c s, one would simply search for the mode whose branching fraction is sought to be measured, thus in the specific $\Lambda_c \rightarrow pK\pi$.

From a purely conceptual side, the measurement is simply performed. Moreover, for the Λ_c s decaying in the mode of interest are a proper sub-sample of the initial one, allows a straightforward factorization of efficiencies, except those concerning direct requirements on Λ_c 's products.

Therefore, the raw numbers extracted from data have to be corrected as follows:

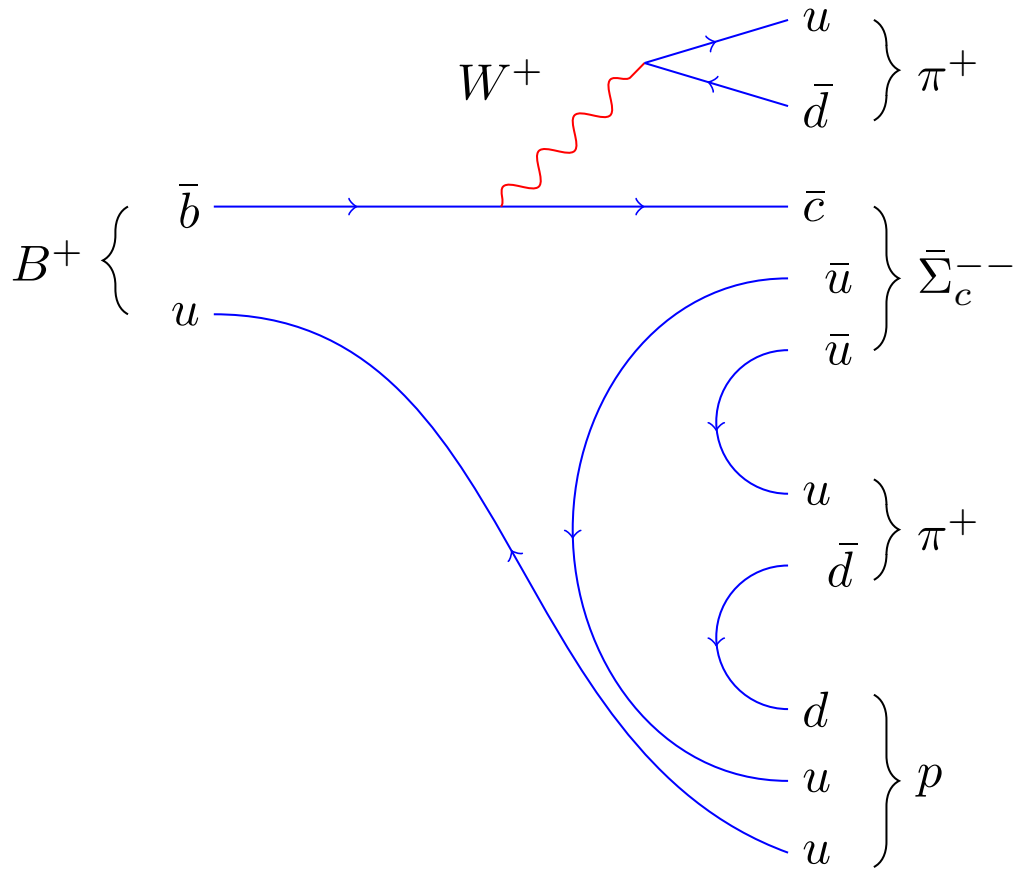


Figure 2.1: Feynmann diagram for the decay $B_u(5279)^+ \rightarrow \bar{\Sigma}_c(2455)^- p \pi^+ \pi^+$.

$$\mathcal{B}(\Lambda_c \rightarrow pK\pi) = \frac{N_{\Lambda_c \rightarrow pK\pi}^{FullReco}}{N_{\Lambda_c}^{PartReco}} \cdot \frac{1}{\epsilon_\Lambda} \quad (2.1)$$

where the factor ϵ_Λ , determined through MonteCarlo, includes the reconstruction efficiency for Λ_c decaying into $pK\pi$ and all the selection criteria applied exclusively to Λ_c 's products.

A check to ensure that the selection applied to the partially reconstructed events does not affect in a different way those containing a Λ_c decaying into $pK\pi$ is mandatory to exclude any possible bias.

2.1.2 A novel method for Λ_c reconstruction

In this thesis, the method originally proposed in [2] is used to measure the absolute branching fraction of the Λ_c decay into $Kp\pi$.

The current value of $6.35 \pm 0.33\%$ given in the PDG (see [1]) is the average of results obtained, in a model dependent way, by the CLEO [10] and the ARGUS [11] collaborations and more recently in a model independent way by the Belle [9] and the Bes III [12] collaborations.

In LHCb a large number ($\sim 10^{12}$) of B_u are produced per year. This suggests to use one of its decay modes as source of an unbiased sample of Λ_c decays and in particular, as already mentioned, $B_u(5279)^+ \rightarrow \bar{\Sigma}_c(2455)^{-} p\pi^+\pi^+$ in which the baryon $\bar{\Sigma}_c^{-}$ decays via strong interactions into $\bar{\Lambda}_c^-\pi^-$ appears to be suited for the purpose. The charge conjugate decay is considered as well throughout this work.

The decay vertex of the B_u^+ is identified by the presence of four charged particles (four-prong decay), specifically $p\pi^+\pi^+\pi^-$, hence its total charge is +2 and it is identified.

In addition, the π^- , i.e. the pion whose charge is opposite to the remaining three particles, is certainly a product of the strong $\bar{\Sigma}_c^{-}$ (Σ_c^{++}) decay (branching fraction 100%) and therefore originates from the B-decay vertex. Henceforth it will be referred to as π_Σ .

The $\bar{\Lambda}_c^-$ needs not to be observed directly.

The scheme of this decay is sketched in Figure 2.2.

The B_u flight direction (\hat{e}_B) is that defined by the line joining the B-decay vertex and the p-p interaction primary vertex in which the B_u^+ was produced.

At the four-prong decay vertex, the three particles directly produced from the B_u^+ , namely $p\pi^+\pi^+$, form a system of total momentum \vec{p}_3 , total energy E_3 and invariant mass $m_3 = \sqrt{E_3^2 - |\vec{p}_3|^2}$ (in the laboratory frame).

\vec{p}_4 , E_4 and $m_4 = \sqrt{E_4^2 - \vec{p}_4^2}$ are the corresponding quantities when all four charged particles are included.

Let E_4^* be the energy of this system in the B_u rest frame. The decay kinematics implies:

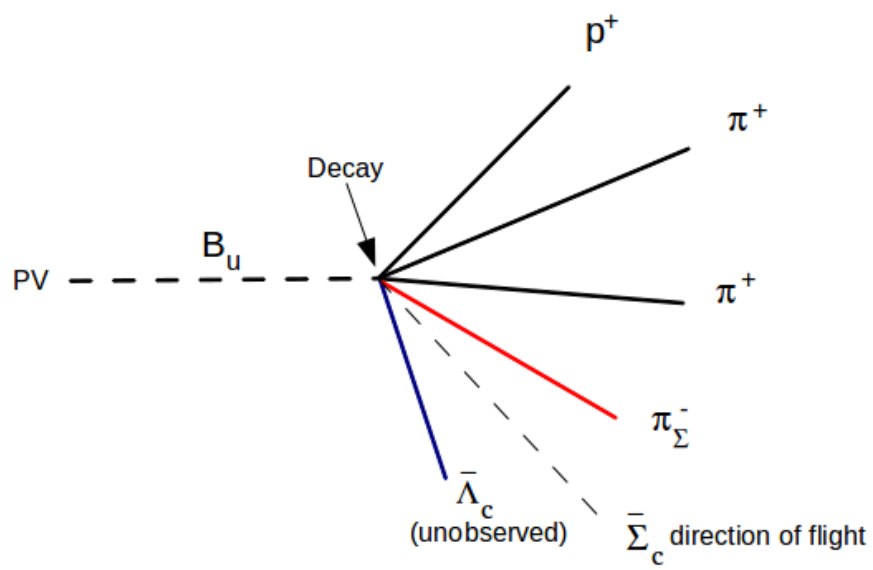


Figure 2.2: Scheme of the $B_u(5279)^+ \rightarrow \bar{\Sigma}_c(2455)^{-} p \pi^+ \pi^+$ total decay.

$$E_4^* = \frac{m_B^2 - m_\Lambda^2 + m_4^2}{2m_B} \quad (2.2)$$

On the other hand, momentum and energy in the laboratory and B_u^- rest frame are related by Lorentz transformations. In particular, the following relations hold:

$$\mathbf{p}_4^T = p_4^{*T} \quad (2.3)$$

$$\mathbf{p}_4^L = \gamma_B p_4^{*L} + \gamma_B \beta_B E_4^* \quad (2.4)$$

$$E_4 = \gamma_B E_4^* + \gamma_B \beta_B p_4^{*L} \quad (2.5)$$

where p_4^T and p_4^L are the transversal and longitudinal momentum relative to the B-flight direction respectively.

Multiplying eq.2.4 by p_4^L and eq.2.5 by E_4 and subtracting, it is obtained:

$$\gamma_B^{1,2} = \frac{E_4 \cdot E_4^* \mp |p_4^L| \cdot |p_4^{*L}|}{m_4^2 + |p_4^{*T}|^2} \quad (2.6)$$

Two solutions are obtained, depending on whether the four-particles system moves forward or backward in B rest frame. In this manner, two solution for the γ factor of the B_u are obtained and, as a consequence, two possible values of the B energy in the laboratory system and its four-momentum as indicated below.

$$E_B = \gamma_B \cdot m_B \quad (2.7)$$

Since the B flight direction is known (\hat{e}_B):

$$\vec{\mathbf{p}}_B = (E_B^2 - m_B^2) \cdot \hat{e}_B \quad (2.8)$$

and the B four-momentum will be:

$$p_B = (E_B, \vec{\mathbf{p}}_B) \quad (2.9)$$

Conservation of energy and momentum would thus determine, the Λ four-momentum:

$$p_\Lambda = p_B - p_4 \quad (2.10)$$

Therefore without the need to observe the decay products of the baryon, i.e. the Λ_c originated from the decay of a Σ_c , the quantity

$$p_\Sigma^2 = (p_\Lambda + p_{\pi_\Sigma})^2 \quad (2.11)$$

must be the Σ mass.

This constraint would allow the two-values ambiguity on the γ factor to be resolved, albeit, as it will be shown later, only partially.

In this manner, an unbiased sample of Λ_c could be selected without an actual observation of the decay of this particle.

Once this sample of Λ_c has been obtained, it would be sufficient to identify within it the decay mode $Kp\pi$ to obtain the absolute branching fraction.

2.1.3 Advantages of the proposed decay chain

There are other specific experimental advantages in using the suggested decay chain, some peculiar to LHCb:

- i) the four-prong decay vertex has charge ± 2 and it is relatively easy to identify;
- ii) there is a proton at this vertex and the experiment has very efficient particle identification capabilities. Furthermore, the charge of this proton is opposite to that of proton from the Λ decay;
- iii) the pion from the Σ has sign of charge opposite to the other three particles;
- iv) some kinematical boundaries can be applied in the selection of events.

In fact, if the final state from B_u^+ decay $\bar{\Lambda}_c^- \pi_\Sigma^- p \pi^+ \pi^+$ is reached via the resonance $\bar{\Sigma}_c^-$, the following limits between the invariant masses m_3 and m_4 must hold true:

$$(m_4^2)_{max} = (E'_3 + E'_{\pi_\Sigma})^2 - (\sqrt{E_3'^2 - m_3^2} - \sqrt{E_{\pi_\Sigma}'^2 - m_{\pi_\Sigma}^2})^2 \quad (2.12)$$

$$(m_4^2)_{min} = (E'_3 + E'_{\pi_\Sigma})^2 - (\sqrt{E_3'^2 - m_3^2} + \sqrt{E_{\pi_\Sigma}'^2 - m_{\pi_\Sigma}^2})^2 \quad (2.13)$$

where E'_3 and E'_{π_Σ} are the energy of the three-particles and of the π_Σ respectively in Σ rest frame.

This certainly would prove useful in the reduction of a possible background coming from the non resonant decay, which has a branching fraction 10 times larger and may produce interference effects with the resonant channel. However, since the method does not infer the presence of a $\Lambda_c \pi$ resonance, in principle any B_u decay with a $p \pi^+ \pi^+ \bar{\Lambda}_c^- \pi^-$ final state could be exploited in order to perform the measurement, provided a dedicated selection is tuned on this aim.

The distribution of masses for true events is shown in Figure 2.3, where the kinematical boundaries typical of this decay are clearly visible.

2.1.4 A two-fold ambiguity

As already pointed out, when applying this method, an ambiguity on the value of γ_B appears and this leads to two different possible values for the energy of the B_u meson. This ambiguity will be addressed in the following.

The origin of the two solutions is easy to understand; for the same value of $\vec{\mathbf{p}}_4^T$, the four-particles system may go forward ($\vec{\mathbf{p}}_4^L \cdot \vec{\mathbf{p}}_4^{*L} > 0$) or backward ($\vec{\mathbf{p}}_4^L \cdot \vec{\mathbf{p}}_4^{*L} < 0$) in the B rest frame with respect to the direction of flight of the B meson.

In the first instance the value obtained for the energy of the B would be smaller than that obtained in the second case. It is obvious that when $\vec{\mathbf{p}}_4^L \cdot \vec{\mathbf{p}}_4^{*L} > 0$ the Λ_c goes backward in the B centre of mass and vice versa.

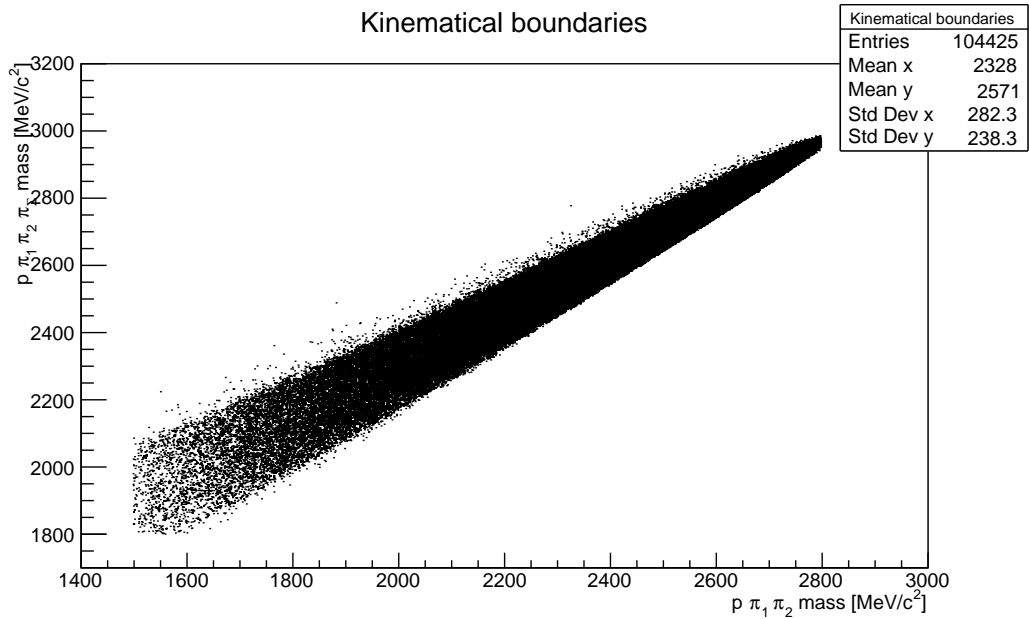


Figure 2.3: Distribution of m_3 VS m_4 for signal events.

For the purpose of this analysis, in order to simplify efficiencies calculations, it is easier to choose systematically one of the two possible solutions.

In view of this observation, it was investigated whether the specific geometrical environment of the LHCb detector and the selections applied favour systematically one of these solutions. As reported in [2], requiring the four tracks ($p\pi\pi\pi\Sigma$) to be within the LHCb acceptance and reconstructed would favour the second solution. However, the selection applied to data, i.e. kinematical selections on proton and pions momenta at "stripping" level and trigger requirements on the four tracks reconstructed, reverts this statement. Quantitative results obtained using MonteCarlo samples generated implementing the LHCb detector geometry and running conditions are reported in Table 2.1.

It is worth noticing that a sizeable fraction of Λ_c are emitted around $\theta \simeq \frac{\pi}{2}$ and therefore the choice of solution might be immaterial, since both will lead to a similar value for γ and thus consequently for the Σ mass.

In conclusion, the rather complex kinematic reconstruction interplay is such that, once the stripping and trigger selection is applied, for more than 85% (Tab.??) of the events the "first" solution (i.e. the one in which the Λ_c goes backward in the center-of-mass frame) is closer to the true value than the "second" (within $5 \text{ MeV}/c^2$) or coincides with it, making thus the obvious systematic choice between the two.

When the first solution is not the correct one, an effect of smearing of the Σ mass peak is observed, thus creating a background which broaden the distribution to values larger than the truth, since the kinematical threshold at $2424 \text{ MeV}/c$ prevents it to do the same in the lower mass region [2].

Sample	Selection	Best solution 1	Best solution 2	Solution 1 \simeq Solution 2
Up 2011	Stripping	1035	975	681
	Stripping+trigger	86	24	58
Down 2011	Stripping	951	850	645
	Stripping+trigger	91	16	56
Up 2012	Stripping	1955	1804	1377
	Stripping+trigger	166	45	116
2012	Stripping	2063	1818	1380
	Stripping+trigger	204	51	119

Table 2.1: Signal events with relative best solution at stripping level or stripping and triggered selected.

Sample	Events with solution 1 better or close to solution 2(%)
Up 2011	86%
Down 2011	90%
Up 2012	86%
Down 2012	86%

2.2 Selection of signal events

The most important step for each analysis is the definition of selection criteria aimed to enhance signal events over those that are not of interest, namely to efficiently suppress background contributions.

In Section 2.2.1 an overview of the samples exploited to perform the measurement is presented. Section 2.2.2 will be dedicated to the background contributions. Section 2.2.3 is focused on the selection strategy and the specific criteria applied to extract signal from background.

2.2.1 Samples

The analysis has been performed using data recorded in the LHCb detector in 2011 and 2012 at centre-of-mass energy of $\sqrt{s} = 7$ TeV and 8 TeV, respectively, with a total integrated luminosity of about 3 fb^{-1} .

Data

As mentioned in Section 1.2.2, the polarity of the magnet is reversed periodically. This feature allows a cross check between samples recorded under opposite magnet conditions and, for this reason, the analysis has been performed independently on four data samples, corresponding to the different years and polarities. Data recorded with magnet field pointing in the negative z-direction will be referred to as Magnet Down (MagDown) sample throughout this thesis, those with magnet field pointing in the positive z-direction

as Magnet Up (MagUp) sample. Table 2.2 shows in detail the integrated luminosity corresponding to the four samples.

Year	Polarity	Luminosity [pb^{-1}]
2011	Mag Up	413.012 ± 7.06251
2011	Mag Down	559.132 ± 9.56115
2012	Mag Up	936.522 ± 10.8637
2012	Mag Down	956.596 ± 11.0965

Table 2.2: Data samples used in the analysis.

MonteCarlo

Simulated samples, containing the number of generated events reported in Table 2.3, have been used to validate the method and the strategy, optimize the selection and estimate the efficiencies. About $2.1 \cdot 10^6$ pp interactions were generated, containing B_u , produced either directly or indirectly via the decay $B^* \rightarrow B_u\gamma$, in the ratio of 1:3. In all cases the B_u was forced to decay into the channel of interest, however the measurement does not depend on this absolute value.

The process simulated is:

$$B_u^+ \rightarrow \bar{\Sigma}_c^{--} p\pi^+\pi^+$$

with the subsequent decay:

$$\bar{\Sigma}_c^{--} \rightarrow \bar{\Lambda}_c^- \pi^-$$

and the momenta of the particles produced in the B_u decay follow a phase-space distribution.

The subsample of the events in which the tracks coming from the B (i.e. p , π , π) and the pion coming from the Σ_c decay were within the LHCb geometrical acceptance, were tracked through the detector and its response was simulated. No requirements instead were set for Λ_c decay products to fall within acceptance. In this manner, it is possible to extract directly and without any further step the reconstruction efficiency for the Λ_c s decaying into the mode of interest. Specifically, the Λ_c was forced to decay with a branching fraction of 100% in a final state $pK\pi$, via resonant or not resonant channels. The ratios imposed in MonteCarlo simulation are reported in Table 2.4 and reflect the values available in [1].

The events generated without tracking the charged particles trajectories in the detector will be referred to as "MC-generator level" events.

The Montecarlo samples called "MC-detector level" are instead constituted solely by events actually detected and reconstructed in the LHCb detector and which survive a selection very similar to that applied to data (see Section 2.2.3.1, "stripping"), except

Year	Polarity	Events Generated	Events detected (PartReco)	Events detected (FullReco)
2011	Mag Up	330k	23107	6729
2011	Mag Down	300k	20950	6051
2012	Mag Up	730k	46893	12985
2012	Mag Down	750k	48144	13326

Table 2.3: MonteCarlo samples used in the analysis.

for trigger and particle identification requirements. In fact, those efficiencies have to be calculated following a data-based strategy since it is not possible to rely completely on MC. This peculiar production is called "filtered Montecarlo", since it simulates and runs the tracking and the reconstruction only for the events which will survive the stripping selection (stripping filtered events), allowing to optimize time and computing resources. Nevertheless, this procedure requires a further step in order to access the reconstruction and stripping efficiencies, since information relative to the non-filtered events are not saved and therefore not available directly on simulation samples.

Mode	Branching fraction
$\Lambda_c^+ \rightarrow p\bar{K}^-\pi^+$	2.8%
$\Lambda_c^+ \rightarrow \Lambda(1520)\pi^+$	1.8%
$\Lambda_c^+ \rightarrow \Delta(1232)^{++}K^-$	0.86%
$\Lambda_c^+ \rightarrow p\bar{K}^*(892)^0$	1.6%

Table 2.4: Absolute branching fractions of Λ_c with final state $pK\pi$ from PDG.

It is important to notice that a single signal event generated, in principle, could yield more than one candidate at detector level, since it is possible for one or more tracks to be lost or misidentified. For this reasons, a set of information on the original and true values is available for each variable track in the MC at detector level, including true identity and origin.

2.2.2 Background contributions

Background is expected to come from four main sources, namely:

1. "mis-id" background
2. partially reconstructed background
3. "self-generated" background
4. combinatorial background.

As it will be explained in Section 2.2.3.4, some requirements on variables related to particle identification have been applied on the proton coming from the B_u , while no requirements have been imposed on pions. This allows specific background contributions (the **"mis-id" background**) due to the misidentification of one or more pions as kaons to be included in the selected sample.

Specifically, if the pion assumed to come from the Σ_c decay is in reality a misidentified kaon, the channel $\Lambda_c^+ \rightarrow pK^-\pi^+$ involving prompt Λ_c can constitute a non-negligible source of background, as shown in Figure 2.4. The $p\pi\pi_\Sigma$ invariant mass under the hypothesis that the π of same sign of charge as the proton is a kaon misidentified is shown in Figures 2.4 and 2.5 separately for the years 2011 and 2012. It is possible to produce such a background by combining the proton and the π_Σ with both the pions of same sign of charge as the proton. However, it was observed that among the two, the pion with higher momentum is more likely to give origin to such a background, and for this reason only this case is shown in the figures, where a signal corresponding to the Λ_c mass is clearly visible.

The "mis-id" component has been removed by applying a veto on the mass region involved.

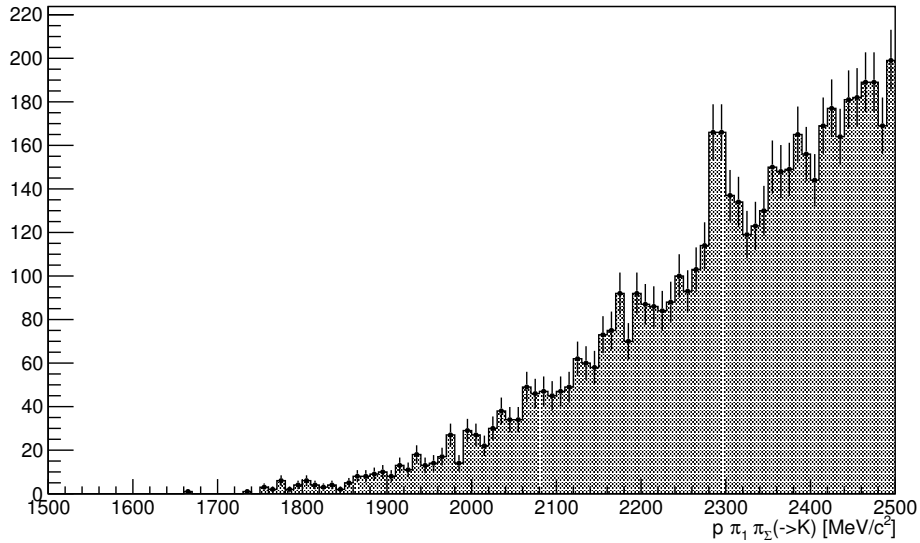


Figure 2.4: $p\pi_1\pi_2$ invariant mass spectrum under the kaon mass hypothesis for the π_Σ , in 2011 sample.

The **partially reconstructed background** is the contribution originated from decays of more massive particles with a loss of tracks and/or random re-combinations.

Combinatorial background comes instead from random combinations of tracks without a specific physical source and collects all candidates made of tracks randomly

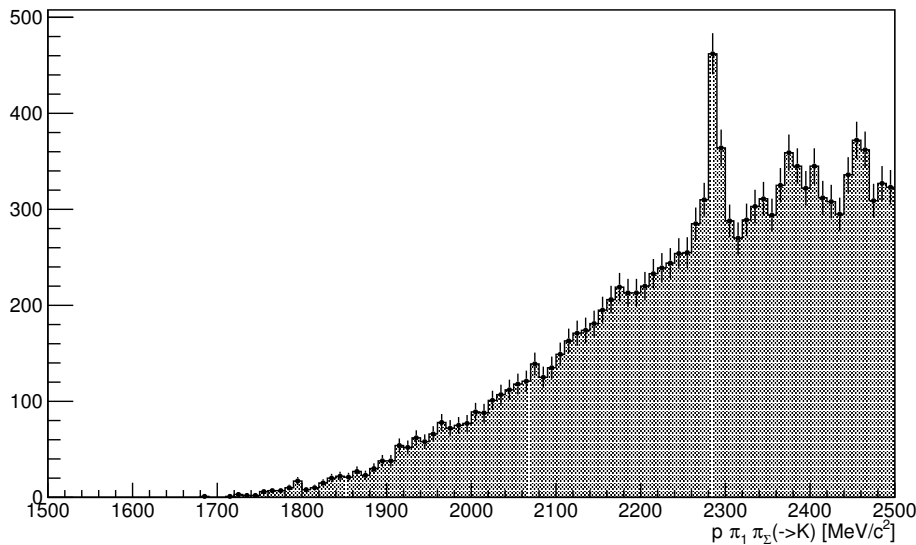


Figure 2.5: $p\pi_1\pi_\Sigma$ invariant mass spectrum under the kaon mass hypothesis for the π_Σ , in 2012 sample.

combined and external to the decay. This process in principle can originate a multiplicity of false candidates per event, when all tracks are detected, or single, fake candidates if one or more than one particles have been lost.

If instead a B_u is produced and decays into the channel of interest, it is possible to select candidates in which not all tracks originate from the signal event. This source of background is called "**self-generated**" and specific studies have been performed through the MonteCarlo sample and will be reported in Section 2.3.2.

2.2.3 Selection strategy

The main aim of this analysis is to select an unbiased sample of Λ_c 's and thus the whole selection strategy is tuned to minimize any bias and to be as much as possible independent of the decay mode.

The selection has been tested on simulated samples, to ensure that the efficiencies remain unchanged, irrespective of whether the Λ_c decays into $pK\pi$ or any other mode.

The candidates are selected through four main stages, which will be explained in what follows:

1. Stripping selection (see Section 2.2.3.1);
2. Kinematical boundaries (see Section 2.1.3);
3. Trigger selection (see Section 2.2.3.2);

4. Multivariate Boosted Decision Tree (BDT) selection (see Section 2.2.3.3);
5. PID selection (see Section 2.2.3.4);
6. Multiplicity of candidates (see Section 2.2.3.5).

2.2.3.1 Stripping Selection

Within LHCb, the first step of each analysis is the definition of selection requirements - the so-called *stripping selection* - to extract events of interest from the huge files produced by the reconstruction software, in order to obtain smaller and more manageable files which can be processed by single users without the need of prohibitive computing resources. It is possible to choose what information has to be stored and the format can be customised on the basis of the effective need of the specific analysis.

In this section, an overview on the stripping selection criteria proper of this analysis is given, as well as the description of the different *lines* and the specific samples they select.

Six stripping selection lines are implemented and used. Two of them are signal lines, while the remaining four are background lines, which are used to investigate combinatorial backgrounds.

- **signal**

- *Partially Reconstructed Line (PartReco)*: selection of candidates with $p\pi^+\pi^+\pi_{\Sigma_c}^-$ forming a vertex
- *Completely Reconstructed Line (FullReco)*: run on the events already selected by the PartReco, isolating therefore a subsample of its candidates. It requires in addition a $\bar{\Lambda}_c \rightarrow \bar{p}K^+\pi^-$ candidate to be reconstructed.

- **background**

- *Partially Reconstructed Wrong Sign Line (PartReco WS)*: selection of $p\pi^+\pi^+\pi_{\Sigma_c}^+$ candidates forming a vertex. These candidates have total charge opposite to signal ones (± 4).
- *Partially Reconstructed Wrong Sign Same Charge Line (PartReco WS SC)*: selection of $p\pi^-\pi^-\pi_{\Sigma_c}^-$ candidates forming a vertex. These candidates have same total charge as signal ones (± 2)
- *Completely Reconstructed Wrong Sign Line (FullRecoWS)*: run on the events selected by the PartRecoWS, requiring in addition a $\bar{\Lambda}_c^- \rightarrow \bar{p}K^+\pi^-$ candidate to be reconstructed
- *Completely Reconstructed Wrong Sign Same Charge Line (FullRecoWS SC)*: run on the events selected by the PartRecoWS SC, requiring in addition a $\bar{\Lambda}_c^- \rightarrow \bar{p}K^+\pi^-$ candidate to be reconstructed

The "FullReco" lines consists of appropriate subsets of samples already selected by the corresponding PartReco lines. This feature ensures the factorization of efficiencies, once it has been proven that the selection does not introduce a bias depending on the decay mode of the Λ_c .

The criteria applied at the stripping level are listed in Tables 2.5 and 2.6.

Candidate	Variable	Cut
B daughters	proton P	> 10 GeV
	proton minimum IP χ^2	> 8
	proton P_T	> 500 MeV
	proton PID($p - \pi$)	> 5
	proton PID($p - K$)	> -5
	$\pi_{1,2}$ p	> 5 GeV
	$\pi_{1,2}$ P_T	> 400 MeV
	$\pi_{1,2}$ minimum IP χ^2	> 8
	$\pi_{1,2}$ track ghost probability	< 0.3
$p\pi^+\pi^+$ candidate	invariant mass	1.5 – 2.8 GeV
	DOCAMAX	= 0.15 mm
	χ^2 VNDOF	< 5
	FD χ^2	> 49
	minimum IP χ^2	> 6
	P_T	> 1 GeV
π_{Σ_c}	p	> 2 GeV
	P_T	> 150 MeV
	minimum IP χ^2	> 8
$p\pi^+\pi^+\pi_{\Sigma_c}$ candidate	invariant mass	1.8 – 3 GeV
	DOCAMAX	= 0.15 mm
	χ^2 VNDOF	< 5
	FD χ^2	> 49
	minimum IP χ^2	> 6
	P_T	> 1 GeV

Table 2.5: Cuts applied in the stripping selection for the PartReco and PartReco WS/PartReco WS SC lines. An explanation for variables not defined at this stage and included in this table can be found in Appendix A.

HLT2 global trigger requirement on the $p \pi_1 \pi_2 \pi_{\Sigma_c}$ is also included in the stripping selection (*HLT2_PhysDecision_TOS*) and all tracks inherit global cuts such as track χ^2 less than 3.

2.2.3.2 Trigger requirements

The LHCb trigger has three major sections, one hardware (L0) and two software (HLT1 and HLT2).

Candidate	Variable	Cut
B_u	mass window	± 200 MeV
	DOCAMAX	= 0.2 mm
	χ^2 VNDOF	< 5 5.0
	FD χ^2	> 64
	DIRA	> 0.998
Λ_c	mass window	± 100 MeV
	FD χ^2	> 36
	χ^2 VNDOF	< 5.0
	DIRA	> 0.98
	DOCAMAX	= 0.5 mm
	P_T	> 0 GeV
Λ_c daughters	p	> 2 GeV
	P_T	> 250 MeV
	minimum IP χ^2	> 8
	proton PID($p - \pi$)	> -5
	kaon PID($K - \pi$)	> -5

Table 2.6: Cuts applied in the stripping selection for the FullReco and FullReco WS/FullReco WS SC lines. An explanation for variables not defined at this stage and included in this table can be found in Appendix A.

For this analysis the so-called L0 hadronic channel was used while for HLT2 the two- and three-body topological trigger line conditions were required to be fulfilled by one or more of the four particles $p\pi^+\pi^+\pi^-$ detected in the PartReco line. This is known as Trigger On Signal (TOS) requirement, meaning that the presence of the signal is sufficient to generate a positive trigger decision.

Events triggered by "HLT2 three-body topological" line are also explicitly excluded, if the requirement is set on the three particles $p\pi^+\pi^+$ coming directly from the B_u .

In fact non negligible differences within data samples corresponding to different magnet polarities were observed when the HLT2 three-body line triggered on the four particles and specific studies performed on data allowed to isolate this effect. In fact, an enhancement of this asymmetry was observed when the particles involved were the $p\pi^+\pi^+$, i.e. when the three particles triggering the three-body topological line had the same charge.

The numerical results are shown in Table 2.7. Although the statistical errors are large, there is a detectable a general trend showing an asymmetry which depends on the polarity of the magnet and on the sign of charge of the three particles.

Since this charge-related effect is not reproduced at all in the simulation, it would not be possible to correct for these differences through efficiencies computed using Monte-Carlo samples and therefore it was decided to put a veto on these specific configurations.

The TOS requirements made on the data sample are listed in Table 2.8.

Sample	Total	Positive	Negative
MagUp 2011	0.16±0.03	0.14±0.04	0.19±0.05
MagDown 2011	0.12±0.02	0.14±0.03	0.09±0.02
MagUp 2012	0.17±0.02	0.13±0.02	0.22±0.03
MagDown 2012	0.18±0.04	0.22±0.06	0.14±0.05

Table 2.7: Topological HLT2 three-body line efficiencies computed on FullReco line for 2011/2012 MagUp/Down samples. The efficiencies are relative to the number of events selected through PID, mass and pointing criteria.

Trigger Level	Requirement on $p\pi_1\pi_2\pi_\Sigma$	Requirement on $p\pi_1\pi_2$
L0	L0Hadron_TOS	
HLT1	Hlt1TrackAllL0_TOS	
HLT2	(Hlt2Topo2BodyBBDTDecision_TOS Hlt2Topo3BodyBBDTDecision_TOS)	!Hlt2Topo3BodyBBDTDecision_TOS

Table 2.8: Trigger selection requirements.

2.2.3.3 Multivariate selection

In high energy particle physics, very often one is faced with the problem of extracting rare events and isolate small fractions of signals of interest out of an enormous amount of data recorded.

This task is carried out through advanced and powerful analysis methods, based on statistical tools, which are under continuous development, in order to obtain higher performance.

The analysis presented in this thesis takes advantage of a multivariate method based on BDT (Boosted Decision Tree) [13], through a dedicated toolkit available in ROOT [14], namely Toolkit for Multivariate Analysis (TMVA) [15]. Methods of this kind are based on the observation and simultaneous analysis of many variables, taking into account the correlation between them and their combined effect with respect to the specific goal.

Through studies performed in multiple dimensions, these tools are able to learn from models how to reach an high power of discrimination between events of interest or not, giving as output a single indicator which contains, summarised, the whole information elaborated. Boosted decision trees allow a better separation than when considering a set of variables independently and make correlations visible.

A tree is structured as a consecutive set of questions (nodes) with only two possible answers. Each question depends on the formerly given answers and is aimed to enhance the separation between signal and background and the final verdict (leaf) is reached after a given maximum number of nodes.

A decision tree needs to be trained on a dataset which already provides the outcome, e.g. a MonteCarlo dataset for signal and/or background. The sequence of nodes is

Candidate	Variable
$p\pi^+\pi^+$	vertex χ^2 NDOF FD χ^2 oriv FD oriv FD χ^2 ownpv FD ownpv DIRA max/min P_T of three max/min IP χ^2 of three distance from primary vertex
π_Σ	P_T minimum IP χ^2
$p\pi^+\pi^+\pi_{\Sigma_c}$ candidate	vertex χ^2 NDOF IP χ^2 DIRA distance from primary vertex

Table 2.9: Variables used in the BDT.

automatically chosen in order to maximise the separation gain g defined as:

$$g = I(\text{parent}) - I(\text{daughter A}) - I(\text{daughter B})$$

where I is an index gain and can be defined as:

$$I = p \cdot (1 - p)$$

with p the purity of the cell.

Since BDTs learn by heart from training samples, it could happen that a statistical fluctuation is interpreted as a proper characteristic of the sample (*overtraining*). In order to avoid this drawback, a different data sample is used to test the method in order to ensure that performance on the training sample is not better than on the test sample.

A measure of a BDTs performance is the Receiver Operating Characteristic curve, which shows the efficiency in preserving signal with respect to that of rejecting background events.

In this analysis, a BDT has been implemented to remove most of the combinatorial background. Only observables present in the PartReco line have been used to train the BDT, not to introduce bias in the selection of events with a Λ_c decaying into $pK\pi$.

The training sample for signal was a MonteCarlo with requirements on the true identity and correct lineage of tracks, while the BDT was trained for background on PartReco WS SC Line with same requirements as signal on HLT2 trigger, in order to be similar to the combinatorial background in the PartRecoLine and at the same time assuring that no signal events were included.

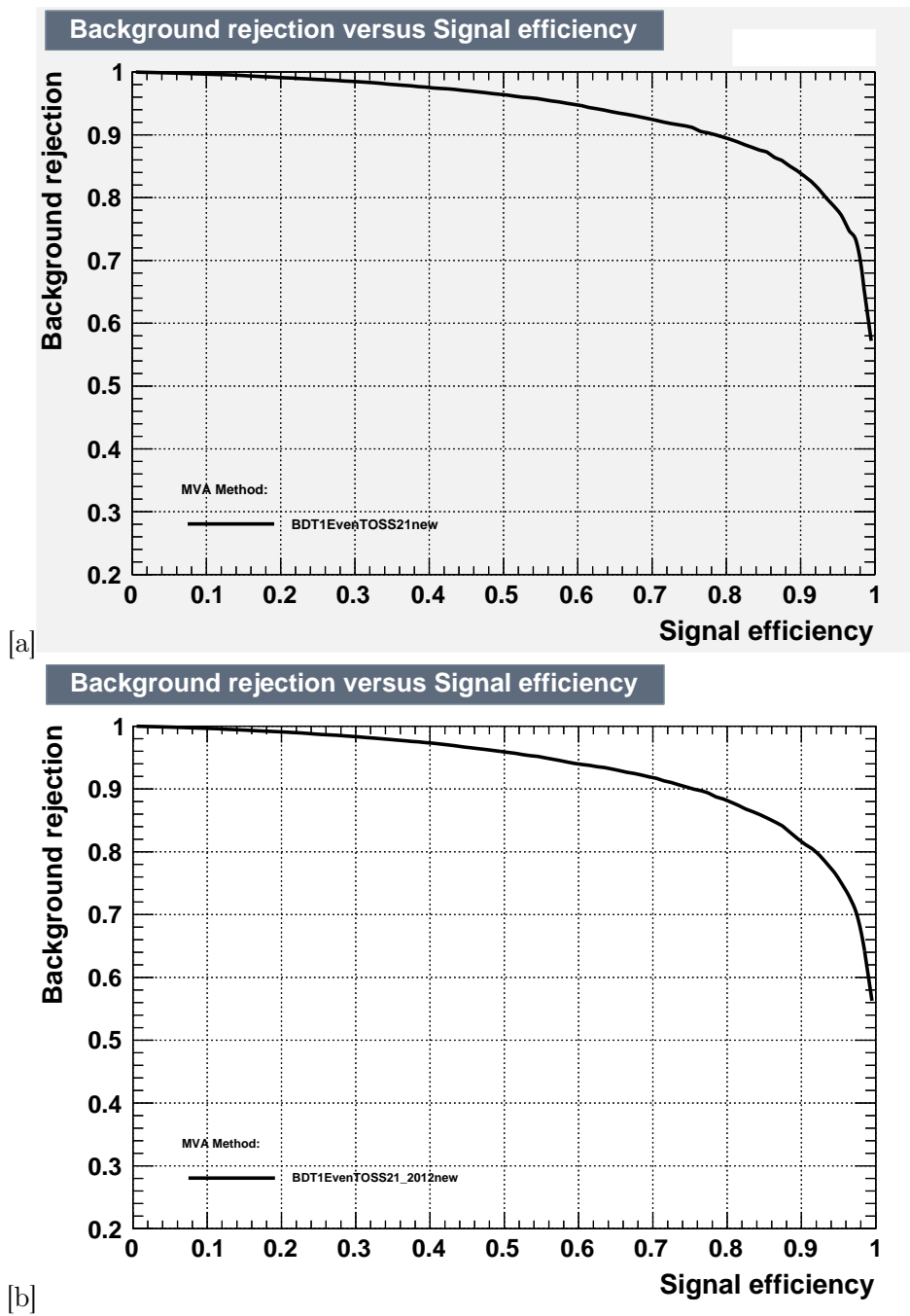


Figure 2.6: ROC curve for 2011 [a] and 2012 [b] BDTs.

Since 2011 and 2012 background distributions are expected to be different, two different BDTs have been implemented for the two years, tuned and trained on appropriate

MC and data samples. This leads to a different efficiency, and consequently to different cuts.

In order to avoid the *overtraining* without losing statistics, two different BDTs based on the same variables have been used. One is trained on candidates with an even event number and tuned on those with an odd even number, the other vice versa. When running over data to obtain the BDTs final value, the first is used on "odd" candidates, the second on "even".

The ROC curve of the BDT used to select 2011 and 2012 data in this analysis is shown in Figure 2.6.

The same BDT is also applied to the fully reconstructed candidates after stripping. The variables used in the BDT are listed in Table 2.9. A comparison of these variables for MC signal in the partially and fully reconstructed lines is shown in Appendix B. It is worth observing that the two samples have very similar distributions and this ensures an unbiased selection with respect to the decay mode of interest.

The cut on BDT variable has been chosen in order to allow a sufficient suppression of background in the PartReco line, and the maximum values have been fixed to -0.1 for 2011 sample and 0. for 2012.

2.2.3.4 Particle Identification

Since candidates are selected by requiring primarily the presence of a proton, some PID cuts are applied to particles of this type coming from the B_u .

In addition, some PID requirements are also set for the protons and kaons coming from the Λ_c , for the Fully reconstructed line.

The complete set of PID cuts applied are summarised in Table 2.10

Sample	p	p_{Λ_c}	K_{Λ_c}
PartRecoLine	PIDp>20. (PIDp-PIDK)>10.	-	-
FullRecoLine	PIDp>20. (PIDp-PIDK)>10.	PIDp>5.	PIDK>5.

Table 2.10: Selection applied on PID variables.

Among all the available choices of algorithms, the selection has been performed through variables based on the maximisation of likelihood for the various mass hypotheses. For pions and protons, this likelihood is built by exploiting the information obtained by the RICH, CALO, and Muon systems (Section 1.2.4, 1.2.5, 1.2.6). For each track and each system, starting from a pion mass hypothesis, a likelihood is re-calculated under a different identity assumption and the hypothesis maximising the likelihood assigns the new identity to the charged particle trajectory. The value considered is then the product of the likelihoods from the different subsystems.

2.2.3.5 Multiple candidates

If more than one candidate per event survive the selection, a random choice is performed in order to reduce the multiplicity to one. Any other choice could in principle affect the measurement, considering that the candidates are ordered by specific criteria.

The average multiplicities on the PartReco samples are shown in Table 2.11 before and after the selection. The effect of selection is clearly a reduction in the candidate multiplicity.

Sample	Pre-selection cand./event	Post-selection cand./event
Up 2011	1.674 ± 0.001	1.20 ± 0.01
Down 2011	1.677 ± 0.001	1.20 ± 0.01
Up 2012	1.6875 ± 0.0007	1.17 ± 0.01
Down 2012	1.6915 ± 0.0007	1.168 ± 0.009

Table 2.11: Number of candidates per event in PartReco samples.

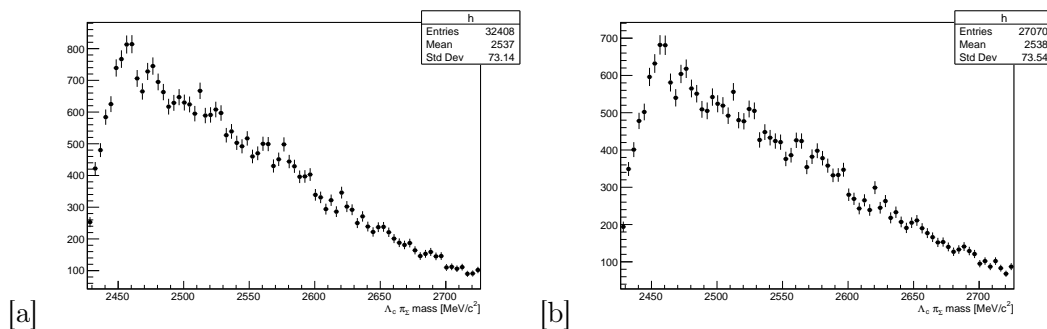


Figure 2.7: Comparison between $\Lambda_c \pi_\Sigma$ invariant mass spectrum obtained through the method presented before [a] and after reducing multiplicity to 1 [b] for 2011 sample.

In Figures 2.7 and 2.8 the $\Lambda_c \pi_\Sigma$ invariant mass spectrum obtained through the method for selected candidates is shown before and after the choice of a single candidate per event for the 2011 and 2012 MagDown subsamples. As it can be seen, this choice does not modify substantially the spectra.

2.2.3.6 FullReco line

All the selections applied discussed so far in this section are automatically applied to the candidates defined, at stripping level, as FullReco line, since they are a subsample of the PartReco.

Further selections are needed, however, to better define this sample.

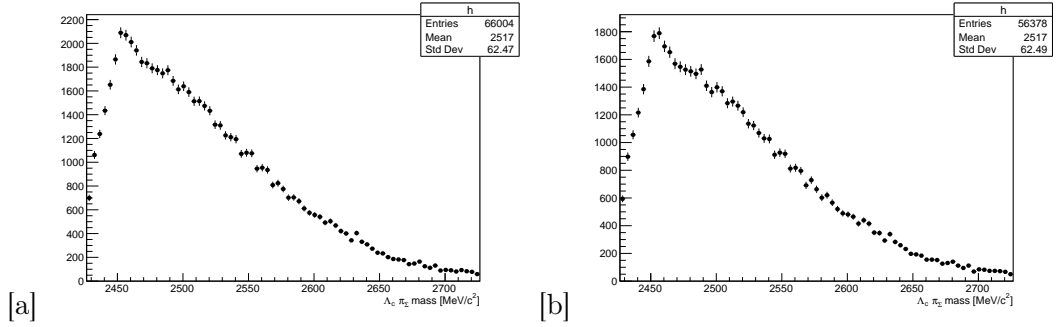


Figure 2.8: Comparison between $\Lambda_c \pi \Sigma$ invariant mass spectrum obtained through the method presented before [a] and after reducing multiplicity to 1 [b] for 2012 sample.

In fact, as reported in Table 2.6, the presence of a Λ_c decaying in $pK\pi$ is only weakly required at stripping level, and suppression of background contributions from fake Λ_c 's is needed.

Once established a one-to-one correspondence between the selected PartReco sample and the corresponding FullReco candidates, only those with a $pK\pi$ invariant mass m_Λ within $\pm 20 \text{ MeV}/c^2$ from the nominal Λ_c mass ($2286 \text{ MeV}/c^2$) are considered. Moreover, it is required m_B the invariant mass of the seven particles in the final state (namely $p \pi \pi \pi \pi p_\Lambda K_\Lambda \pi_\Lambda$) to be in a window of $60 \text{ MeV}/c^2$ centred at the B_u nominal mass ($5279 \text{ MeV}/c^2$).

At this stage loose cuts on the particle identification variables PIDp and PIDK are applied to the proton and the pion coming from the Λ_c , and the detail is reported in Table 2.10.

As in PartReco case, a random choice was applied to select only one candidate per event in case of multiplicity greater than one to the FullReco sample as well. However, the numbers of events affected is very small.

2.3 Signal extraction

2.3.1 Strategy

In order to extract the number of signal events ($B_u^+ \rightarrow p\pi^+\pi^+\bar{\Sigma}_c^{--}$), which is equal to the number of initial Λ_c , an unbinned maximum-likelihood fit was performed on the mass spectrum obtained through the method explained in Section 2.1. The mass of Σ_c is in fact computed by adding the four-momentum of the slow pion to that of the Λ_c , this latter being inferred by assuming the final state particles to be produced through the decay chain $B_u^+ \rightarrow p\pi^+\pi^+\bar{\Sigma}_c^{--}$ and the presence of a Λ_c only in the final state. A resonance in the mass region around $2455 \text{ MeV}/c^2$ should then be observed and allow to measure the number of initial Λ_c 's.

Once this sample is defined, a further selection is applied on those events containing

a Λ_c reconstructed through $pK\pi$ and an unbinned maximum likelihood is performed on the relative Σ_c mass spectrum.

This choice was driven by the intent to minimise systematic errors, by applying to both PartReco and Full samples the same fit procedure described in details in Section 2.3.2.

2.3.2 Fit

The signal and the background parameters are obtained performing an unbinned maximum-likelihood fit to the Σ invariant mass spectrum.

This technique has been applied through an algorithm implemented in ROOT [14]. A data sample consists of a certain number N of data points in the observable Σ_c calculated mass. The observable distributions is modelled with a probability density function (PDF), $P(m_\Sigma|\bar{\theta})$, where $\bar{\theta} = \theta_1, \theta_2, \dots$ is a set of unknown parameters.

The likelihood function, $L(\bar{\theta})$, is defined as the product of the PDFs of all reconstructed candidates; i.e. $L(\bar{\theta}) = \prod_{i=1}^N P(m_{\Sigma_i}|\bar{\theta})$.

This function constitutes an estimate of the probability to obtain the measured quantities given the parameters $\bar{\theta}$. Maximizing the likelihood function gives the best estimate for the unknown parameters. Generally the negative logarithm of the likelihood function is used rather than the function itself, so that during the fitting procedure the function

$$-\ln L(\bar{\theta}) = -\sum_{i=1}^N \ln P(m_{\Sigma_i}|\bar{\theta})$$

has to be minimised and, in this analysis, this aim is achieved through the Minuit framework [16].

The sum of the two components, namely signal and background, is described by the PDF

$$P(m_\Sigma|\bar{\theta}) = f_{sign} \cdot P_{Sign}(m_\Sigma|\bar{\theta}_{sign}) + (1 - f_{sign})P_{Bkg}(m_\Sigma|\bar{\theta}_{bkg})$$

where f_{sign} is the fraction of signal events and is defined as

$$f_{sign} = \frac{N_{sign}}{N_{sign} + N_{bkg}}$$

with N_{sign} and N_{bkg} the number of signal and background events, respectively.

Even if it is not trivial to define a goodness of a fit performed with such a technique, there are some important advantages in using the unbinned instead of the corresponding binned version. In fact, in this way the result is free from statistical fluctuations and the presence of bins with few events does not affect the procedure, leading to smaller errors than in the binned case.

Once the fit has been performed and a binning defined for the plot, the quality of the obtained PDF can be judged by the pull distribution. The pull p in each mass bin i is defined as

$$p_i = \frac{N_i - P(m)_i}{\sigma_i}$$

where N_i are the entries in bin i , σ_i is its statistical uncertainty and $P(m)_i$ is the value of the PDF at the centre of bin i .

Signal

The parameters of the PDF for the signal component were extracted by fitting the MonteCarlo sample, properly selected. The same selection tuned for the data sample and explained in Section 2.2.3 was applied to the MonteCarlo detector level, with further requirements on the true identity and correct origin of particles.

The PDF function used for the signal component $P_{sign(2455)}$ is a relativistic Breit-Wigner (Appendix C).

There is no specific reason or physical motivation for this specific choice, since the spectrum fitted is not obtained from a direct measurement of the Σ_c invariant mass, but rather from the calculation implied by the method explained in Section 2.1.

Due to the slight differences between the selection criteria applied, specifically the BDT (see Section 2.2.3.3), the MonteCarlo samples concerning 2011 and 2012 were fitted separately (Figure 2.9). The parameters obtained are reported in Table 2.12.

Parameter	2011	2012
$\alpha_o \pm \sigma_\alpha$	2453.6 ± 0.2	2453.5 ± 0.2
$\beta_o \pm \sigma_\beta$	13.2 ± 0.6	13.1 ± 0.4
$\gamma_o \pm \sigma_\gamma$	160 ± 20	180 ± 24

Table 2.12: Fit parameters for 2011 and 2012 MonteCarlo signal events.

The values of the parameters obtained from the fit to the MC data were used to fix the parametrisation of the signal PDF, leaving only the normalization free. To be specific, when fitting the data, each parameter was allowed to vary within a gaussian constraint, having as mean value that obtained when fitting the MC sample (α_o , β_o , γ_o respectively) and as standard deviation the uncertainty coming from the fit itself (σ_α , σ_β , σ_γ), i.e.

$$P'_{sign(2455)} = P_{sign(2455)} \cdot e^{-\frac{(\alpha-\alpha_o)^2}{\sigma_\alpha^2}} \cdot e^{-\frac{(\beta-\beta_o)^2}{\sigma_\beta^2}} \cdot e^{-\frac{(\gamma-\gamma_o)^2}{\sigma_\gamma^2}}$$

Background

Unfortunately, it is not possible to produce MonteCarlo samples for all the background contributions.

However, since this analysis deals with partially reconstructed events, a big effort was spent with the aim to understand and model the background. In fact, the method imposes a specific decay chain and assumes the presence of particles not detected. This, in non-signal candidates is a fake hypothesis, and it is a non trivial task to determine the

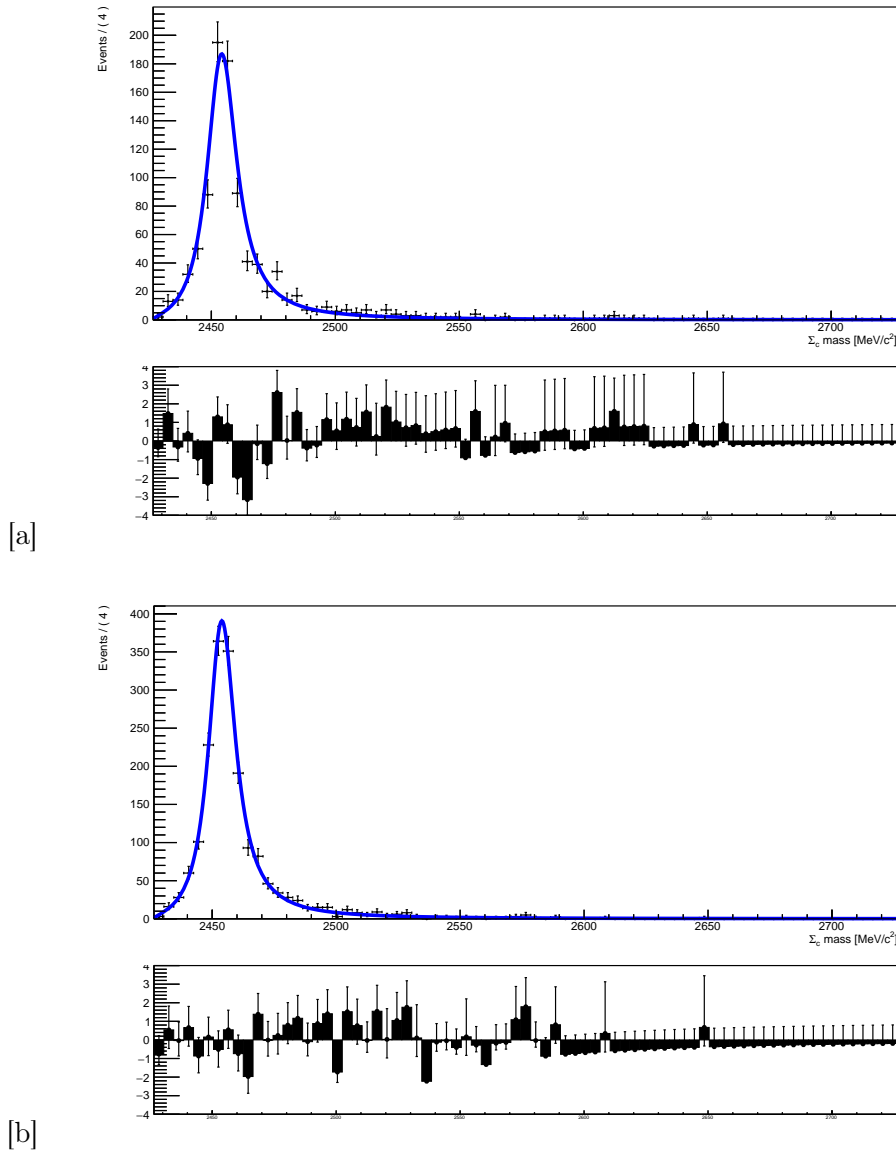


Figure 2.9: Fit result obtained on Σ_c calculated mass spectrum for the $B_u^+ \rightarrow p\pi^+\pi^+\bar{\Sigma}_c(2455)^--$ 2011 [a] and 2012 [b] Montecarlo samples.

character of background events, trace them to their source and thence distinguish and isolate one component from the others.

The selection applied to data, being tuned on signal, is meant to suppress self-generated background as well as the other components mentioned in Section 2.2.2.

In Table 2.13 the ratio between self-generated background candidates B and the sum

of them with signal ones S in MonteCarlo is reported per year and polarity. As it can be seen, the ratio $B/(S+B)$ decreases together with the tightening of the selection. Moreover, choosing one candidate per event drops the chance to select a false candidate, as shown in Table 2.14. Once all the requirements have been applied and one candidate per event chosen, the fraction of self-generated background events is about 6-7%. In our simulation sample the majority of events surviving the selection are generated by the combination of one or more correct tracks from B with the pion coming from the Λ_c instead. However, it is worth recalling that in the MonteCarlo used all the Λ_c s are forced to decay in $pK\pi$, therefore the expected fraction in real data is ~ 20 times smaller, leading to the conclusion that this contribution can be neglected.

Selection	MagUp 2011	MagDown 2011	MagUp 2012	MagDown 2012
None	0.536 ± 0.005	0.541 ± 0.005	0.549 ± 0.003	0.546 ± 0.003
Kinematical	0.319 ± 0.004	0.329 ± 0.004	0.338 ± 0.003	0.331 ± 0.003
+Trigger	0.18 ± 0.01	0.19 ± 0.01	0.19 ± 0.01	0.193 ± 0.009
+BDT	0.095 ± 0.010	0.040 ± 0.007	0.069 ± 0.006	0.079 ± 0.006
+PID	0.08 ± 0.01	0.08 ± 0.01	0.066 ± 0.007	0.075 ± 0.007

Table 2.13: $B/(S+B)$, all candidates

Sample	Signal	Self-generated Bkg	$B/(S+B)$
MagUp 2011	633	49	0.07 ± 0.01
MagDown 2011	606	39	0.06 ± 0.01
MagUp 2012	1298	76	0.055 ± 0.006
MagDown 2012	1375	93	0.063 ± 0.007

Table 2.14: Self-generated background after selection, 1 candidate per event

Partial reconstruction and random combination of tracks are expected to be the main sources of background. As mentioned in Section 2.2.3.1, two different stripping lines (WS and WS-SC) were written to allow those backgrounds to be studied and possibly to extract the shapes for these two components. But even these stripping lines, envisaged to give a model for combinatorial background, showed significant differences in the mass spectrum distribution with respect to the signal.

After accurate studies and a long time devoted to this investigation, significant irreducible differences remained, whose origin was difficult to trace. Therefore, the conclusion that only an empirical solution at this stage would be viable.

It was then decided to fit the data sample by assuming it to be the sum of two components, namely signal and combinatorial/partially reconstructed background, the latter being determined empirically by the subtraction of the signal component from the total.

Although the two background lines could not provide an exact description of background in PartReco, the specific choice of the PDF used was inspired by the $\Lambda_c\pi\Sigma$ distribution in this two lines.

The PDF function used for the background components is:

$$P_{bkg} = (x - x_{th})^\alpha \cdot \exp\left(-\frac{x - x_{th}}{\beta}\right)$$

An unexpected contribution

During a preliminary analysis of the FullReco sample, an excess of events was observed in the Σ_c mass spectrum at around $2520\text{MeV}/c^2$. After some studies aimed to identify the origin of this peak, it came out that no selection designed to suppress background events was able to reduce it, leading to the conclusion that it was the first observation of the decay $B_u^+ \rightarrow p\pi^+\pi^+\bar{\Sigma}_c(2520)^{-}$.

Parameters	2011	2012
a1	0.31 ± 0.13	0.40 ± 0.08
a2	0.23 ± 0.09	0.63 ± 0.13
n1	3.7 ± 0.7	121.92 ± 0.02
n2	4.1 ± 0.5	5.1 ± 1.0
m	2516.1 ± 0.4	2518.3 ± 0.8
s	3.6 ± 1.5	9.4 ± 1.8

Table 2.15: Parameters of the Double Crystal-Ball function for 2011 and 2012 MonteCarlo $\Sigma_c(2520)$ signal events.

A MonteCarlo sample was then produced, under the same conditions as the one described in Section 2.2.1, simulating this new decay mode.

Once the selection optimised for the $\Sigma_c(2455)$ to the candidates of this MonteCarlo was applied and the momentum of the Λ_c computed via the method already described, it was found that the spectrum of the calculated Σ_c mass was described by a double Crystal Ball PDF $P_{sign(2520)}$ [17], a function with a gaussian core, defined by the parameters m and s, and asymmetric tails defined by the a1, a2, n1 and n2 parameters.

As for the $\Sigma_c(2455)$ component, in the global fit to data, the PDF parameters were left free to vary within a gaussian constraint with mean value the value fitted in the MonteCarlo sample and standard deviation the uncertainty coming from the fit itself.

The results obtained for different polarities of 2011 and 2012 are slightly different and are reported in Table 3.10. The fit result for the 2011 and 2012 MC samples is shown in Figure 2.10.

2.3.2.1 PartReco line

The total function used in the PartReco sample fitting procedure is therefore defined as:

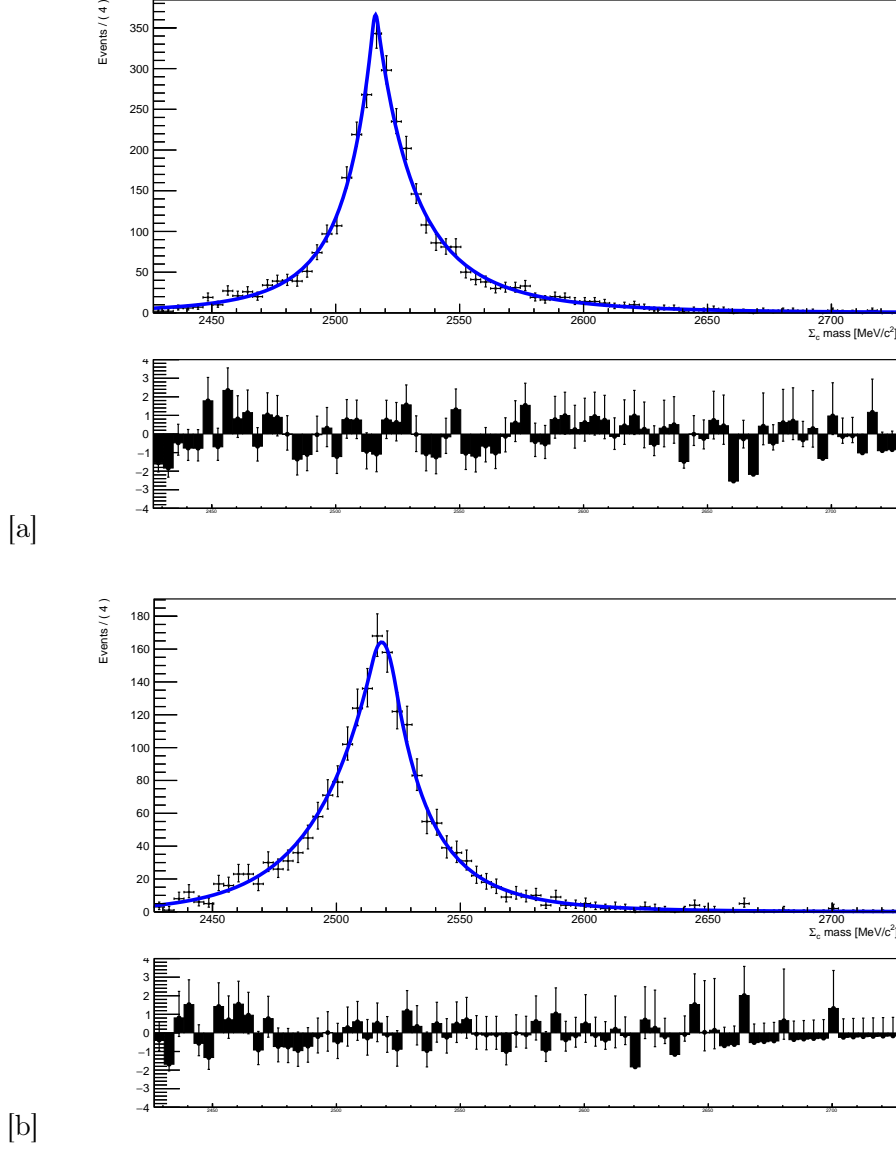


Figure 2.10: Fit result obtained on Σ_c calculated mass spectrum for the $B_u^+ \rightarrow p\pi^+\pi^+\bar{\Sigma}_c(2520)^-$ 2011 [a] and 2012 [b] MonteCarlo samples.

$$P_{tot} = f_{sign(2455)} \cdot P'_{sign(2455)} + f_{sign(2520)} \cdot P'_{sign(2520)} + f_{bkg} \cdot P_{bkg}$$

where $P'_{sign(2455)}$ and $P'_{sign(2520)}$ are the two Σ_c 's signal components, multiplied by the functions expressing the gaussian constraints to the respective parameters.

An unbinned maximum likelihood fit was performed on the $\Lambda_c\pi\Sigma$ inferred mass spec-

trum of both polarities for each year.

Parameter	2011	2012
α	0.53 ± 0.2	0.47 ± 0.03
β	91 ± 2	41 ± 7
A	-	2.081 ± 0.002
B	-	39.2 ± 0.3

Table 2.16: Background fitted parameters.

Specifically, a simultaneous fit was performed for MagUp and MagDown samples of 2011 and 2012 separately, since subsamples of different polarities are supposed to be consistent. In fact the general collision and data-taking conditions and the energy in the center of mass are constant through the year.

This assumes that background parameters and the relative ratios between different contributions are the same, independently of the magnetic field configuration.

Contribution	2011		2012	
	MagUp	MagDown	MagUp	MagDown
Signal $\Sigma_c(2455)$	241 ± 98	352 ± 143	970 ± 263	1063 ± 288
Signal $\Sigma_c(2520)$	0 ± 20	0 ± 29	0 ± 42	0 ± 46
Background I	10272 ± 3270	14996 ± 4773	19098 ± 4557	20933 ± 4995
Background II	-	-	6419 ± 1777	7036 ± 1948

Table 2.17: Fit results on yields, obtained from simultaneous fitting.

However, given the variation of data taking conditions between 2011 and 2012, it is reasonable to expect differences in the background line shapes of the two data samples.

In fact, while for 2011 a simple P_{bkg} was sufficient to describe the background, for the 2012 samples it was necessary to use a combination of two PDFs of the same shape, with different parameters:

$$P_{bkg}^{2012} = P'_{bkg} + P''_{bkg}$$

where

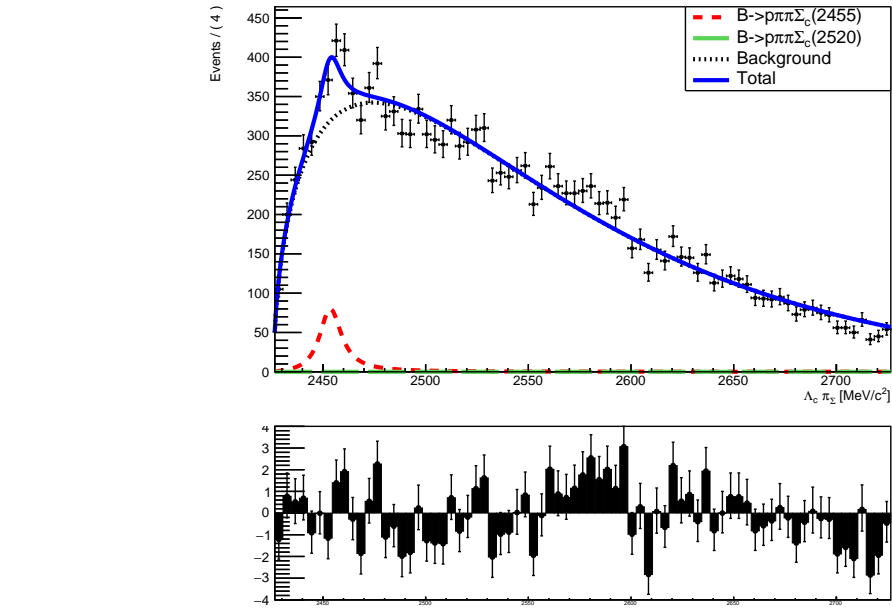
$$P'_{bkg} = (x - x_{th})^\alpha \cdot \exp\left(-\frac{x - x_{th}}{\beta}\right);$$

and

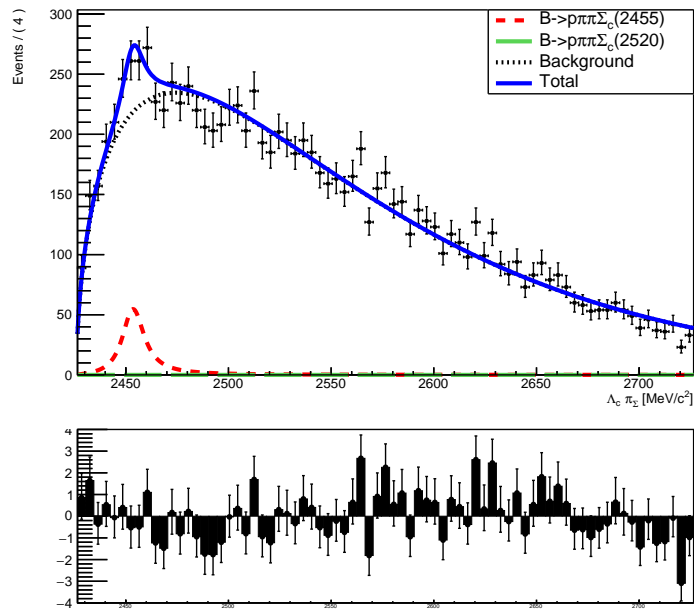
$$P_{bkg} = (x - x_{th})^A \cdot \exp\left(-\frac{x - x_{th}}{B}\right);$$

The fit parameters obtained for these contributions are reported in Table 2.16.

The fitting results are shown in Figure 2.11 for 2011 and in Figure 2.12 for 2012.

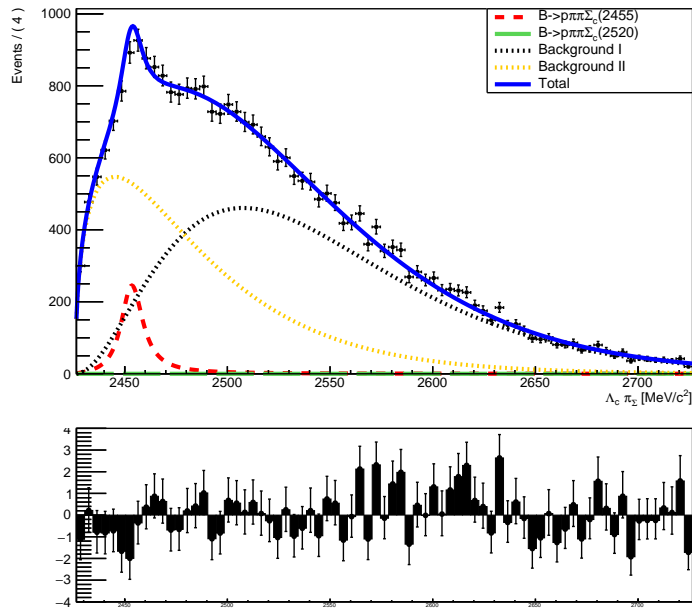


[a]

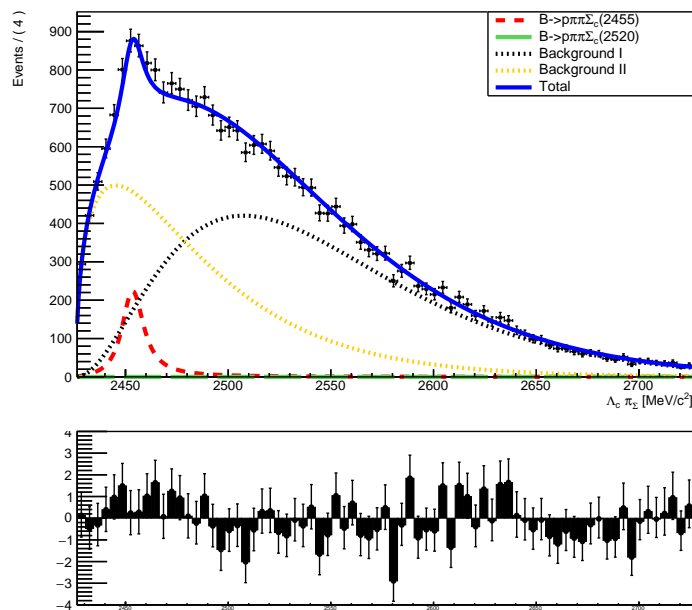


[b]

Figure 2.11: Fit result for PartReco line of MagUp [a] and MagDown [b] 2011 subsamples.



[a]



[b]

Figure 2.12: Fit result for PartReco line of MagUp [a] and MagDown [b] 2012 subsamples.

The yields for each contribution are reported in Table 2.17.

For each year, the ratio between the total number of events of the two polarities follows the integrated luminosity, as expected. Also the signal contributions are in the expected ratios in each year. However, a comparison between the two years shows that the number of signal events in 2012 exceeds by a factor of almost two what can be predicted on the basis of luminosity and the number of events in 2011.

Large errors characterise the background yields due to the almost total freedom on the PDF modelling the background. This feature reflects itself naturally on the uncertainty on the signal yield as well.

The contribution due to the $B_u \rightarrow p\pi\pi\Sigma_c(2520)$ decay is estimated to be compatible with zero.

Contribution	2011	2012
Signal $\Sigma_c(2455)$	593 ± 91	2035 ± 190
Signal $\Sigma_c(2520)$	0 ± 49	0 ± 78
Background I	25266 ± 182	13554 ± 1057
Background II	-	39929 ± 1038

Table 2.18: Fit results on yields obtained on PartReco lines for the total 2011 and 2012 data samples.

A raw estimate for the ratio of the selection efficiencies computed for the $B_u \rightarrow p\pi\pi\Sigma_c(2455)$ and $B_u \rightarrow p\pi\pi\Sigma_c(2520)$ decays gave a value of ~ 4 . In addition the relative branching fraction of the two decay modes is ~ 0.7 (see Chapter 4 of this thesis). Therefore, given the large broadness of its line shape, it is plausible to imagine that the signal might have been absorbed by the empirically extracted background contribution.

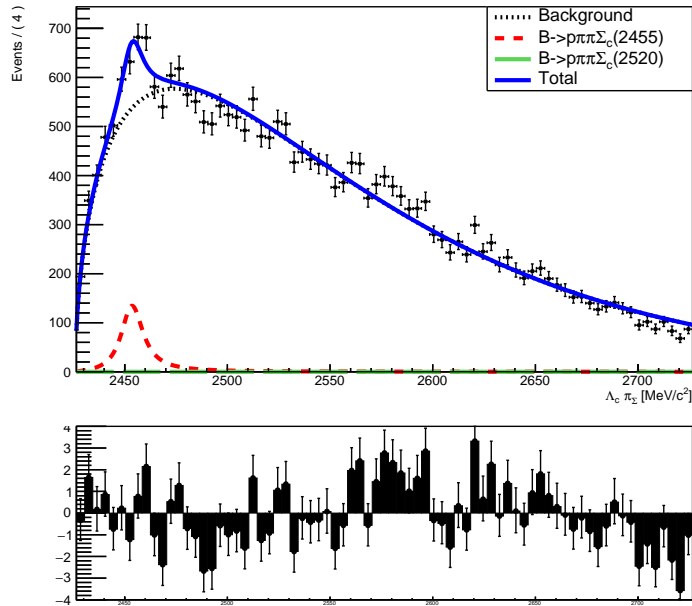
In the light of these considerations, in order to reduce statistical errors due to fitting procedure, a global fit for the MagUp and MagDown subsamples was performed separately for 2011 and 2012. The numerical results are summarised in Table 2.18, while the plots showing the fit results superimposed to the data are visible in Figure 2.13 for 2011 and 2012.

2.3.2.2 FullReco line

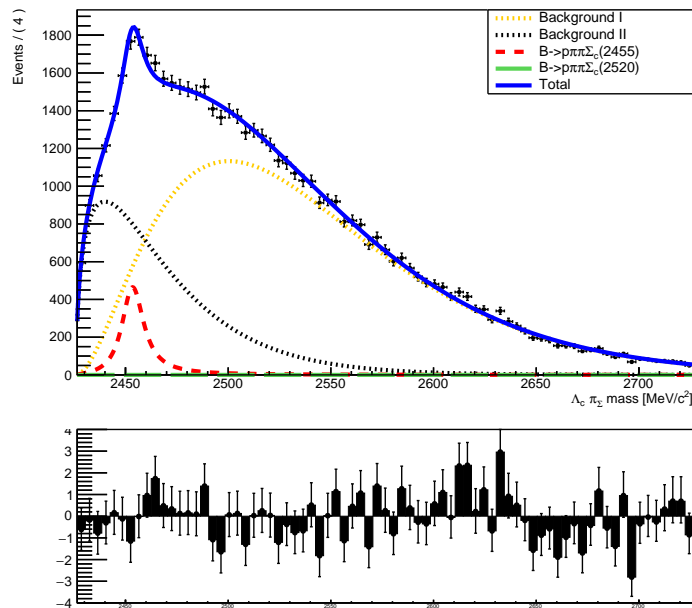
Having applied all the selections discussed in Section 2.2.3 to the complete FullReco sample (i.e. 2011+2012, regardless of magnet polarity), the inferred Σ_c mass spectrum shown in Figure 2.14 is obtained.

It is visible a small excess of events around $2520 \text{ MeV}/c^2$, confirming the first observation of the decay $B_u^+ \rightarrow p\pi^+\pi^+\bar{\Sigma}_c(2520)^{-}$.

It is worth noting that the spectrum falls definitely to zero for masses above $\sim 2740 \text{ MeV}/c^2$. This could give a quantitative idea of the effective reduction of the non-resonant contribution $B_u^+ \rightarrow p\pi^+\pi^+\bar{\Lambda}_c^-\pi^-$, which is expected to peak at $\sim 2700 \text{ MeV}/c^2$ and has a branching fraction about 8 times larger than the resonant component. The whole



[a]



[b]

Figure 2.13: Fit result for PartReco line of 2011 [a] and 2012 [b] samples.

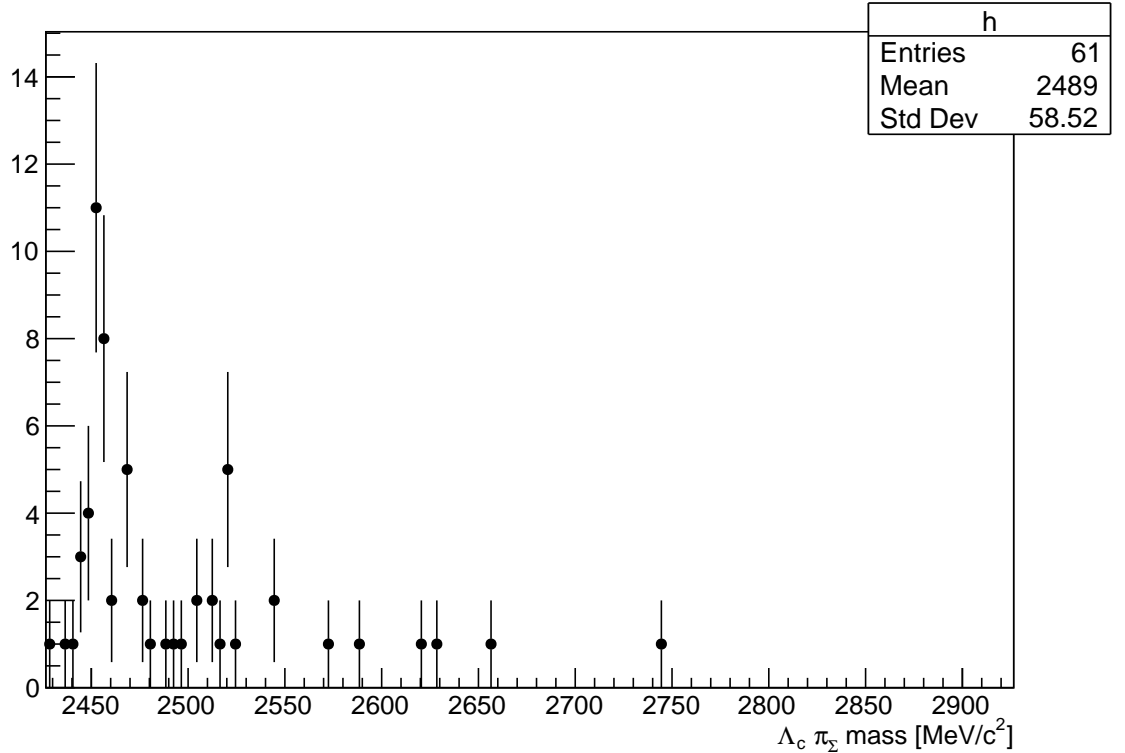


Figure 2.14: $\Lambda_c\pi_\Sigma$ invariant mass spectrum obtained when the proposed method is applied to the FullReco line for the 2011+2012 sample, regardless of magnet polarity.

selection in fact had been devised and tuned to suppress all contributions but the resonant signal and this appears to be the case. However, only a MonteCarlo produced in the same conditions as those one used for this analysis could provide a numerical estimate for this suppression factor. Unfortunately, production of MonteCarlo samples is limited, due to a combination of a large number of requests and the need to optimize the computing resources for the whole collaboration.

Since we have no hint of evidence of possible background contributions, the total function used in the FullReco sample fitting procedure is defined simply as:

$$P_{tot} = f_{sign(2455)} \cdot P'_{sign(2455)} + f_{sign(2520)} \cdot P'_{sign(2520)}$$

where $P'_{sign(2455)}$ and $P'_{sign(2520)}$ are the two Σ_c s signal components, multiplied by the respective parameters gaussian constraints.

An unbinned maximum likelihood fit was performed on the $\Lambda_c\pi_\Sigma$ inferred mass spectrum of both polarities for each year. The results are shown in Figure 2.15 for 2011 and in Figure 2.16 for 2012 and the yields corresponding to the two contributions are

Contribution	2011		2012	
	MagUp	MagDown	MagUp	MagDown
Signal $\Sigma_c(2455)$	2.4 ± 1.7	5.3 ± 2.5	18.1 ± 4.5	13.1 ± 3.8
Signal $\Sigma_c(2520)$	1.6 ± 1.4	2.7 ± 1.9	5.9 ± 2.9	6.9 ± 2.9

Table 2.19: Fit results on yields obtained on FullReco lines.

Contribution	2011	2012
Signal $\Sigma_c(2455)$	7.7 ± 3.0	31.1 ± 5.9
Signal $\Sigma_c(2520)$	4.3 ± 2.4	12.9 ± 4.1

Table 2.20: Fit results on yields obtained on FullReco lines for the total 2011 and 2012 samples.

available in Table 2.19.

Consistently with what was observed in PartReco samples, the ratio between the number of signal events in different polarities reflects the one between luminosities, while the number of signal events in 2011 over those fitted in 2012 sample is 2 times larger than what it was expected to be.

Similarly to what it has been done on PartReco sample, a global fit including both samples of different polarities for each year was performed. The numerical results are shown in Table 2.20 and the plots showing the results of the fit are available in Figure 2.17.

2.3.2.3 Raw branching ratio

The raw branching fraction values obtained from the fit procedure described in the previous sections are reported in Table 2.21.

2011		2012	
MagUp	MagDown	MagUp	MagDown
0.0100 ± 0.0081	0.0151 ± 0.0094	0.0187 ± 0.0069	0.0123 ± 0.0049
0.0132 ± 0.0056		0.0157 ± 0.0033	

Table 2.21: Raw branching fractions.

2.4 Efficiencies

In order to obtain the yield for Λ_c decaying into $pK\pi$, the raw event yields, obtained from the fit are corrected for the efficiencies extracted from MonteCarlo.

As explained in the preceding chapters, since the FullReco sample is a proper sub-sample of PartReco, once demonstrated that no selection affects PartReco candidates

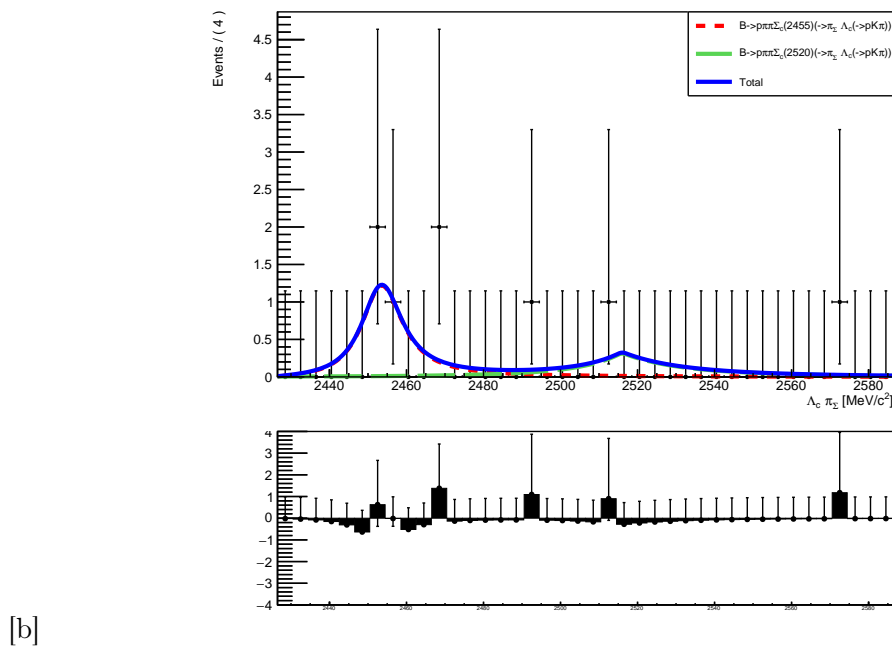
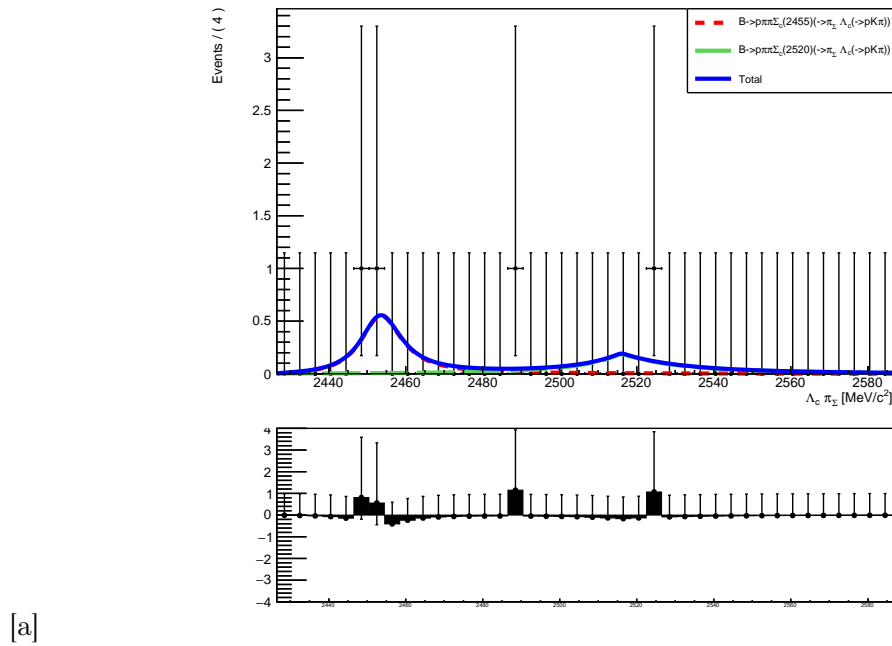
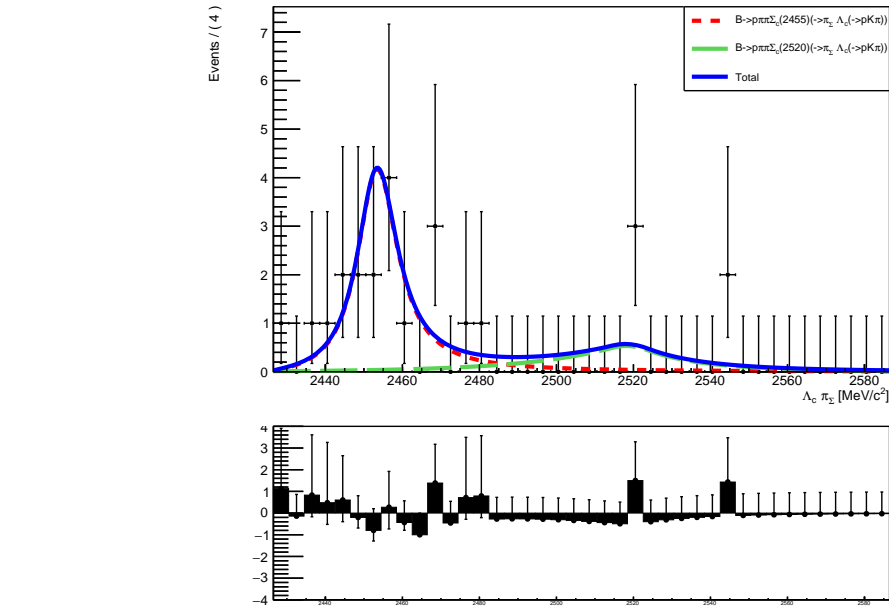
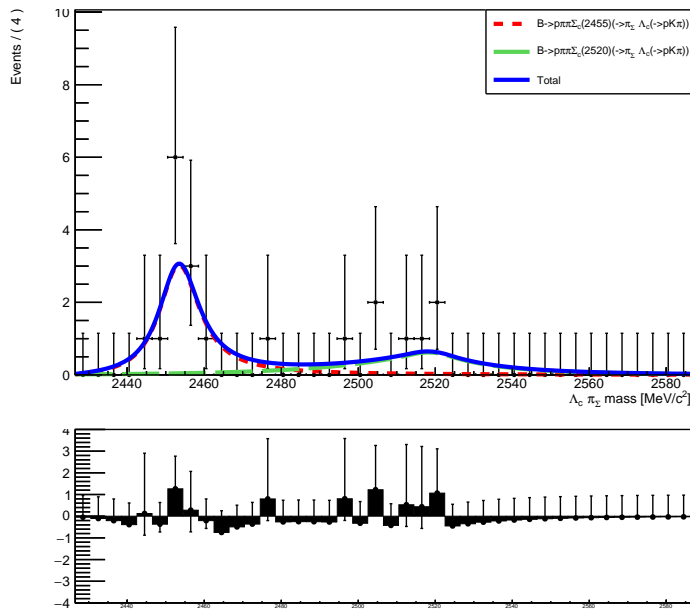


Figure 2.15: Fit result for FullReco line of MagUp [a] and MagDown [b] 2011 subsamples.

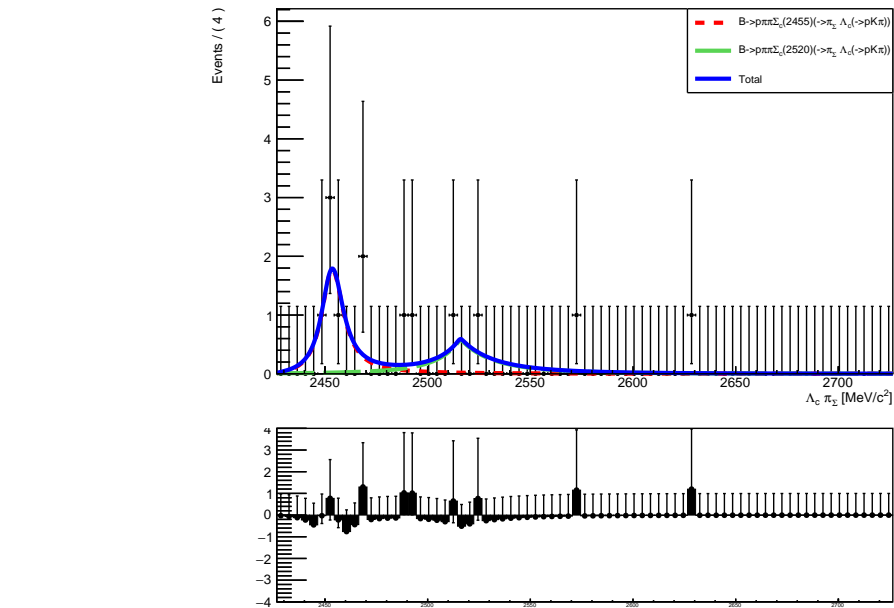


[a]

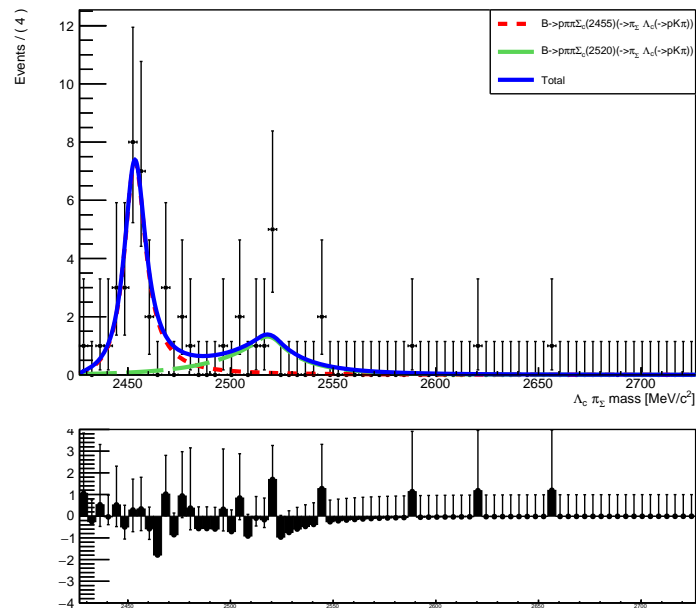


[b]

Figure 2.16: Fit result for FullReco line of MagUp [a] and MagDown [b] 2012 subsamples.



[a]



[b]

Figure 2.17: Fit result for FullReco line of 2011 [a] and 2012 [b] samples.

differently from FullReco ones, all the selection, acceptance and detection efficiencies can be factorized, except for:

- the reconstruction efficiency for Λ_c detected in $pK\pi$
- the PID efficiency concerning requirements on Λ_c 's daughters

The raw branching fraction, estimated by using the numbers obtained from the fit, has to be corrected as follows:

$$\mathcal{B}(\Lambda_c \rightarrow pK\pi) = \frac{N_{\Lambda_c \rightarrow pK\pi}^{FullReco}}{N_{\Lambda_c}^{PartReco}} \cdot \frac{1}{\epsilon_{reco\Lambda}} \cdot \frac{1}{\epsilon_{\Lambda}^{PID}} \quad (2.14)$$

The reason why the ϵ_{Λ}^{PID} needs to be computed separately is that the differences between simulation and data for PID variables entail a data-driven procedure in order to extract the efficiencies.

In fact, a weighting procedure of the PID calibration samples according to the signal tracks distributions in transverse momentum p_T and pseudorapidity η obtained from MC is performed in order to obtain the PID efficiencies.

2.4.1 Reconstruction efficiency of the Λ_c decay into $pK\pi$

The reconstruction efficiency for Λ_c can be computed as:

$$\epsilon_{reco\Lambda} = \frac{N_{\Lambda_c \rightarrow pK\pi}^{MC-Full}}{N_{\Lambda_c}^{MC-Part}} \quad (2.15)$$

where $N_{\Lambda_c \rightarrow pK\pi}^{MC-Full}$ is the number of Λ_c reconstructed from $pK\pi$ in the MonteCarlo FullReco sample after the selection (excluding PID on Λ_c 's daughters), while $N_{\Lambda_c}^{MC-Part}$ is the number of events $B \rightarrow p\pi^+\pi^+\bar{\Sigma}_c(2455)^{-}$, hence the number of Λ_c selected in MonteCarlo PartReco sample.

The efficiencies computed using the expression in Equation (2.15) at different levels of selection are reported in Table 2.22.

The selection does not affect differently events of the PartReco and the FullReco lines, and this is demonstrated by the fact that the apparent Λ_c branching fraction, computed at each step remains constant within the errors.

It is worth reminding that in our simulation all the Λ_c 's are forced to decay in a $pK\pi$ final state. This means that, if the acceptance, detection and reconstruction efficiencies were equal to 1, the apparent branching fraction measured in MC sample would be 100%.

Selection	MagUp 2011	MagDown 2011	MagUp 2012	MagDown 2012
Stripping	0.294±0.005	0.292±0.005	0.280±0.003	0.281±0.003
+Kinematical	0.294±0.005	0.292±0.005	0.279±0.003	0.281±0.003
+BDT	0.296±0.005	0.293±0.005	0.281±0.004	0.283±0.004
+Trigger	0.33±0.03	0.32±0.03	0.29±0.02	0.31±0.02
+Invariant mass (on FullReco)	0.30±0.03	0.28±0.03	0.28±0.02	0.31±0.02

Table 2.22: Efficiencies of reconstruction of Λ_c decay into $pK\pi$ at different steps of the selection and, separately for different years and magnet polarities.

2.4.2 PID efficiency

As explained in Section 2.2.3.4, distributions of PID related variables and relative efficiencies are not properly reproduced in MonteCarlo simulations. In fact, the detector occupancy in simulated events is lower than in real data and since the RICH performance depends on this occupancy, PID response appears different between simulation and data. For this, a data-driven approach is required.

In LHCb, a software package called PIDCalib [18] has been developed in order to make this procedure easily available for the entire collaboration, providing calibration samples and tools to analyse them.

Calibration samples are collections of tracks of a known, specific particle type, stored together with the relative kinematical variables.

Indeed, it is assumed that the PID variables of a particular track depend on kinematic or global event variables, e.g. track momentum, transverse momentum, pseudorapidity or number of tracks in the event. Then the most significant variables for a specific analysis can be chosen, and the calibration and signal samples (i.e. a MonteCarlo sample properly selected) are binned in these variables.

The population of each bin in the calibration and signal samples is compared and the weight of each bin is computed as the ratio of these two populations.

The true PID variables distribution of the signal tracks is given by the distribution obtained from the calibration sample, weighted bin-by-bin.

PID on proton from B_u

As already mentioned, PID efficiencies are computed in bins of variables such as transverse momentum and pseudorapidity.

A simple way to estimate if differences are expected between PartReco and FullReco samples is to make a comparison between the distributions of P_T and η for the two samples.

As shown in Figure 2.18 and Figure 2.19, no significant differences can be noticed between the distributions for 2011 and 2012, so that there is no reason to assume that

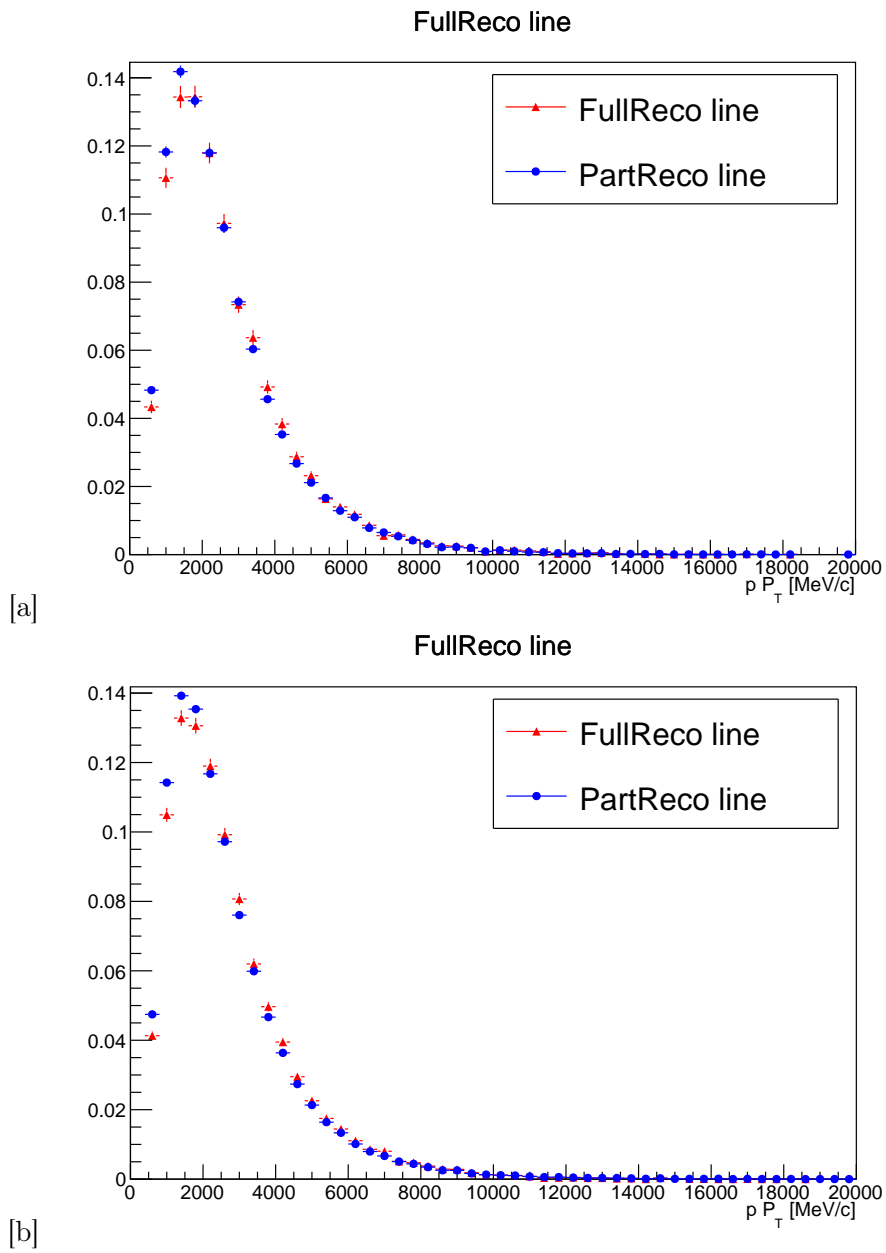


Figure 2.18: Proton P_T distribution for PartReco and FulReco samples in 2011 [a] and 2012 [b].

the PID efficiencies would be different for the two samples and therefore to prevent their factorisation.

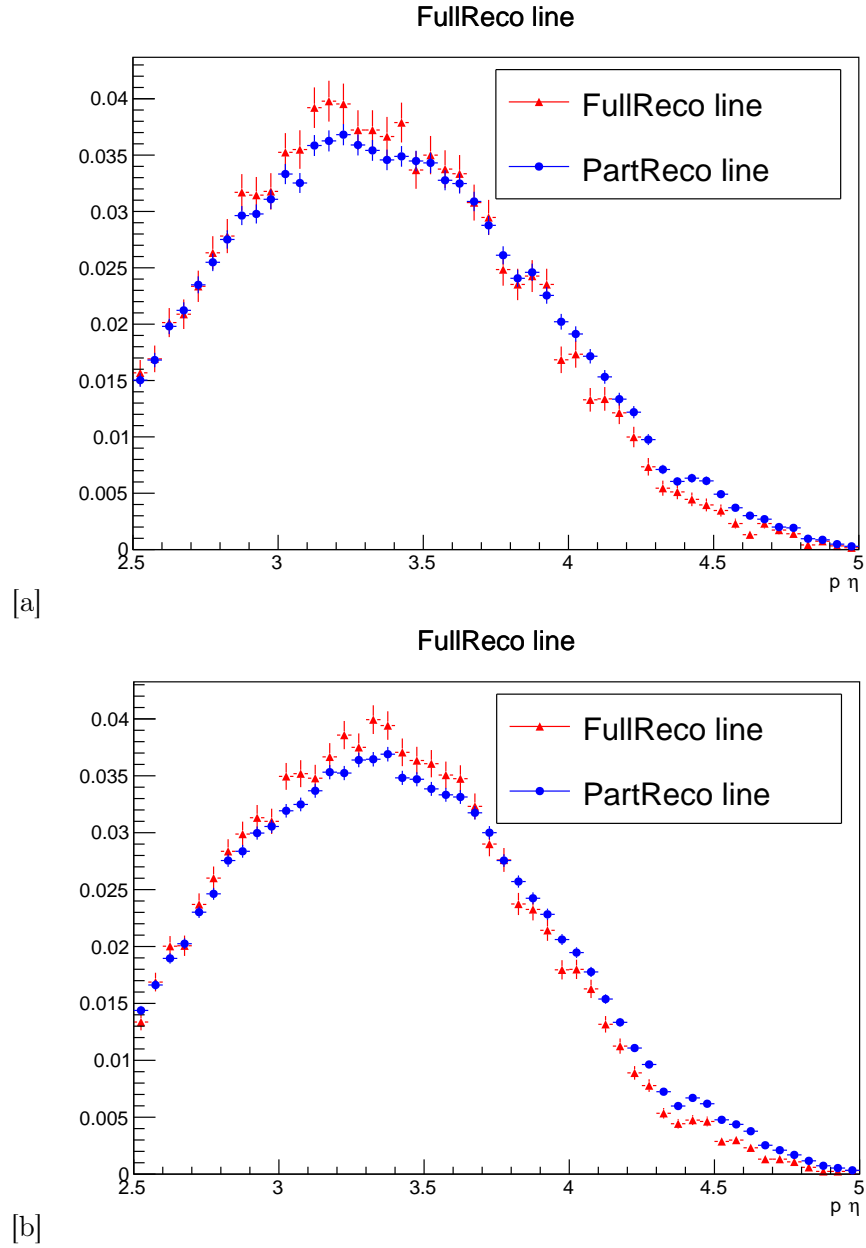


Figure 2.19: Proton η distribution for PartReco and FulReco samples in 2011 [a] and 2012 [b].

PID on Λ_c decay products

The PID on Λ_c 's daughters is the only selection applied solely on the FullReco sample. The efficiencies have been computed in bins of η and P_T either for the proton and the

kaon coming from Λ_c decay.

The signal samples used to perform the weighting have been obtained by selecting true signal MonteCarlo events with same requirements imposed on data, except for L0 and Hlt1 in order to obtain larger statistics.

In order to free the results from the specific choice of binning, three different schemes, called A, B and C, have been submitted to PIDCalib package.

The PID efficiencies ϵ_{PID} obtained by applying this procedure to the analysis presented in this thesis are reported in Tables 2.23 and 2.24. For each subsample, the central value has been obtained by computing the mean of the results corresponding to the three different binnings and the uncertainty is the main statistical uncertainty among those of the three results obtained.

Binning Scheme	MagUp 2011 (%)	MagDown 2011 (%)
A	$71.30 \pm 0.02(\text{stat})$	$71.12 \pm 0.01(\text{stat})$
B	$60.0 \pm 1.0(\text{stat})$	$60.3 \pm 0.8(\text{stat})$
C	$69.59 \pm 0.02(\text{stat})$	$69.28 \pm 0.02(\text{stat})$
Total	$67 \pm 0.1(\text{stat})$	$66.9 \pm 0.8(\text{stat})$

Table 2.23: PID efficiencies for three different binning schemes for 2011 subsamples.

Binning Scheme	MagUp2012 (%)	MagDown 2012 (%)
A	$68.6 \pm 0.01(\text{stat})$	$69.394 \pm 0.009(\text{stat})$
B	$57.7 \pm 0.1(\text{stat})$	$58.3 \pm 0.4(\text{stat})$
C	$67.68 \pm 0.01(\text{stat})$	$67.95 \pm 0.01(\text{stat})$
Total	$64.7 \pm 0.1(\text{stat})$	$65.2 \pm 0.4(\text{stat})$

Table 2.24: PID efficiencies for three different binning schemes for 2012 subsamples.

2.5 Systematic uncertainties

One of the main advantages of the method proposed and used in this thesis is the possibility to factorize all the efficiencies but those related to the requirements on the decay products of the Λ_c . This has the beneficial effect of a drastic reduction of the possible sources of systematic uncertainties, since the only one remaining is PID-related and will be considered in what follows.

The systematic error has been estimated by exploiting the three binning schemes used to compute the PID efficiency, by simply taking the maximum excursion between the mean value and the values obtained through PIDCalib.

The results obtained for the three schemes and the systematic associated to each subsample are reported in Tables 2.25 and 2.26.

For all subsamples, the estimated relative systematic uncertainty varies between 9% and 11%.

However, with a larger MonteCarlo and careful specific choices on the binnings used, it could be possible to further reduce these errors.

Binning Scheme	MagUp 2011 (%)	MagDown 2011 (%)
A	$71.30 \pm 0.02(\text{stat})$	$71.12 \pm 0.01(\text{stat})$
B	$60.0 \pm 1.0(\text{stat})$	$60.3 \pm 0.8(\text{stat})$
C	69.59 ± 0.02	$69.28 \pm 0.02(\text{stat})$
Total	$67 \pm 0.1(\text{stat}) \pm 7(\text{syst})$	$66.9 \pm 0.8(\text{stat}) \pm 6(\text{syst})$

Table 2.25: PID efficiencies for three different binning schemes for 2011 subsamples.

Binning Scheme	MagUp2012 (%)	MagDown 2012 (%)
A	$68.6 \pm 0.01(\text{stat})$	$69.394 \pm 0.009(\text{stat})$
B	$57.7 \pm 0.1(\text{stat})$	$58.3 \pm 0.4(\text{stat})$
C	$67.68 \pm 0.01(\text{stat})$	$67.95 \pm 0.01(\text{stat})$
Total	$64.7 \pm 0.1(\text{stat}) \pm 7(\text{syst})$	$65.2 \pm 0.4(\text{stat}) \pm 7(\text{syst})$

Table 2.26: PID efficiencies for three different binning schemes for 2012 subsamples.

2.6 Results

As discussed in Section 2.4, the raw numbers given in Section 2.3.2.3 have to be corrected by the PID and reconstruction efficiencies, in order to obtain the final measurement.

The resulting final values obtained for the branching fraction, after correction for Λ_c reconstruction efficiency only and after the further correction for PID on Λ_c decay products, are shown in the second and third rows of Tables 2.27 and 2.28.

The errors reported in Tables 2.27 and 2.28 are the result of quadratic propagation of the statistical errors due to the fitting and reconstruction efficiency. The statistical

	MagUp 2011	MagDown 2011	MagUp 2012	MagDown 2012
\mathcal{B}_{raw}	0.0100 ± 0.0081	0.0151 ± 0.0094	0.0187 ± 0.0069	0.0123 ± 0.0049
$\mathcal{B}_{raw}/\epsilon_{reco\Lambda}$	0.033 ± 0.027	0.054 ± 0.034	0.067 ± 0.025	0.040 ± 0.016
$\mathcal{B}_{raw}/(\epsilon_{reco\Lambda} \cdot \epsilon_{PID})$	0.0493 ± 0.040	0.081 ± 0.051	0.104 ± 0.038	0.061 ± 0.025

Table 2.27: Results on $\Lambda_c \rightarrow pK\pi$ branching fraction. The errors reported are purely statistical.

	2011	2012
\mathcal{B}_{raw}	0.0132 ± 0.0056	0.0157 ± 0.0033
$\mathcal{B}_{raw}/\epsilon_{reco\Lambda}$	0.046 ± 0.020	0.053 ± 0.011
$\mathcal{B}_{raw}/(\epsilon_{reco\Lambda} \cdot \epsilon_{PID})$	0.068 ± 0.030	0.082 ± 0.017

Table 2.28: Results on $\Lambda_c \rightarrow pK\pi$ branching fraction. The errors reported are purely statistical.

Sample	$\mathcal{B}(\Lambda_c \rightarrow pK\pi)$
MagUp 2011	$0.0493 \pm 0.040(stat) \pm 0.005(syst)$
MagDown 2011	$0.081 \pm 0.051(stat) \pm 0.008(syst)$
MagUp 2012	$0.104 \pm 0.038(stat) \pm 0.010(syst)$
MagDown 2012	$0.061 \pm 0.025(stat) \pm 0.006(syst)$
2011	$0.068 \pm 0.030(stat) \pm 0.007(syst)$
2012	$0.082 \pm 0.017(stat) \pm 0.008(syst)$

Table 2.29: Final results on branching fractions.

uncertainty associated to PID efficiency is negligible when compared with other uncertainties, either statistical, coming from the size of data sample and the fitting procedure, or systematic.

The final results, including both statistical and systematic uncertainties, are reported in Table 2.29.

For 2011, the systematic uncertainty is one order of magnitude smaller than the statistical, while for 2012 sample they are of the same order.

Since the results for the two years are in agreement, the weighted average can be computed yielding the result:

$$\mathcal{B}(\Lambda_c^+ \rightarrow pK^- \pi^+) = 0.079 \pm 0.015(stat) \pm 0.008(syst)$$

. The systematic uncertainty has been estimated under the assumption of a complete correlation for 2011 and 2012.

The final result is therefore:

$$\mathcal{B}(\Lambda_c^+ \rightarrow pK^- \pi^+) = 0.079 \pm 0.017$$

2.6.1 Dependence on background lineshape

The major source of uncertainty is linked to the background extraction procedure. Therefore, a study has been performed to evaluate the sensitivity of the result on the fitting procedure, varying in particular the range over which the fit was performed.

The results presented in the previous section were obtained following the procedure described in details in Section 2.3 and extending the fit to the range [2427:2727] MeV/c².

It was decided to limit this range to [24267:2587] MeV/c², to estimate the background line shape excluding its behaviour at high masses, and therefore determine a new number of decaying Λ_c 's.

It is clear that the reduced range does not affect at all the results obtained for the FullReco sample and discussed in Section 2.3.2.2. Therefore, those will be used in the determination of the branching fraction in this section.

The fit results obtained by fitting simultaneously the subsamples corresponding to different orientations of the magnet field are shown in Table 2.30.

	2011		2012	
Contribution	MagUp	MagDown	MagUp	MagDown
Signal $\Sigma_c(2455)$	295 ± 57	456 ± 69	883 ± 109	548 ± 111
Signal $\Sigma_c(2520)$	0 ± 48	0 ± 67	505 ± 182	533 ± 194
Background	7462 ± 145	10985 ± 124	21201 ± 283	23633 ± 298

Table 2.30: Fit results on yields obtained from simultaneous fitting of the samples corresponding to different magnet polarities, for each year, in the limited mass range.

1	2011		2012	
Contribution	MagUp	MagDown	MagUp	MagDown
Signal $\Sigma_c(2455)$	294 ± 63	465 ± 74	800 ± 117	624 ± 119
Signal $\Sigma_c(2520)$	30 ± 97	1 ± 52	582 ± 192	456 ± 203
Background	7462 ± 156	10975 ± 126	21207 ± 292	23629 ± 307

Table 2.31: Fit results on yields obtained from separate fitting, in the limited mass range.

	2011		2012	
Parameter	MagUp	MagDown	MagUp	MagDown
α	0.42 ± 0.4	0.46 ± 0.03	0.54 ± 0.02	0.55 ± 0.02
β	116 ± 9	109 ± 7	71 ± 2	73 ± 2

Table 2.32: Background fitted parameters in the limited mass range.

Contribution	2011	2012
Signal $\Sigma_c(2455)$	752 ± 95	1423 ± 167
Signal $\Sigma_c(2520)$	1 ± 114	1037 ± 279
Background	18475 ± 164	44837 ± 424

Table 2.33: Fit results on yields obtained on PartReco lines in the limited mass range.

	MagUp 2011	MagDown 2011	MagUp 2012	MagDown 2012
\mathcal{B}_{raw}	0.0082 ± 0.0061	0.0114 ± 0.0057	0.0226 ± 0.0065	0.0210 ± 0.0073
$\mathcal{B}_{raw}/\epsilon_{reco\Lambda}$	0.0273 ± 0.0205	0.0407 ± 0.0208	0.0807 ± 0.0239	0.0677 ± 0.0240
$\mathcal{B}_{raw}/(\epsilon_{reco\Lambda} \cdot \epsilon_{PID})$	0.041 ± 0.031	0.061 ± 0.031	0.125 ± 0.037	0.104 ± 0.037

Table 2.34: Results on $\Lambda_c \rightarrow pK\pi$ branching fraction from fitting a reduced mass range. The errors reported are purely statistical.

	2011	2012
\mathcal{B}_{raw}	0.0102 ± 0.0042	0.0219 ± 0.0049
$\mathcal{B}_{raw}/\epsilon_{reco\Lambda}$	0.035 ± 0.015	0.074 ± 0.017
$\mathcal{B}_{raw}/(\epsilon_{reco\Lambda} \cdot \epsilon_{PID})$	0.052 ± 0.022	0.114 ± 0.026

Table 2.35: Results on $\Lambda_c \rightarrow pK\pi$ branching fraction from fitting a reduced mass range. The errors reported are purely statistical.

Similar results were obtained by fitting the sub samples separately, leading to yields in agreement with the output of separate fitting and reported in Table 2.31.

The corresponding fit parameters obtained for the background contribution are reported in Table 2.32.

It can be seen clearly that parameters are in agreement for different polarities of the same year, while there exist differences between the 2011 and 2012 samples.

However, as mentioned, this discrepancy was already observed and can be attributed either to the different selection applied or to the different data-taking conditions between 2011 and 2012.

As in the results discussed in Section 2.3, for each year, the ratio between the total number of events of the two polarities follows the integrated luminosity, as expected. Some fluctuations are noticeable instead for the single contributions.

In particular, while the yields corresponding to signal contribution are in the same ratio (within the errors) as luminosities for 2011 and MagUp 2012, the MagDown 2012 sample differs significantly from expectations.

The signal-to-background ratio is also constant within the errors for all subsamples but MagDown 2012.

Figure 2.20 and Figure 2.21 show the results of the fit for 2011 and 2012, respectively.

As in the previous case, a global fit for the MagUp and MagDown subsamples was performed for each year, and the results shown in Table 2.33 for the PartReco samples (see Figure 2.22) were obtained.

The resulting final values obtained for the branching fraction are shown in the second and third rows of Tables 2.34 and 2.35.

The final results with both statistical and systematic uncertainties are reported in Table 2.36.

Sample	$\mathcal{B}(\Lambda_c \rightarrow pK\pi)$
MagUp 2011	$0.041 \pm 0.031(\text{stat}) \pm 0.004(\text{syst})$
MagDown 2011	$0.061 \pm 0.031(\text{stat}) \pm 0.005(\text{syst})$
MagUp 2012	$0.125 \pm 0.037(\text{stat}) \pm 0.01(\text{syst})$
MagDown 2012	$0.104 \pm 0.037(\text{stat}) \pm 0.01(\text{syst})$
2011	$0.052 \pm 0.022(\text{stat}) \pm 0.005(\text{syst})$
2012	$0.114 \pm 0.026(\text{stat}) \pm 0.012(\text{syst})$

Table 2.36: Final results on 2011 and 2012 from fitting a reduced mass range.

The systematic uncertainty is still one order of magnitude smaller than statistical in 2011, while in 2012 sample they are comparable.

The results obtained for different magnet polarities are in agreement with each other, separately for 2011 and 2012 data. However, a discrepancy exists when comparing the branching fraction measured using 2011 data with that measured in 2012. This discrepancy is at level slightly over two standard deviations. If nevertheless the two results are combined, the weighted average with relative uncertainty is:

$$\mathcal{B}(\Lambda_c^+ \rightarrow pK^- \pi^+) = 0.078 \pm 0.017(\text{stat}) \pm 0.012(\text{syst})$$

The total result is therefore:

$$\mathcal{B}(\Lambda_c^+ \rightarrow pK^- \pi^+) = 0.078 \pm 0.021$$

which is in agreement with the first one presented.

2.7 Conclusions

A measurement of the absolute branching fraction of the $\Lambda_c \rightarrow pK\pi$ decay was performed at LHCb using a dataset corresponding to 3 fb^{-1} of integrated luminosity, implementing a novel method [2] which exploits the decay $B_u \rightarrow p\pi\pi\Sigma_c(2455)$ and allows, for the first time, a measurement of this branching fraction in a hadron-collider environment.

The feasibility of the measurement through the method has been demonstrated successfully.

One of its major advantages is the factorisation of the efficiencies and the reduction of possible sources of systematic uncertainty, whose only source are essentially the criteria for particle identification imposed on the Λ_c decay products.

Larger simulation samples and careful choices are required however to make these errors smaller than statistical errors.

Some dependence of the result on the background estimation was observed between the results obtained for the 2011 and 2012 samples and a 2σ discrepancy was observed in the results obtained when the fit is performed over a reduced range of the mass spectrum.

However, the weighted average of the results presented in this work, lead to a common result, regardless of the procedure followed for the background estimation.

Further studies on this aspect may be carried on, in order to estimate more precisely and possibly suppress this dependence.

The model independent result presented has to be compared with the current value presented by [1], which is the average between two measurements performed at the Belle [9] and BES III [12] in 2014 and 2016, respectively. The two values, which were obtained in an e-e environment, have precisions of the order of 5-6%, although they are not consistent within errors. Our measurement is in agreement with both of them, even if the central value obtained is slightly larger than the current cited by the PDG. The total error is of $\sim 25\%$ and a larger statistic is required to better this precision.

For this reason, the analysis of data recorded at LHCb during 2015 and 2016 seems to be essential.

Data samples corresponding to $\sim 1.5 \text{ fb}^{-1}$ produced in pp collisions at 13 TeV in the center of mass are indeed already available. Since the cross-section for production of B_u mesons at this energy will be enhanced by a factor 2, an important improvement of the statistics is expected, which may shed light on the aspects still not completely understood observed in this work.

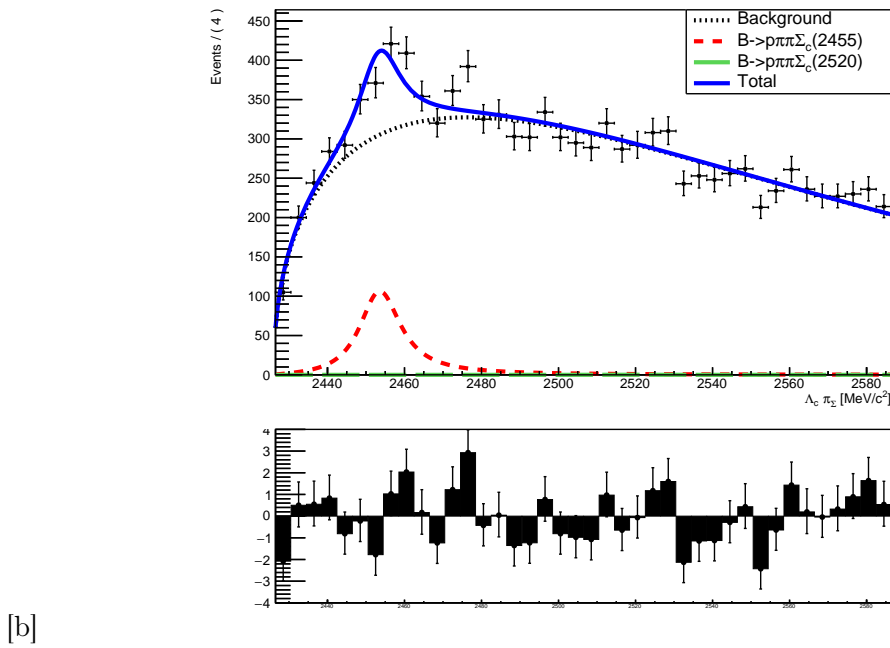
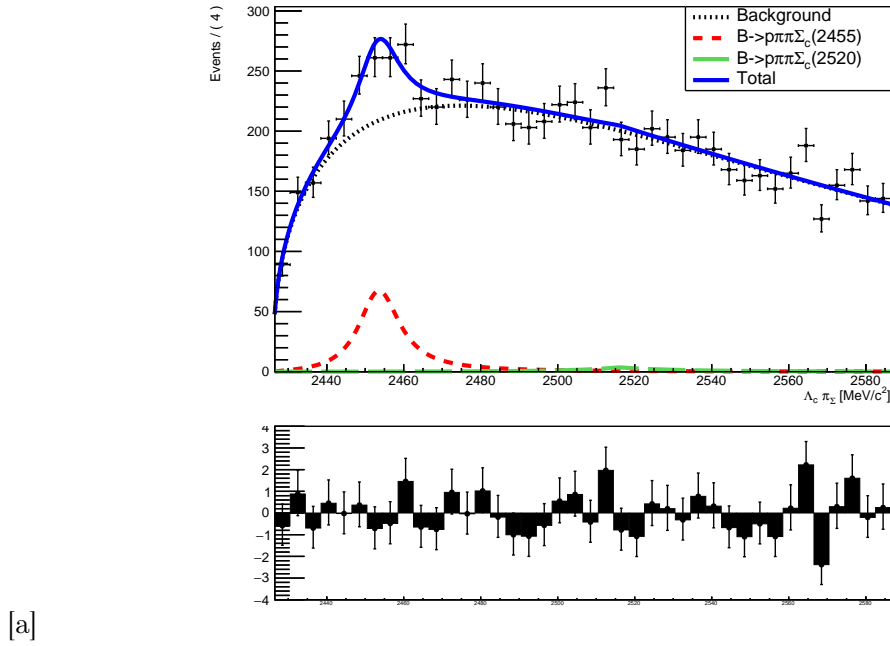
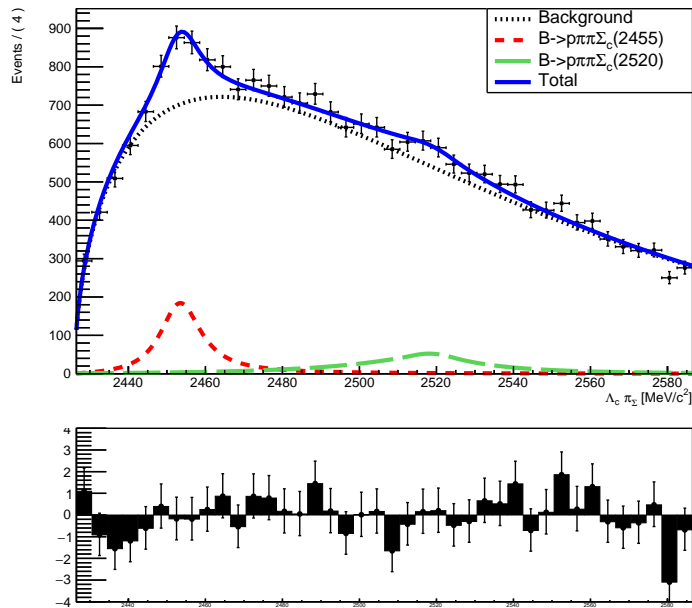
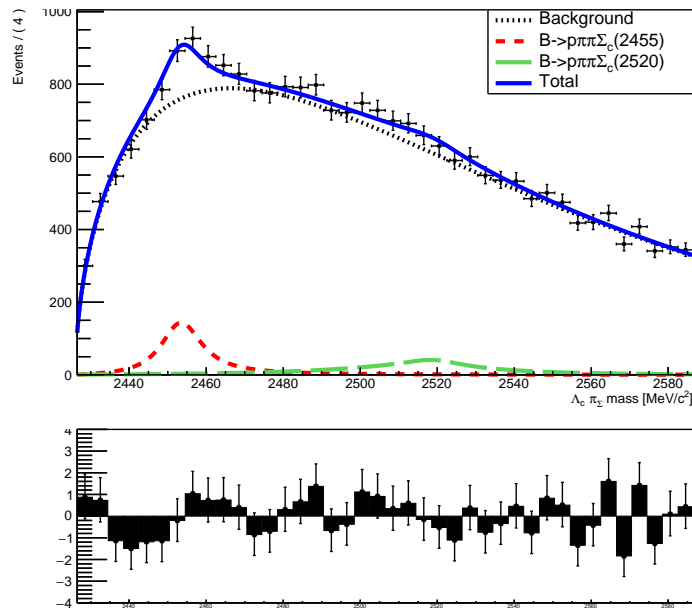


Figure 2.20: Fit result for PartReco line of MagUp [a] and MagDown [b] 2011 subsamples in the reduced mass range.

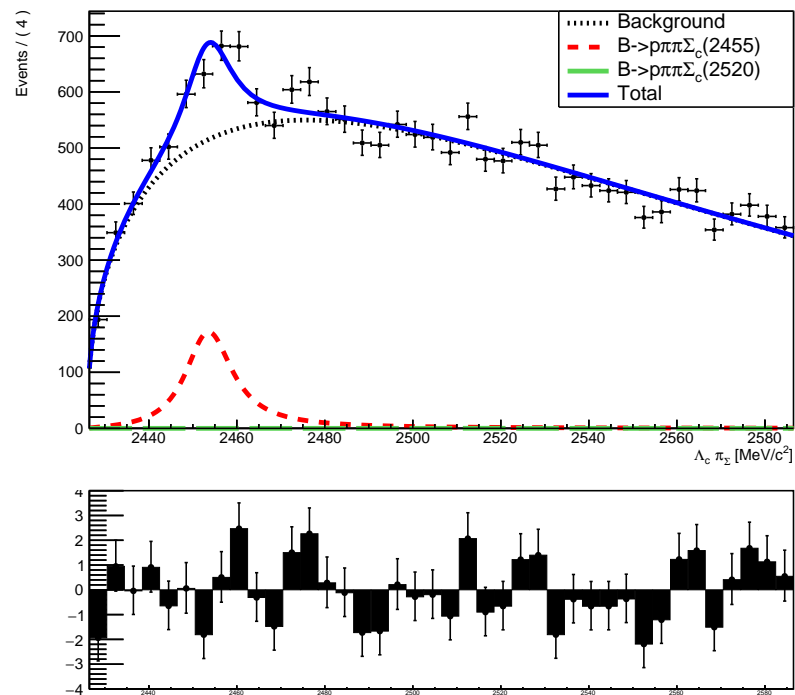


[a]

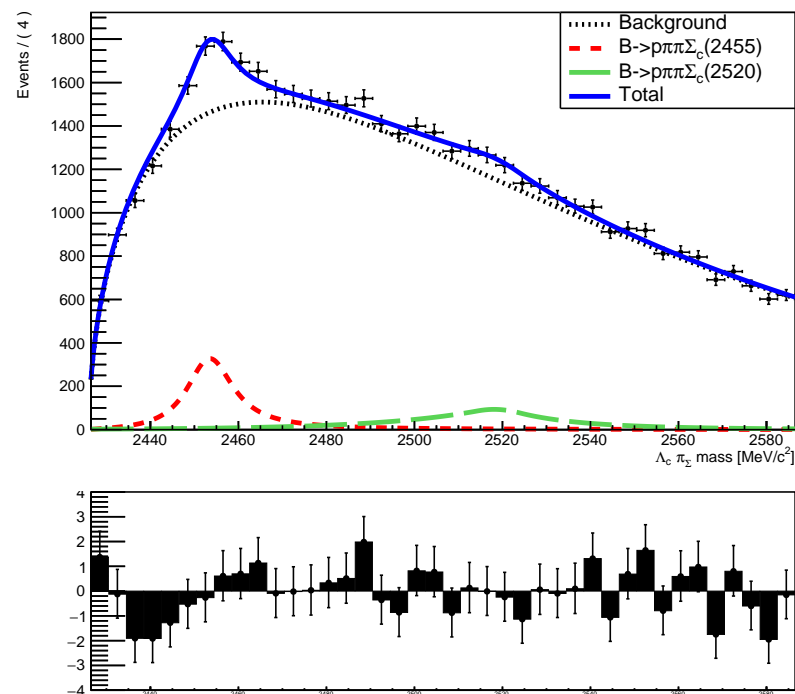


[b]

Figure 2.21: Fit result for PartReco line of MagUp [a] and MagDown [b] 2012 subsamples in the reduced mass range.



[a]



[b]

Figure 2.22: Fit result for PartReco lines of 2011 [a] and 2012 [b] samples in the reduced mass range quoted in the text.

MEASUREMENT OF THE RELATIVE BRANCHING
FRACTION $B_u^+ \rightarrow p\pi^+\pi^+\bar{\Sigma}_c(2520)^{-}$

The B_u^+ decay mode selected to measure the Λ_c absolute branching fraction contains $p\pi^+\pi^+\pi^-\bar{\Lambda}_c^-$ in the final state. No requirement was imposed on the combination $\pi^-\bar{\Lambda}_c^-$ to be consistent with the mass of the Σ_c when the selection was applied on the FullReco sample, where the $pK\pi$ decay products of the Λ_c were also detected.

In principle, besides the $\Sigma_c(2455)$, other Σ_c resonances besides the $\Sigma_c(2455)$ could be produced in the decay of the B_u meson, and indeed while performing the measurement of the absolute branching fraction of $\Lambda_c \rightarrow pK\pi$, an excess of events around 2520 MeV/ c^2 in the $\Lambda_c\pi$ mass spectrum was observed, as mentioned in Section 2.3.

Baryonic B-decays could improve the understanding of b-quark hadronisation into baryons. At the same time, the large value of the B mass allows a wide spectrum of baryons of different masses and flavours, at the final state, thus making these decays very useful in the search for exotic baryons.

Experimentally, an ordering is observed in the relative branching fractions of baryonic decays; decays with only a baryon-antibaryon pair have in fact smaller branching fractions than those containing in addition one pion and these modes, in turn, are less frequent than those with two or three pions.

This feature is confirmed by the soft momentum spectrum shown by the Λ_c in inclusive studies [19] [20].

Furthermore the decays of the type $B^- \rightarrow \Lambda_c^+ \bar{p} n \pi$ receive contributions from intermediate states involving Σ_c resonances, neutral or doubly charged.

In addition, in the decays $B_u^0 \rightarrow \bar{p}\pi^-\Sigma_c(2455)^{++}$ the rate as function shows an enhancement near threshold when compared with the rate of $B_u^0 \rightarrow \bar{p}\pi^+\Sigma_c(2455)^0$. A number of models has been developed to explain this feature [21], which can be understood qualitatively if one assumes that the partial decay width is proportional to $\alpha_s(q^2)$

and to the gluon propagator $\frac{1}{q^2}$. Therefore soft gluons are preferred and thus baryon pairs of small masses. Pole models [22] are invoked to explain why doubly charged Σ_c 's are produced via soft gluons, while neutral Σ_c 's through hard gluons.

Therefore a measurement of the branching fraction of the decay $B_u^+ \rightarrow p\pi^+\pi^+\bar{\Sigma}_c(2520)^{--}$ is decay relative to $B_u^+ \rightarrow p\pi^+\pi^+\bar{\Sigma}_c(2455)^{--}$ is well worth.

Globally a seven-tracks final state directly observed through the decays $\Sigma_c \rightarrow \Lambda_c\pi$ and $\Lambda_c \rightarrow pK\pi$ thus enhances the interest on this observation and measurement, being a proof of the LHCb detector capabilities and excellent performance.

In the following sections, the strategy followed to select and extract signal events, and the results obtained will be presented.

The charge conjugate decay is considered as well throughout this work.

3.1 Analysis strategy

This section will be devoted to the explanation of the analysis strategy planned and followed to perform the measurement.

3.1.1 Determination of the relative branching ratio

The branching fraction $B_u^+ \rightarrow p\pi^+\pi^+\bar{\Sigma}_c(2520)^{--}$ is computed with respect to the normalization channel $B_u^+ \rightarrow p\pi^+\pi^+\bar{\Sigma}_c(2455)^{--}$ as follows:

$$\mathcal{B}(B_u^+ \rightarrow p\pi^+\pi^+\bar{\Sigma}_c(2520)^{--}) = \mathcal{B}(B_u^+ \rightarrow p\pi^+\pi^+\bar{\Sigma}_c(2455)^{--}) \cdot \frac{N_{B_u^+ \rightarrow p\pi^+\pi^+\bar{\Sigma}_c(2520)^{--}}^{raw}}{N_{B_u^+ \rightarrow p\pi^+\pi^+\bar{\Sigma}_c(2455)^{--}}^{raw}} \cdot \epsilon_{rel}$$

where $\mathcal{B}(B_u^+ \rightarrow p\pi^+\pi^+\bar{\Sigma}_c(2455)^{--}) = (3.0 \pm 0.8) \cdot 10^{-4}$ is the branching fraction of the normalization channel according to [1].

The term ϵ_{rel} is the relative efficiency for the two decay modes, defined as the ratio between $\epsilon_{B_u^+ \rightarrow p\pi^+\pi^+\bar{\Sigma}_c(2455)^{--}}$ and $\epsilon_{B_u^+ \rightarrow p\pi^+\pi^+\bar{\Sigma}_c(2520)^{--}}$, i.e. the total efficiency obtained for the normalisation and the signal channels, respectively.

where $\epsilon_{B_u^+ \rightarrow p\pi^+\pi^+\bar{\Sigma}_c(2455)^{--}}$ and $\epsilon_{B_u^+ \rightarrow p\pi^+\pi^+\bar{\Sigma}_c(2520)^{--}}$ are the total efficiency obtained for the normalization and the signal channel, respectively.

Those efficiencies take into account the totality of the effects of detection, reconstruction and selection peculiar of both the detector and the analysis.

Candidates selected through a dedicated stripping line were analysed through further selection based on trigger, invariant mass and PID variables and a Boosted Decision Tree, designed to enhance the two resonant contributions.

Efficiencies have been computed by exploiting dedicated MonteCarlo samples and the systematic uncertainties, which are largely overwhelmed by statistical errors, have been obtained through specific methods which will be discussed in the following.

Interference effects can in principle involve the $B_u^+ \rightarrow p\pi^+\pi^+\bar{\Sigma}_c(2455)^{--}$ and $B_u^+ \rightarrow p\pi^+\pi^+\bar{\Sigma}_c(2520)^{--}$ channels and the non-resonant $B_u^+ \rightarrow p\pi^+\pi^+\pi^-\bar{\Lambda}_c^-$ one. Since the

spin of the $\Sigma_c(2455)^{++}$ and of the $\Sigma_c(2520)^{++}$ are different, no interference involving these two components should be taken into account. However, this type of effect will be not discussed in this thesis and will be treated out of this contest in the near future.

However, this class of effects is not and it is expected to have a negligible repercussion on the ratio between their branching fractions at this level. For this reason, interference effects will not be discussed in this thesis.

During a preliminary analysis, two more channels were visible in the data sample. In fact, with the same particles in the final state, it is possible to combine the Λ_c with a pion of opposite sign of charge. The invariant mass computed in this manner showed a resonance peak around $2455 \text{ MeV}/c^2$, originated from the $B_u^+ \rightarrow p\pi^+\pi^-\bar{\Sigma}_c(2455)^0$ decay, as it was expected. A peak around $2520 \text{ MeV}/c^2$ was observed as well, being the first observation of the decay $B_u^+ \rightarrow p\pi^+\pi^-\bar{\Sigma}_c(2520)^0$.

However, the decay into neutral Σ_c 's will not be discussed further in this work, except for the aspects which are essential to the measurement performed, but will be topic of a different analysis at a later stage.

3.2 Selection of signal events

Unlike the analysis aimed to measure the absolute branching fraction of $\Lambda_c \rightarrow pK\pi$, the measurement of this relative branching fraction is based on the detection and complete reconstruction of all the particles in the final state.

Thanks to the excellent performance of the LHCb detector, it is possible to select a sample of data of high purity, efficiently suppressing combinatorial background in the B_u invariant mass spectrum.

Section 3.2.1 will be dedicated to an overview of the samples exploited to perform the measurement. Section 3.2.2 will be dedicated to the background contributions, while the selection strategy is presented in Section 3.2.3.

3.2.1 Samples

In the following sections, data and MonteCarlo samples exploited in order to perform the relative branching fraction of the decay $B_u^+ \rightarrow p\pi^+\pi^+\bar{\Sigma}_c(2455)^{-}$ will be discussed.

Data

The data sample analysed corresponds to an integrated luminosity of 3 fb^{-1} collected during 2011 and 2012 pp collisions by the LHCb detector.

Table 3.1 shows in detail the integrated luminosity corresponding to the data sample, classified according to the magnet configuration.

3.2.1.1 MonteCarlo

Studies on signal and background contributions and efficiencies have been performed using various MonteCarlo samples specifically generated for the purpose.

Year	Polarity	Luminosity [pb^{-1}]
2011	Mag Up	413.012 ± 7.06251
2011	Mag Down	559.132 ± 9.56115
2012	Mag Up	936.522 ± 10.8637
2012	Mag Down	956.596 ± 11.0965

Table 3.1: Integrated luminosity corresponding to data analysed.

After a preliminary study and plan of the analysis strategy, the following samples were produced:

- $\Sigma_c(2455)^{++}$ sample, simulating the chain $B_u^+ \rightarrow p\pi^+\pi^+\bar{\Sigma}_c(2455)^{-}(\rightarrow \bar{\Lambda}_c^-\pi^-)$
- $\Sigma_c(2520)^{++}$ sample, simulating the decay chain $B_u^+ \rightarrow p\pi^+\pi^+\bar{\Sigma}_c(2520)^{-}(\rightarrow \bar{\Lambda}_c^-\pi^-)$
- *non-resonant* sample, simulating the decay chain $B_u^+ \rightarrow p\pi^+\pi^+\bar{\Lambda}_c^-\pi^-$
- $\Sigma_c(2455)^0$ sample, simulating the decay chain $B_u^+ \rightarrow p\pi^+\pi^-\bar{\Sigma}_c(2455)^0(\rightarrow \bar{\Lambda}_c^-\pi^+)$
- $\Sigma_c(2520)^0$ sample, simulating the decay chain $B_u^+ \rightarrow p\pi^+\pi^-\bar{\Sigma}_c(2520)^0(\rightarrow \bar{\Lambda}_c^-\pi^+)$

The events were of the type "filtered MonteCarlo", already defined, and details on the size of the various event samples in different configurations are shown in Table 3.3.

In all samples, the Λ_c is forced to decay exclusively in the $pK\pi$ final state, as it is through this mode that it is reconstructed. As for the analysis presented in the first part of this thesis, this final state can be reached via resonant or not resonant modes, with relative ratios in agreement with those cited in [1] and reported in Table 3.2.

Mode	Branching fraction
$\Lambda_c^+ \rightarrow p\bar{K}^-\pi^+$	2.8%
$\Lambda_c^+ \rightarrow \Lambda(1520)\pi^+$	1.8%
$\Lambda_c^+ \rightarrow \Delta(1232)^{++}K^-$	0.86%
$\Lambda_c^+ \rightarrow p\bar{K}^*(892)^0$	1.6%

Table 3.2: Absolute branching fractions of Λ_c with final state $pK\pi$ from PDG.

In all cases the B_u produced was forced to decay into the channel of interest and only events with all the tracks within the LHCb acceptance have been tracked and simulated.

While it is easy to understand the need for the $\Sigma_c(2455/2520)^{++}$ and *non-resonant* samples, at this point of the dissertation it may be surprising the appearance of samples corresponding to three new decay modes, two of which have not been observed so far up to this thesis, namely $B_u^+ \rightarrow p\pi^+\pi^-\bar{\Sigma}_c(2520)^0$ and $B_u^+ \rightarrow p\pi^+\pi^+\bar{\Sigma}_c(2800)^{-}$.

In fact, preliminary studies on data showed some interesting hints concerning the possibility to observe those new decays.

Sample	2011		2012	
	MagUp	MagDown	MagUp	MagDown
$\Sigma_c(2455)^{++}$	5182	5156	7859	9478
$\Sigma_c(2520)^{++}$	7356	5949	13401	12367
<i>non-resonant</i>	6566	5981	11145	12861
$\Sigma_c(2455)^0$	1971	2011	3767	3692
$\Sigma_c(2520)^0$	4452	4563	4042	7342

Table 3.3: Signal events in filtered MonteCarlo samples.

However, while the $B_u^+ \rightarrow p\pi^+\pi^+\bar{\Sigma}_c(2800)^{--}$ mode will be discussed and taken into account in this work, the study and branching fraction measurement of the $B_u^+ \rightarrow p\pi^+\pi^-\bar{\Sigma}_c(2520)^0$ decay mode, which is clearly visible and therefore observed for the first time, will be analysed out of this context.

The samples concerning all modes but the $\Sigma_c(2455/2520)^{++}$ have been used to understand and model as needed sources of background, which will be discussed in Section 3.2.2.

All the samples have been produced following the "filtered Montecarlo" procedure, by simulating and running the tracking and the reconstruction only for the events which pass the stripping selection.

Since the events which are expected not to survive the stripping selection are not saved in a format readily available, a further step is needed in order to access this information and be able to compute reconstruction and stripping efficiencies.

3.2.2 Background contributions

Background is expected to come from three main sources, namely:

- combinatorial background;
- non-resonant background;
- neutral Σ_c 's background.

Combinatorial background

Combinatorial background comes from random combinations of tracks without a specific physical source, giving origin to candidates which may survive selections. This component can be numerically evaluated directly from data fitting the B_u invariant mass spectrum. In fact, random candidates are expected to have a flat distribution over the whole range and the contribution under the peak can be easily estimated using mass regions adjacent to the B_u mass peak itself.

Non resonant background

Non resonant background is the contribution arising from the $B_u \rightarrow p\pi\pi\Lambda_c\pi$ decay. These events stand under the signal region in the B_u mass spectrum, defined as ± 30 MeV/ c^2 around the B_u nominal mass (5279 MeV/ c^2). However, since in this work the aim is to measure the ratio between the channel of interest and that of normalisation, the non resonant events will be considered as a non-signal contribution.

Neutral modes contributions

Neutral Σ_c 's contribution collects all the events whose origin are the $B_u^+ \rightarrow p\pi^+\pi^-\bar{\Sigma}_c(2455)^0$ or $B_u^+ \rightarrow p\pi^+\pi^-\bar{\Sigma}_c(2520)^0$ decays. In fact, as it will be explained in the following sections, in the $\Lambda_c^+\pi^+$ invariant mass spectrum these channels produce a background, whose shape is compatible with that of the combinatorial contribution.

3.2.3 Selection strategy

The candidates are selected through four main stages, explained in the following sections:

1. Stripping selection (see Section 3.2.3.1);
2. Trigger selection (see Section 3.2.3.2);
3. Multivariate Boosted Decision Tree (BDT) selection (see Section 3.2.3.3);
4. PID selection (see Section 3.2.3.4);
5. Multiplicity of candidates (see Section 3.2.3.5);
6. Invariant mass and Decay Tree Fitter [23] boundaries (see Section 3.2.3.6);

An optimization procedure was applied in order to choose a combination of BDT and PID cuts to maximise the signal-to-background ratio, defined as follows:

$$R = \frac{S}{\sqrt{S+B}}$$

where S is the number of resonant signal events, and B is the number of background events in the $\Sigma_c(\Lambda_c^+\pi^+)$ invariant mass spectrum.

The values obtained will be reported in Section 3.2.3.3 and 3.2.3.4.

3.2.3.1 Stripping selection

A dedicated stripping selection was written in order to enhance signal candidates and suppress background contribution.

Candidates are built with a leaf-to-root/bottom-to-top approach, starting from requiring the presence of a Λ_c reconstructed in $pK^-\pi^+$, then proceeding from these final state particles up to the top of the decay chain, namely the B_u .

A detailed overview of these selection criteria is reported in Table 3.4.

Candidate	Variable	Cut
B_u	mass window	± 200 MeV
	DOCAMAX	= 0.2 mm
	χ^2 VNDOF	< 5 5.0
	FD χ^2	> 64
	DIRA	> 0.998
$p\pi^+\pi^+$ candidate	invariant mass	1.5 – 2.8 GeV
	DOCAMAX	= 0.15 mm
	χ^2 VNDOF	< 5
	FD χ^2	> 49
	minimum IP χ^2	> 6
	P_T	> 1 GeV
Λ_c	mass window	± 100 MeV
	FD χ^2	> 36
	χ^2 VNDOF	< 5.0
	DIRA	> 0.98
	DOCAMAX	= 0.5 mm
	P_T	> 0 GeV
Λ_c daughters	p	> 2 GeV
	P_T	> 250 MeV
	minimum IP χ^2	> 8
	proton PID($p - \pi$)	> -5
	kaon PID($K - \pi$)	> -5
Σ_c	FD χ^2	> 36
	χ^2 VNDOF	< 10.0
	DOCAMAX	= 0.2 mm

Table 3.4: Cuts applied in the stripping selection. An exhaustive explanation for variables not yet defined and contained in this table is available in Appendix A.

3.2.3.2 Trigger requirements

Dealing with trigger configurations, the L0 hadronic channel and the HLT2 four-body topological trigger lines to be fired by one of the seven tracks reconstructed to form a B candidate (TOS).

Trigger Level	Selection requirement on $p\pi_1\pi_2\pi_\Sigma$
L0	LOHadron_TOS
HLT1	Hlt1TrackAllL0_TOS
HLT2	Hlt2Topo4BodyBBDTDecision_TOS

Table 3.5: Trigger selection requirements.

The TOS requirements made on the data sample are listed in Table 3.5.

3.2.3.3 Multivariate selection

As in the analysis discussed in the previous chapter, a BDT has been implemented to enhance the resonant signal over the combinatorial background and the non resonant components.

The method has been tuned using variables related to B_u and Λ_c , which are listed in Table 3.6.

The training samples used for signal were two MonteCarlo samples relative to the signal and the normalization channels, $B_u^+ \rightarrow p\pi^+\pi^-\bar{\Sigma}_c(2520)^{--}$ and $B_u^+ \rightarrow p\pi^+\pi^-\bar{\Sigma}_c(2455)^{--}$, respectively, with requirements on the true identity and correct lineage of tracks.

A data sample with same requirements as signal on HLT2 trigger, but extracted from a region at higher mass than signal in the B_u invariant mass spectrum, was instead used as training sample for background.

Two different BDTs with common variables were tuned separately for 2011 and 2012, and for each year, the BDT final variable was computed for candidates with an even RunNumber through a BDT trained on odd-RunNumber events, and vice versa.

The ROC curves relative to 2011 and 2012 BDTs are shown separately in Figure 3.1.

Candidate	Variable
B_u	FD ownpv FD χ^2 ownpv DIRA IP χ^2 vertex χ^2
Λ_c	FD ownpv FD χ^2 ownpv DIRA IP χ^2 vertex χ^2 P_T
B_u daughters	proton P_T proton IP χ^2 $\pi_1 P_T$ $\pi_2 P_T$
π_Σ	P_T
$p\pi^+\pi^+\pi_{\Sigma_c}$ candidate	vertex χ^2 NDOF IP χ^2 DIRA

Table 3.6: Variables used in the BDT.

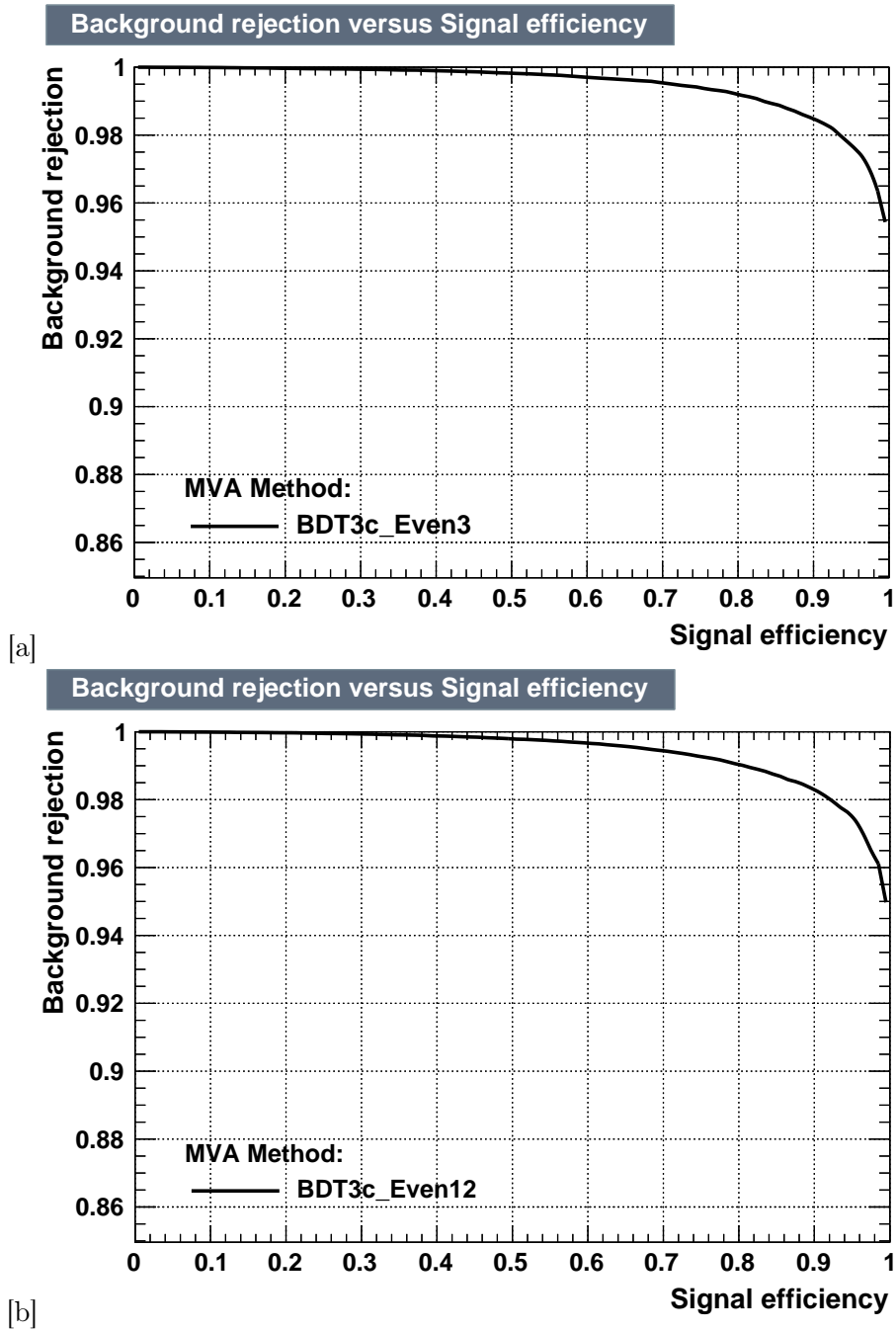


Figure 3.1: ROC curve for 2011 [a] and 2012 [b] BDTs.

The maximisation procedure for the ratio signal-to-background (see Section 3.2) led to the same BDT cut value for both years, equal to -0.1.

3.2.3.4 Particle Identification

The presence of two protons in the decay, combined with the excellent particle identification performance of the LHCb detector, simplifies appreciably the detection of signal candidates and sensibly enhance the rejection efficiency for background.

In this analysis, to select true protons, it was considered more effective the use of an approach different than the one adopted in Chapter 2. The so-called "ProbNN" variables were used instead.

It is a set of variables which have been developed to improve upon the simple log likelihood variables. They take into account correlations between different detector sub-systems, including additional information.

In fact, PID information coming from RICH, calorimeters and muon systems is combined through multivariate techniques, leading to a single probability value for each particle hypothesis.

The training of these multivariate analyses is performed on MonteCarlo inclusive B events, with one neural network per hypothesis and exclusive responses.

A different training sample leads to different versions of ProbNNs, with slightly different performance.

The choice among different tunings available in LHCb or more in general between single or combined PID variables depends strictly on the specific aim of the analysis, and the characteristics of data analysed, since in principle there is no *a priori* reason to prefer one variable rather than the others.

The complete set of PID cuts applied are reported in Table 3.7. As already explained in Section 3.2, the values have been determined through a signal-to-background maximisation procedure.

\mathcal{P}_B	\mathcal{P}_{Λ_c}
ProbNNp>0.4	ProbNNp>0.3

Table 3.7: PID requirements on the protons.

3.2.3.5 Multiple candidates

Only one candidate per event is accepted after the selection described in the previous sections and in case of multiplicity larger than one the choice between all possible candidates is performed randomly, for the reasons already explained in Section 2.2.3.5.

3.2.3.6 Invariant mass and *Decay-Tree Fitter*

As mentioned in 3.2.3.1, the mass window defined at stripping level for both B_u and Λ_c invariant masses is deliberately large. This was decided to allow a better understanding of the background around the signal region and a more precise estimation of the number

of signal candidates. However, as soon as the purpose is to analyse the Σ_c mass spectrum and extract signal yields, a tighter cut is mandatory.

The B_u mass window allowed is therefore tightened to ± 30 MeV/ c^2 around the nominal mass, which means 3 times the σ obtained through the fit performed on the B_u invariant mass spectrum, as will be explained in Section 3.3.2.

Concerning the Λ_c , a package using a method called "Decay Tree Fitter" [23] has been exploited to fit the decay chain of interest.

Very often in high energy physics the reconstruction of processes follows a bottom-up procedure. Starting from final state particles, the parameters of each decay vertex are extracted and these constraints are then applied to "upstream" particles.

Although it is a fast and easy method, this "leaf-by-leaf" approach does not allow the constraints upstream of a decay vertex to contribute to improve the knowledge of the parameters of the vertex.

The decay-tree fitter instead extracts all parameters in a decay chain simultaneously and it is hypothesis driven, meaning that it is possible to define the decay tree model adding both internal (i.e. momentum conservation at each vertex) and external constraints (i.e. final state tracks information) to the degrees of freedom typical of the procedure (i.e. positions of the vertices in the decay tree, momenta of particles). In this configuration, the mass of a final state particle can be assigned on the basis of the particle hypothesis in the decay tree.

In this analysis, we applied the Decay Tree Fitter to the entire decay chain, choosing as constraints the presence of a $\Lambda_c(2286)^{++}$ reconstructed through its decay into $pK\pi$. This mass hypothesis allows a cleaner Σ_c invariant mass spectrum, where resonances are expected to become better determined than they would without applying this procedure. No constraints have instead been applied to the B mass hypothesis, as this could modify and fake the Σ_c mass spectrum.

The Λ_c mass value imposed through this method is fixed at 2286 MeV/ c^2 .

A cut on a variable defining the quality of the global fit has then been applied to remove events which were mistakenly fitted by forcing them into the selected decay chain.

3.2.4 Data selected

The seven particles invariant mass spectrum of candidates selected as described in this section is shown in Figure 3.2. It is worth to notice the low level of background in the range [5179:5249] and [5309:5479] MeV/ c^2 (the so-called "flat-background region"), which reflects the power of the selection criteria adopted as well as the excellent performance of the LHCb detector. A significant excess of events is visible for masses lower than ~ 5180 MeV/ c^2 ("low-mass background region"). Since these events survived the strict selection applied to data, it is plausible to assume that they come from a physical source. The best hypothesis is that they are decays of a B_u into the $p\pi^+\pi^+\pi^-\pi^0\bar{\Lambda}_c^-$ channel with a missing π^0 .

Some preliminary studies were carried out on the $pK\pi$ and the $\Lambda_c\pi$ invariant mass spectra for the events in this region and details may be found in Appendix D. However, due to "stripping level" cuts, the spectrum falls to zero at 5079 MeV/ c^2 , making

impossible to perform a more detailed analysis.

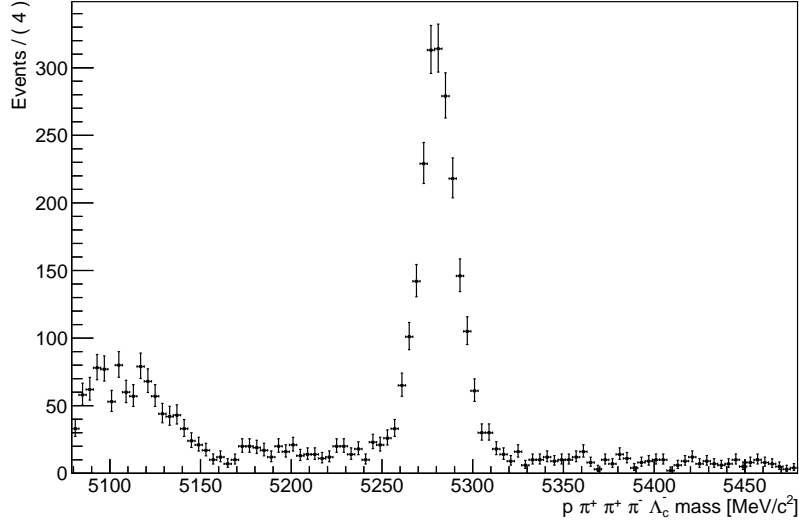


Figure 3.2: $p\pi^+\pi^+\bar{\Lambda}_c^-\pi^-$ invariant mass spectrum for the 2011+2012 data sample.

The $\Lambda_c^+\pi^+$ invariant mass spectrum for the events in the B_u signal region, namely [5250:5310] MeV/c^2 , is shown in Figure 3.3. The two resonances are clearly visible.

To corroborate the statement of Section 3.1 concerning the observation of the $\Sigma_c(2520)$ resonances, the $\Lambda_c^+\pi^-$ invariant mass spectrum too is shown in Figure 3.4. A clear evidence of the $\Sigma_c(2520)^0$ resonance is visible.

3.3 Signal extraction

3.3.1 Strategy

To extract the number of events relative to the signal $B_u^+ \rightarrow p\pi^+\pi^+\bar{\Sigma}_c(2520)^{-}$ and the normalisation $B_u^+ \rightarrow p\pi^+\pi^+\bar{\Sigma}_c(2455)^{-}$ channels, an unbinned maximum-likelihood fit was performed on the measured $\Lambda_c\pi\Sigma$ invariant mass spectrum.

3.3.2 Fit

To describe the $\Lambda_c\pi$ invariant mass spectrum, a fit on the seven particles of the final state was necessary, in order to define the signal region in the u mass spectrum, and identify as signal the events under the B_u peak. Therefore, a description of the procedures followed to perform this fit on the B_u and then on the $\Lambda_c\pi$ spectra is presented in the following.

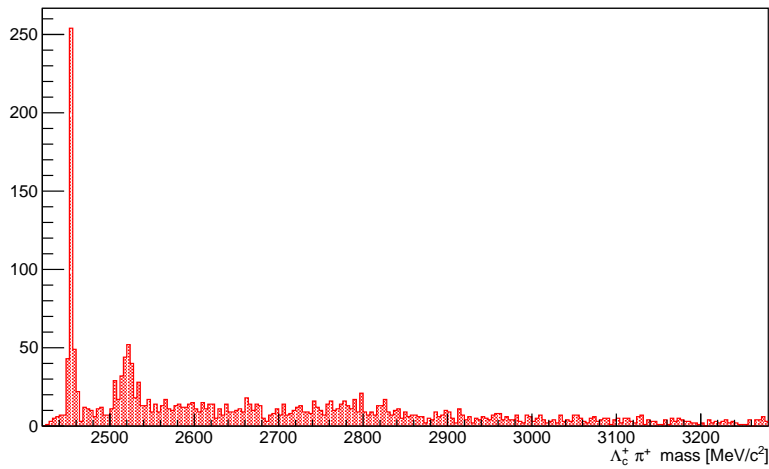


Figure 3.3: $\Lambda_c^+ \pi^+$ invariant mass spectrum for the 2011+2012 data sample.

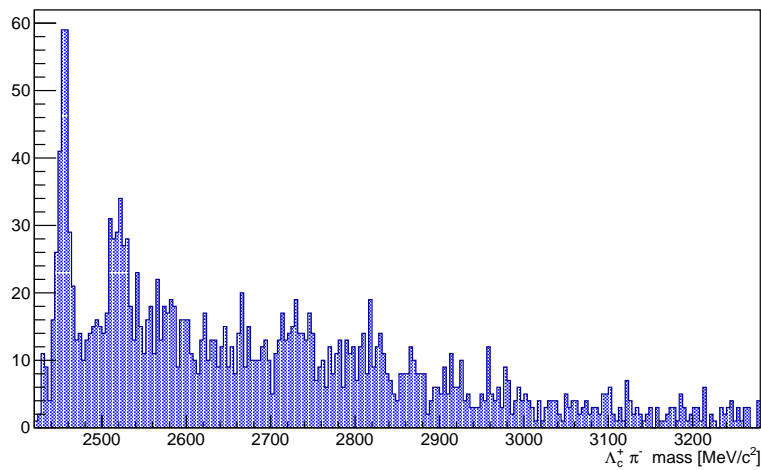


Figure 3.4: $\Lambda_c^+ \pi^-$ invariant mass spectrum for the 2011+2012 data sample.

3.3.2.1 Fit to the B_u invariant mass spectrum

An unbinned maximum likelihood fit was performed on the seven particles invariant mass spectrum for MonteCarlo events to fix the PDF describing the B_u mass peak, which was found to be a double crystal-ball.

The B_u signal in MonteCarlo data together with the result of the fit superimposed is shown in Figure 3.5 and the parameters listed in Table 3.8.

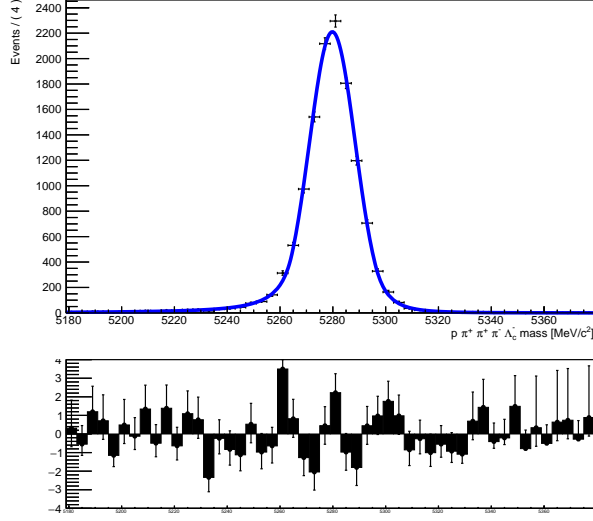


Figure 3.5: Fit result obtained on $p\pi^+\pi^+\bar{\Lambda}_c^-\pi^-$ invariant mass spectrum for the 2011+2012 Montecarlo sample.

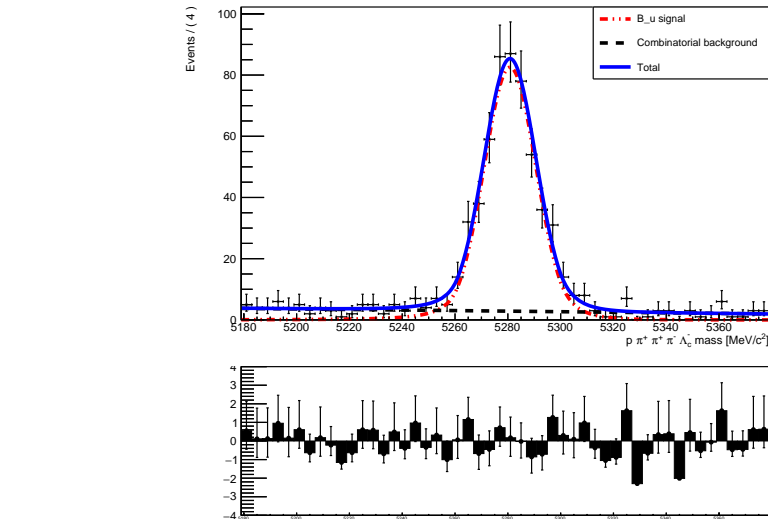
Parameters	Fit result
a1	1.76 ± 0.08
a2	1.90 ± 0.08
n1	2.0 ± 0.2
n2	4.5 ± 0.7
m	5279.8 ± 0.1
s	8.7 ± 0.1

Table 3.8: Parameters of the Double Crystal-Ball function for 2011 and 2012 MonteCarlo signal events. The first four parameters determine the shape of the tails, while the gaussian core is defined by the m and s parameters.

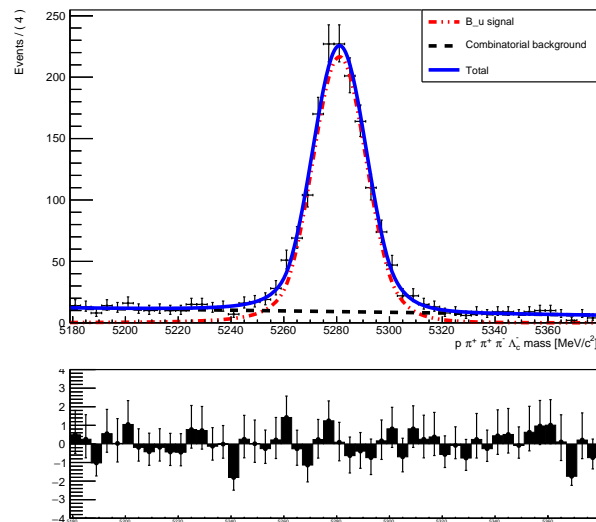
These parameters were then used as input for the fit to the 2011 and 2012 data samples separately, regardless of magnet polarity, in the mass range [5179:5379] MeV/c^2 to exclude the "low mass background region" mentioned in Section 3.2.4. In fact, some differences could be noted in the background for the two years, due to the different data-taking conditions, although the signal shape is predicted to be the same for both.

The results are shown in Figure 3.6[a] and [b].

The width of the signal in the fitting of the data sample was allowed to vary in a wider range with respect to that defined by the gaussian constraint obtained on MonteCarlo, so that the s parameter value fitted for data was 9.8 ± 0.5 for the 2011 sample and 10.2 ± 0.4



[a]



[b]

Figure 3.6: Fit results on the $p\pi^+\pi^+\bar{\Lambda}_c^-\pi^-$ invariant mass spectrum for the 2011 and 2012 data samples.

for the 2012.

The background contribution is described by a polynomial function.

The yields relative to the signal and background contributions, as well as the $S/(S+B)$ ratio computed in the signal region (defined within $\pm 3\sigma$ around the B_u nominal mass) are reported in Table 3.9 separately for the 2011 and 2012 samples. The purity of the sample

	2011	2012
Signal	523 ± 25	1443 ± 45
Background	143 ± 16	457 ± 32
S/(S+B) in signal region	92%	91%

Table 3.9: Yields result from a fit on the $p\pi^+\pi^+\bar{\Lambda}_c^-\pi^-$ invariant mass spectrum (B_u for the 2011 and 2012 samples).

is similar for 2011 and 2012 and, specifically, the fraction of signal events is numerically estimated to be 92% for the 2011 sample and 91% for the 2012 sample.

The ratio between the signal yields for the two years is slightly larger than one would expect from the relative luminosities.

3.3.2.2 Fit to the $\Lambda\pi$ invariant mass spectrum

The signal, the normalisation and the non resonant and neutral background contributions line shapes were fixed from MonteCarlo performing a fit to the relevant data using the same technique of unbinned maximum likelihood.

The same selection, tuned for the data sample and explained in Section 3.2.3, was applied to the MonteCarlo detector level, with further requirements on the true identity and correct origin of particles, prior to the fitting procedure.

Even though the data-taking conditions and selections were different, for the various contributions the fit gave compatible results for the 2011 and the 2012 samples. For this reason, all MonteCarlo samples, regardless of year and magnet polarities, were fitted together.

When fitting the data, all parameters of each contribution were allowed to vary within a gaussian constraint, having as mean value that obtained when fitting the MC sample and as standard deviation the uncertainty coming from the fit itself.

The PDF describing combinatorial background was obtained by fitting the sidebands of the B_u peak in the m_B invariant mass spectrum, in order to exclude any possible contribution originated by B_u decays.

Signal contribution

The parameters of the PDF for the $B_u^+ \rightarrow p\pi^+\pi^+\bar{\Sigma}_c(2520)^{-}$ component were extracted by fitting a selected MonteCarlo sample simulating this decay.

The PDF function describing the signal component $P_{\Sigma_c(2520)^{++}}$ is a double Crystal-Ball [17] and the parameters fitted are available in Table 3.10, while the fit result is shown in Figure 3.7, superimposed to MonteCarlo data.

The fact that the width of the gaussian core of this contribution is small (see parameter s in Table 3.10) is a natural consequence of the application of Decay-Tree Fitter and the excellent momentum resolution of the LHCb experiment.

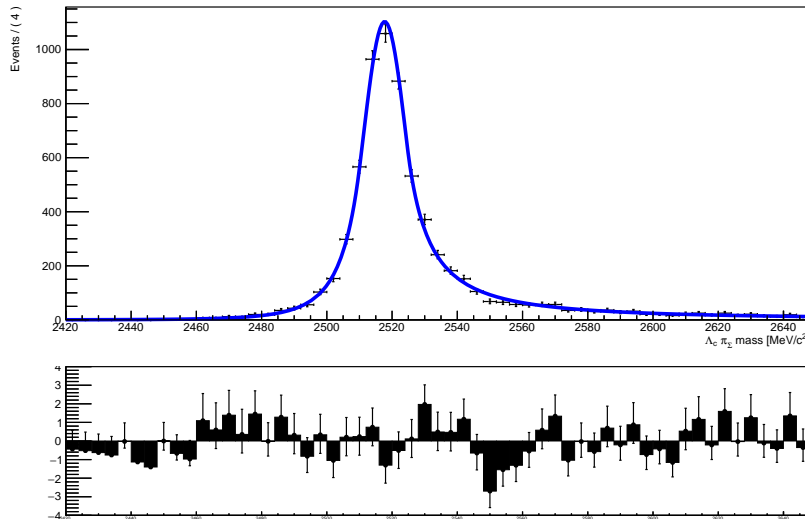


Figure 3.7: Fit result obtained on $\bar{\Lambda}_c^- \pi^-$ invariant mass spectrum for the $B_u^+ \rightarrow p\pi^+\pi^+\bar{\Sigma}_c(2520)^{--}$ 2011+2012 MonteCarlo sample.

Parameters	Fit result
a1	1.14 ± 0.07
a2	1.03 ± 0.04
n1	5.1 ± 0.8
n2	1.52 ± 0.07
m	2517.7 ± 0.2
s	6.6 ± 0.2

Table 3.10: Parameters of the Double Crystal-Ball function for 2011 and 2012 MonteCarlo $\Sigma_c(2520)^{++}$ signal events. The first four parameters determine the shape of the tails, while the gaussian core is defined by the m and s parameters.

A comparison between the spectra obtained for true signal events on this MonteCarlo sample before and after the application of Decay-Tree Fitter is shown in Figure 3.8.

Normalisation contribution

As for signal contribution, the PDF describing the one related to the normalisation decay mode $B_u^+ \rightarrow p\pi^+\pi^+\bar{\Sigma}_c(2455)^{--}$ is a double Crystal-Ball function.

The parameters which fix its line shape were extracted by fitting the corresponding MonteCarlo sample and are reported in Table 3.11.

It is worth describing that the width of the normalisation contribution is clearly

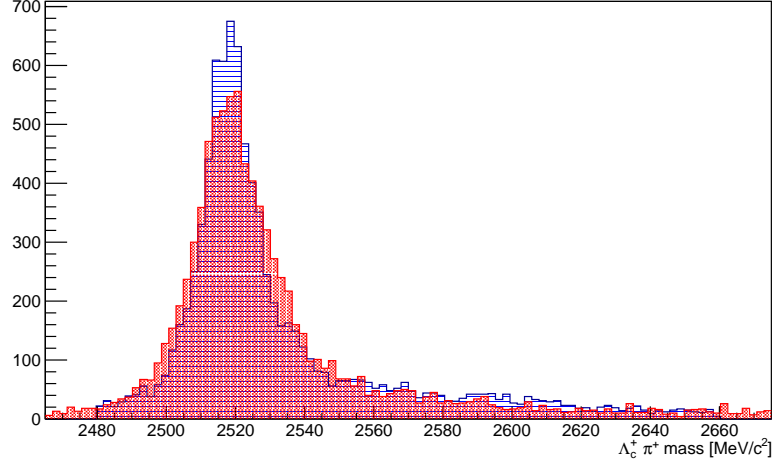


Figure 3.8: $\bar{\Lambda}_c^- \pi^-$ invariant mass spectrum for the $B_u^+ \rightarrow p\pi^+\pi^+\bar{\Sigma}_c(2520)^{-}$ MonteCarlo events before (in red) and after (in blue) the application of Decay-Tree Fitter.

Parameters	Fit result
a1	1.12 ± 0.06
a2	1.08 ± 0.06
n1	3.6 ± 0.3
n2	2.6 ± 0.1
m	2453.99 ± 0.03
s	1.4 ± 0.05

Table 3.11: Parameters of the Double Crystal-Ball function for 2011 and 2012 MonteCarlo $\Sigma_c(2455)^{++}$ signal events. The first four parameters determine the shape of the tails, while the gaussian core is defined by the m and s parameters.

smaller than that of the signal. This is due to a the fact that the natural width of this resonance is much smaller than that of the $\Sigma_c(2520)$ and to the proximity of this resonance to the kinematical threshold. The result of the fit is shown in Figure 3.9.

Non resonant contribution

The PDF describing the non resonant contribution was found to be the product of an exponential and a power function:

$$P_{nores} = (x - x_{th})^\alpha \cdot \exp\left(-\frac{x - x_{th}}{\beta}\right)$$

where x_{th} is the kinematical threshold.

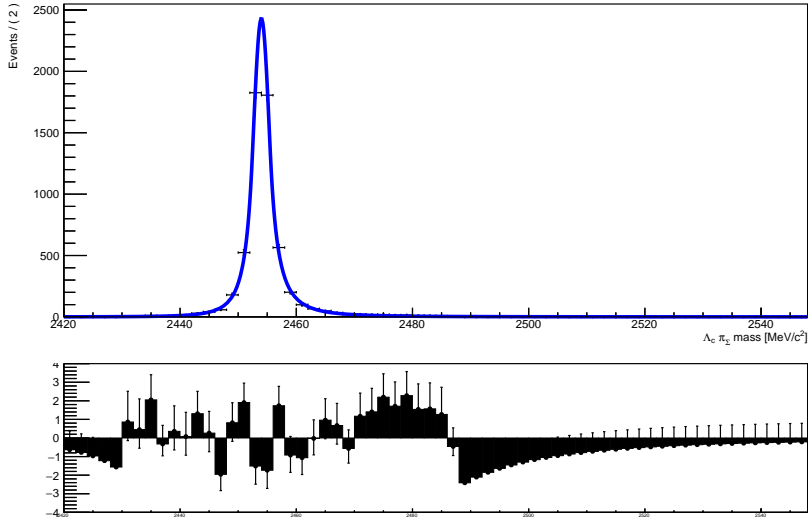


Figure 3.9: Fit result obtained on $\bar{\Lambda}_c^- \pi^-$ invariant mass spectrum for the $B_u^+ \rightarrow p\pi^+\pi^+\bar{\Sigma}_c(2455)^--$ 2011+2012 MonteCarlo sample.

Parameter	Fit result
α	0.905 ± 0.003
β	219 ± 3

Table 3.12: Fitted parameters for the non resonant contribution.

The parameters α and β are shown in Table 3.12 and the resulting function is superimposed to the MonteCarlo for this decay in Figure 3.10.

Neutral contribution

Neutral contributions whose origin are the known $B_u^+ \rightarrow p\pi^+\pi^-\bar{\Sigma}_c(2455)^0$ and the $B_u^+ \rightarrow p\pi^+\pi^-\bar{\Sigma}_c(2520)^0$ observed for the first time in this work were fixed by fitting the relative MonteCarlo samples, as well as the other contributions described up to this point.

Although in the neutral charge combination $\Lambda_c^+ \pi^-$ these contributions peak around 2455 and 2520 MeV/c^2 , in the $\Lambda_c^+ \pi^+$ invariant mass spectrum, they are both described by a function similar to that used to describe the non resonant contribution, i.e.

$$P_{neu} = (x - x_{th})^\alpha \cdot \exp\left(-\frac{x - x_{th}}{\beta}\right)$$

The parameters obtained in the two MonteCarlo samples are in agreement and are reported in Table 3.13.

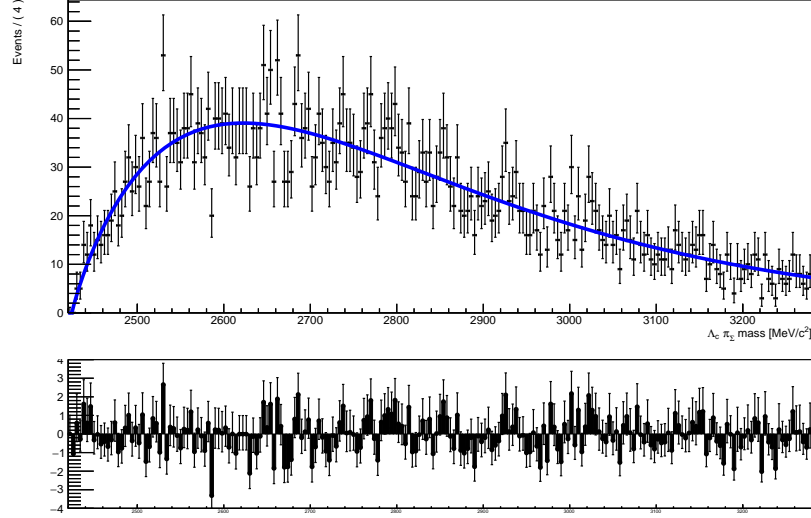


Figure 3.10: Fit result obtained on $\Lambda_c^- \pi^-$ invariant mass spectrum for the $B_u^+ \rightarrow p\pi^+\pi^+\pi^-\bar{\Lambda}_c^-$ 2011+2012 Montecarlo sample.

Parameter	Fit result
α	1.0 ± 0.1
β	280 ± 32

Table 3.13: Background fitted parameters.

Combinatorial contribution

As explained in Section 3.2.2, the combinatorial contribution is due to random combinations of tracks external to the decay.

For this reason, the only way to estimate it is to study this component in data.

All the contributions described in the preceding are originated by the decay of a B_u , meaning that the invariant mass of the seven particles in the final state (namely $p\pi^+\pi^+\pi^-\bar{p}_\Lambda K_\Lambda^+\pi_\Lambda^-$) is expected to be measured around the B_u nominal mass.

Combinatorial candidates instead do not fulfil this requirement, and their distribution in the B_u mass spectrum is expected to be almost flat throughout the whole range.

For this reasons, to extract the PDF describing the combinatorial contribution in the $\Lambda^+\pi^+$ invariant mass spectrum, a fit was performed on the the events whose mass is out of the B_u signal region (sidebands).

The function used is:

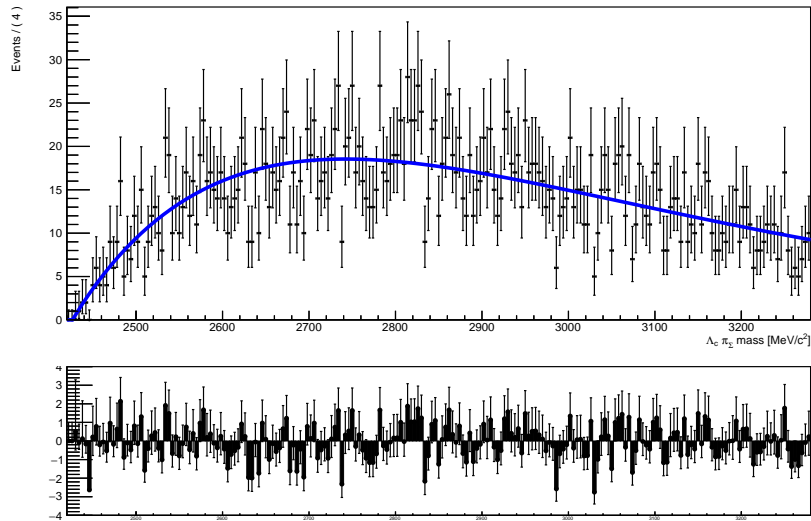


Figure 3.11: Fit result obtained on $\Lambda_c^+ \pi^+$ invariant mass spectrum for the $B_u^+ \rightarrow p \pi^+ \pi^+ \bar{\Sigma}_c(2455)^0$ 2011+2012 Montecarlo sample.

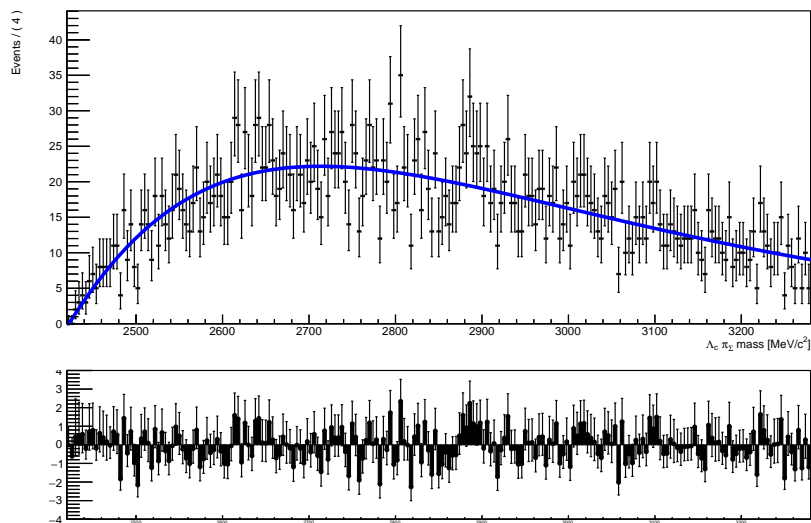


Figure 3.12: Fit result obtained on $\Lambda_c^+ \pi^+$ invariant mass spectrum for the $B_u^+ \rightarrow p \pi^+ \pi^+ \bar{\Sigma}_c^0$ 2011+2012 Montecarlo sample.

$$P_{comb} = (x - x_{th})^\alpha \cdot \exp\left(-\frac{x - x_{th}}{\beta}\right)$$

and the values obtained are in agreement with those presented in Table 3.13, although these are affected by larger errors due to the limited statistics.

For this reason, neutral and combinatorial contributions were described by the same PDF in the final procedure.

Total PDF and fit results

The total PDF describing the $\Lambda_c^+\pi^+$ mass spectrum is defined in the following:

$$P_{tot} = f_{sign(2520)} \cdot P'_{\Sigma_c(2455)^{++}} + f_{sign(2520)} \cdot P'_{\Sigma_c(2520)^{++}} + f_{nores} \cdot P'_{nores} + f_{bkg} \cdot P'_{bkg}$$

where $P'_{\Sigma_c(2520)^{++}}$ and $P'_{\Sigma_c(2455)^{++}}$ indicate the two doubly charged Σ_c 's components, multiplied by the functions expressing the gaussian constraints to the respective parameters. P'_{nores} and P'_{bkg} are the non resonant and the combinatorial plus neutral contributions, respectively, also multiplied by the respective gaussian constraints.

At the end of the fitting procedure, no dependence of the results on magnet polarities was observed. This is possible since, as it will be shown in the following sections, neither the efficiencies nor the systematic errors depend on the polarity of the magnet.

For this reason all the fitting results are presented regardless of the orientation of the magnetic field during data taking, allowing a larger statistic and smaller uncertainties.

In addition, since the PDFs of the single contributions are common, a simultaneous unbinned maximum likelihood fit was performed on these two samples.

The numerical results and the raw relative branching fraction are reported in Table 3.14, while the results of the fit are shown in Figure 3.13 together with the data.

	2011	2012
$\Sigma_c(2520)^{++}$	67 ± 13	165 ± 24
$\Sigma_c(2455)^{++}$	101 ± 12	255 ± 24
\mathcal{B}_{raw}^{rel}	0.66 ± 0.15	0.65 ± 0.11

Table 3.14: Yields and raw relative branching fraction for 2011 and 2012 samples. The errors are from the fit.

It is worth observing that in the figures the non-resonant and background components seem to have different ratios in the two years. This may be due to different efficiencies in 2011 and 2012 or to the fit procedure. In fact, since the PDF describing them are similar, it is hard to define exactly their relative ratio with small statistics and this reflects in large errors in the fit for these components.

Observing carefully the pull distribution around $2800 \text{ MeV}/c^2$, it can be noted that this region seems not to be perfectly described by the fitting function. It could be an

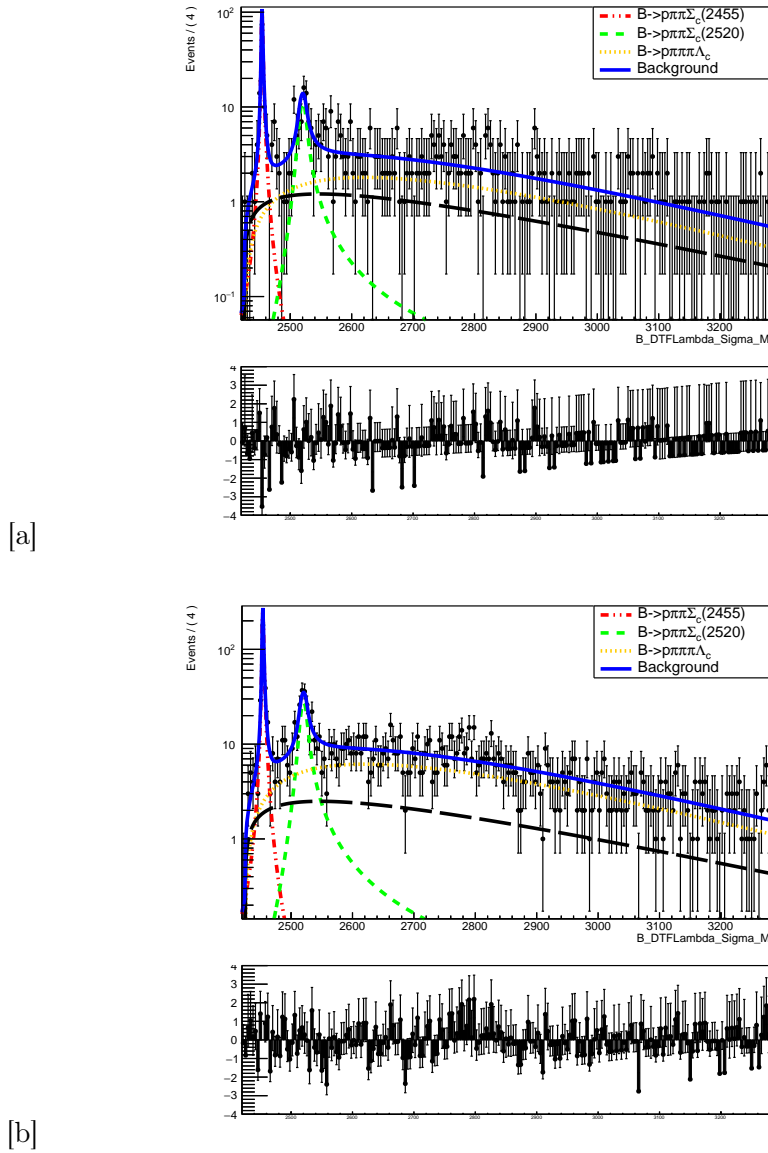


Figure 3.13: Fit results for 2011 and 2012 samples.

hint of the presence of the resonance $\Sigma_c(2800)$. Further studies will be performed in the future on this possibility.

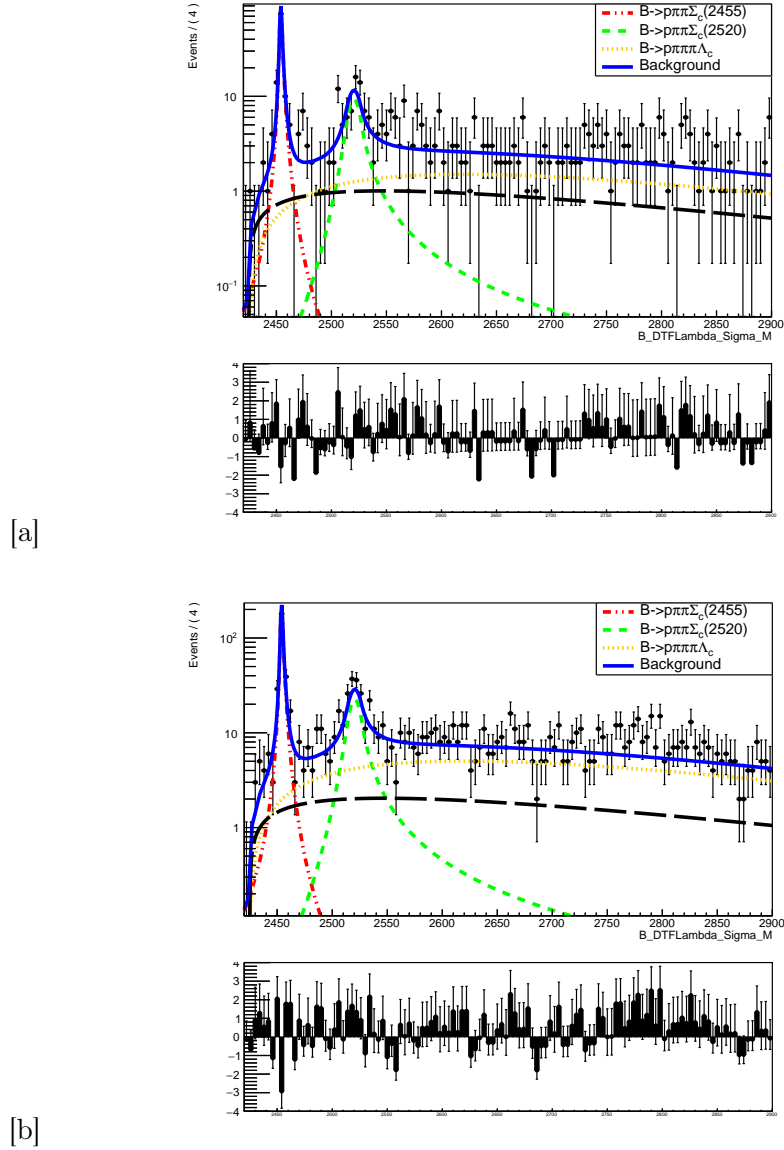


Figure 3.14: Fit results for 2011 and 2012 samples shown in the reduced mass range [2420:2800] MeV/c².

3.4 Efficiencies

To correct the raw relative ratio of branching fraction extracted from data, it is necessary to compute the total relative efficiency ϵ_{rel} , to which several sources contribute, namely:

- stripping and pre-stripping (acceptance, detection and reconstruction)

- selection (post stripping).

While the MonteCarlo samples allow a straightforward calculation for post stripping selection efficiencies (point 2 of the preceding itemized list), a different approach is needed to compute the relative effects of the remaining sources. The following sections will be dedicated to an exhaustive discussion on the efficiencies.

3.4.1 Acceptance, reconstruction and stripping efficiency

The simulated sample is a so-called filtered MonteCarlo and, therefore, it is not possible to extract neither the acceptance and reconstruction nor the stripping efficiencies through simple counting steps at various stages of the simulation.

To account for possible asymmetries between the signal and the normalization modes, caused by geometrical and pre-selection effects, it is necessary to have access to the production logfiles through the LHCb MonteCarlo production software.

However, due to technical problems, this information was not available at the time of writing this thesis and therefore it was estimated using non-filtered MonteCarlo samples simulating the decay $B_u \rightarrow p\pi\pi\Sigma_c(2455)$ and $B_u \rightarrow p\pi\pi\Sigma_c(2520)$, under practically the same conditions as the ones presented so far.

The relative efficiencies obtained are reported in Table 3.15.

	2011	2012
$\epsilon_{accept+reco+stripping}$	0.83 ± 0.02	0.86 ± 0.02

Table 3.15: Efficiency relative to acceptance, reconstruction and stripping selection for 2011 and 2012.

We believe that these efficiencies will not change appreciably once the technical problems are overcome and they are computed on the same samples on which all the other efficiencies have been evaluated.

3.4.2 Selection efficiencies

All the selection criteria applied post-stripping are in principle reproduced by the simulation. Therefore their calculation is conceptually very simple.

In Tables 3.16 and 3.17, the absolute and relative efficiencies taken from MonteCarlo are reported for both the signal and the normalization channels. All the absolute values are computed with respect to the initial sample of true events, for both 2011 and 2012. No differences were seen as a function of the magnet polarity and therefore MagUp and MagDown data have been combined for each year.

The efficiencies in Tables 3.16 and 3.17 do not include L0 trigger and PID, which need to be treated separately, since it is known that the MonteCarlo does not reproduce exactly these conditions and therefore a data-driven procedure needs to be employed.

Selection	2011		
	$\Sigma_c(2455)$	$\Sigma_c(2520)$	ϵ_{rel}
Stripping+association	1.	1.	1.
BDT	0.99 ± 0.01	0.99 ± 0.01	1.00 ± 0.01
Mass cuts+DTF χ^2	0.91 ± 0.01	0.91 ± 0.01	1.00 ± 0.01
L1	0.512 ± 0.009	0.463 ± 0.007	1.11 ± 0.03
L2	0.388 ± 0.007	0.344 ± 0.006	1.13 ± 0.03

Table 3.16: Relative selection efficiencies in 2011 sample.

Selection	2012		
	$\Sigma_c(2455)$	$\Sigma_c(2520)$	ϵ_{rel}
Stripping+association	1.	1.	1.
BDT	0.99 ± 0.01	0.988 ± 0.009	1.00 ± 0.01
Mass cuts+DTF χ^2	0.91 ± 0.01	0.903 ± 0.008	1.00 ± 0.01
L1	0.483 ± 0.006	0.444 ± 0.005	1.09 ± 0.02
L2	0.398 ± 0.006	0.346 ± 0.004	1.15 ± 0.02

Table 3.17: Relative selection efficiencies in 2012 sample.

3.4.2.1 L0 trigger efficiencies

Of the three stages of trigger, the L0 efficiency is the one that needs to be tested accurately, being the most influential either because the L0-step is directly responsible for the recording of the events and the choice of a single L0 line constitutes the selection with strongest effects on signal candidates.

Since the MonteCarlo absolute trigger efficiencies are not completely reliable, a data-driven procedure is required in order to estimate this relative efficiency.

In Table 3.18, the L0 efficiency computed as any other selection efficiency through MonteCarlo samples is reported for the signal and the normalisation channels for both 2011 and 2012.

Sample	$\Sigma_c(2455)^{++}$	$\Sigma_c(2520)^{++}$	ϵ_{rel}^{L0}
2011	0.69 ± 0.02	0.69 ± 0.02	1.00 ± 0.04
2012	0.68 ± 0.01	0.66 ± 0.01	1.03 ± 0.02

Table 3.18: L0 trigger efficiencies extracted from MonteCarlo.

Within the LHCb collaboration, the procedure applied to account for numerical differences between efficiencies computed on MonteCarlo or data is called "TISTOS method" [24]. It is worth reminding that a trigger condition TOS (Trigger On Signal) means that

Sample	$\Sigma_c(2455)^{++}$	$\Sigma_c(2520)^{++}$	ϵ_{rel}^{L0}
2011	0.58 ± 0.13	0.40 ± 0.20	1.45 ± 0.79
2012	0.46 ± 0.07	0.38 ± 0.13	1.21 ± 0.45

Table 3.19: L0 trigger efficiencies extracted through the TISTOS method applied on data.

the presence of the signal is sufficient to generate a positive trigger decision, while TIS (Triggered Independent of Signal) events are those where the part of the event remaining after removing the particles associated with the signal and hits belonging to them, is sufficient to generate a positive trigger decision.

Since TIS requirements are defined not to be dependent from the signal, it is possible to extract the trigger efficiency from data by factorising the number of signal events triggered in a TIS configuration with the number of signal events triggered by the coincidence of that specific TIS configuration and the TOS of interest.

The lines chosen in this case were the *L0HadronDecision TIS* and *L0MuonDecision TIS* which however contain only a very limited number of events. The fitting procedure leading to an estimate for the number of signal events ($\Sigma_c(2455)$ and $\Sigma_c(2520)$) was repeated on the $\Lambda\pi$ mass spectrum resulting from application of the above selection and on that obtained requiring *L0HadronDecision TOS* in addition.

The relative efficiencies obtained applying such method to data selected events are those reported in Table 3.19.

Even though the absolute efficiencies are not in good agreement, relative efficiencies are compatible within errors.

The large errors reported in Table 3.19 are purely statistical and come from the fit procedure applied to obtain the signal yields for the signal and the normalisation channels, which have a limited number of events.

3.4.2.2 PID efficiencies

PID efficiencies ϵ_{rel}^{PID} have been computed through the PIDCalib package (see 2.4.2).

The signal samples used to perform the weighting have been obtained by selecting true signal MonteCarlo events with the same requirements imposed on data.

MagUp 2011	MagDown 2011	MagUp 2012	MagDown 2012
1.002 ± 0.005	1.002 ± 0.003	1.0078 ± 0.0005	1.0072 ± 0.0007

Table 3.20: PID relative efficiencies for the different subsamples.

Three different dedicated binning schemes on pseudorapidity η and transverse momentum P_T of the the protons have been chosen to extract efficiencies through PIDCalib, making sure that a sufficient number of events populates each bin.

The values reported in Table 3.20 are computed as the mean value of the results obtained with the three different schemes and the errors are estimated using the largest among the statistical errors obtained in each case, and depend on the calibration and weighting samples' size.

3.5 Systematic uncertainties

The major sources of systematic uncertainties are expected to be related to:

- L0 trigger efficiency calculation
- Particle Identification
- model used in the decay of the Λ_c .

In the following paragraphs each of them will be addressed in details.

3.5.1 L0 trigger

The relative L0 trigger efficiency ϵ_{rel}^{trigg} has been calculated through the TISTOS method applied to the data, as discussed in Section 3.4.2.1.

The systematic error associated to this method was computed from a comparison between the result from a direct estimate of L0 trigger efficiency using the MonteCarlo (Table 3.18) and that obtained applying the TISTOS method to the MonteCarlo samples, reported in Table 3.21. This is acceptable since we are interested only in relative efficiencies, otherwise this were not the case, trigger efficiencies and the determination of their systematic errors would have required a more involved treatment.

For convenience the value of values of Table 3.18 are shown also in the first columns of Table 3.22, where also the differences between the mean values are given.

The comparison yield the value of ± 0.01 for the systematic error associated to the L0 trigger efficiency, completely negligible when compared with the statistical error.

Sample	$\Sigma_c(2520)^{++}$	$\Sigma_c(2455)^{++}$	ϵ_{rel}^{L0}
2011	0.52 ± 0.02	0.52 ± 0.01	1.00 ± 0.04
2012	0.46 ± 0.01	0.48 ± 0.02	1.04 ± 0.05

Table 3.21: Trigger efficiencies extracted through the TISTOS method.

Therefore, no systematic uncertainty has been associated to L0 trigger selection.

3.5.2 PID

Systematic errors on PID efficiencies originated from the dependence of the results on the choice about the particular binning used for their calculation through the PIDCalib package.

Sample	L0-MC	L0-TISTOS on MC	Δ mean values
2011	1.00 ± 0.04	1.00 ± 0.04	0.
2012	1.03 ± 0.02	1.04 ± 0.05	0.01

Table 3.22: L0 trigger systematic uncertainties.

Binning scheme	2011		2012	
	Up	Down	Up	Down
A	1.0125 ± 0.0001	1.0118 ± 0.0001	1.0092 ± 0.0002	1.0086 ± 0.0001
B	1.0138 ± 0.0002	1.0134 ± 0.0002	1.0113 ± 0.0002	1.0105 ± 0.0002
C	0.980 ± 0.005	0.981 ± 0.003	1.0028 ± 0.0005	1.0026 ± 0.0007

Table 3.23: PID relative efficiencies obtained with three different binning schemes.

The usage of different binning schemes allows to estimate this systematic error. surely helps in reaching the aim to take into account any systematic effect related to this choice.

As mentioned in Section 3.4.2.2, three binning schemes (named A,B, and C) have been adopted within PIDCalib for this analysis. The results obtained are reported in Table 3.23, separately for year and polarity.

A reasonable estimation for the systematic associated to PID variables is assumed to be the maximum absolute variation of the central values obtained with the different schemes.

This procedure for the 2011 and 2012 data yields the results shown in Table 3.24.

From a comparison between these systematic errors and the statistical ones, it is clear that the former are $\mathcal{O}(10 - 100)$ larger than the latter and therefore one can conclude that PID efficiencies are systematic errors dominated.

3.5.3 Decay model

In order to estimate the effect of the decay model used of the Λ_c , it was decided to artificially vary the relative fractions of the decay channels of the Λ_c that have the same final state $pK\pi$. In fact, although the Λ_c is forced to decay in a $pK\pi$ final state, this process can also happen via resonant channels, as explained in Section 3.2.1, in the ratios shown in Table 3.2.

2011		2012	
MagUp	MagDown	MagUp	MagDown
0.03	0.03	0.009	0.008

Table 3.24: Relative systematic uncertainties related to PID.

Specifically, the global selection efficiencies were re-computed in three different configurations, by varying the ratio between the non resonant channel, in which the three final state particles are distributed according to three-body phase space, and the remaining decays, as follows:

- "Real", where the ratio between the events decaying into the different channels was not modified
- "Modified I", where the non-resonant fraction was enhanced by the 50% with respect to the simulated ratio
- "Modified II", where the non-resonant fraction was reduced by the 50% with respect to the simulated ratio

The relative efficiencies for the initial and modified configurations are shown in Table 3.25.

Configuration	2011	2012
Real	1.13 ± 0.03	1.17 ± 0.03
Modified I	1.11 ± 0.06	1.17 ± 0.05
Modified II	1.13 ± 0.06	1.19 ± 0.05

Table 3.25: Relative efficiencies computed varying the relative branching fractions of the channels through which the Λ_c is forced to decay into the final state $pK\pi$.

Since the mean values differ by 0.02 at the most and are consistent with each other within errors, no systematic uncertainty has been associated to the decay model of the Λ_c .

We understand that another systematic error can be introduced by the decay model assumed for the Σ_c , but this is more difficult to calculate at this stage, since it would require the generation of a MonteCarlo sample not available at this stage.

3.6 Results

The raw branching fraction ratio given in Table 3.14 needs to be corrected for the various efficiency factors computed so far.

Table 3.26 summarises the effects of the various corrections applied in sequence.

The two results are in agreement within the errors, which are large due mainly to the fitting results and the L0 trigger efficiencies.

With the estimated systematic uncertainty estimated coming uniquely from PID-related requirements, the final results are

$$\frac{\mathcal{B}(B_u \rightarrow p\pi^+\pi^+\bar{\Sigma}_c(2520)^{--})}{\mathcal{B}(B_u \rightarrow p\pi^+\pi^+\bar{\Sigma}_c(2455)^{--})} = 0.90 \pm 0.21(stat) \pm 0.49(L0 - stat) \pm 0.03(syst)$$

Correction	2011	2012
None	0.66 ± 0.15	0.65 ± 0.11
Acceptance+reconstruction+stripping	0.55 ± 0.13	0.56 ± 0.09
+Selection	0.62 ± 0.15	0.64 ± 0.10
+PID	0.62 ± 0.15	0.64 ± 0.10
+Trigger	0.90 ± 0.53	0.77 ± 0.31

Table 3.26: Relative branching fraction for the 2011 and 2012 samples after the various corrections have been applied. The errors are purely statistical.

for 2011 data and

$$\frac{\mathcal{B}(B_u \rightarrow p\pi^+\pi^+\bar{\Sigma}_c(2520)^{--})}{\mathcal{B}(B_u \rightarrow p\pi^+\pi^+\bar{\Sigma}_c(2455)^{--})} = 0.77 \pm 0.12(stat) \pm 0.29(L0 - stat) \pm 0.007(syst)$$

for 2012, where $L0-stat$ indicates the statistical error introduced by the estimation of the L0 trigger efficiency. This error could be however significantly reduced extending the method of calculation to larger samples.

The weighted average of the results shown is

$$\frac{\mathcal{B}(B_u \rightarrow p\pi^+\pi^+\bar{\Sigma}_c(2520)^{--})}{\mathcal{B}(B_u \rightarrow p\pi^+\pi^+\bar{\Sigma}_c(2455)^{--})} = 0.80 \pm 0.11(stat) \pm 0.25(L0 - stat) \pm 0.03(syst)$$

Assuming for the branching fraction of the decay $B_u \rightarrow p\pi^+\pi^+\bar{\Sigma}_c(2455)^{--}$ the measured value of $(2.34 \pm 0.20) \cdot 10^{-4}$ quoted in [1] and resulting from the average between measurements performed by the CLEO and BaBar collaborations, the branching fraction of the $B_u \rightarrow p\pi^+\pi^+\bar{\Sigma}_c(2520)^{--}$ decay measured is

$$\mathcal{B}(B_u \rightarrow p\pi^+\pi^+\bar{\Sigma}_c(2520)^{--}) = (1.87 \pm 0.61(stat) \pm 0.17(syst)) \cdot 10^{-4}$$

The final systematic uncertainty is the sum in quadrature of the relative uncertainty PID-related and the one due to the value used for the branching fraction of the normalisation mode, which is the largest of the two.

3.7 Conclusions

The first observation of the decay $B_u \rightarrow p\pi^+\pi^+\bar{\Sigma}_c(2520)^{--}$ is reported using data collected by the LHCb detector during 2011 and 2012, corresponding to a total integrated luminosity of 3 fb^{-1} and a first measurement of its branching fraction relatively to the $B_u \rightarrow p\pi^+\pi^+\bar{\Sigma}_c(2455)^{--}$ decay was performed in this thesis.

LHCb VARIABLES DEFINITION

- χ^2 NDOF: χ^2 per number of degrees of freedom. In LHCb tracks are reconstructed through a fit procedure of the relative hits in the tracking system. The goodness of this fit is quantified through this variable. A track fitted using random hits has a $\chi^2 NDOF > 5$.
- χ^2 VNDOF: χ^2 of the vertex per number of degrees of freedom. It is referred to the goodness of the fit result on the decay vertex. This fit is performed using tracks of particles which define the vertex. A real vertex is characterized by a χ^2 VNDOF of about 1.
- DOCAMAX: maximum distance of closest approach. It represents the maximum value among those obtained by measuring the closest approach distance between all possible couples of tracks in the decay of interest.
- IP χ^2 : impact parameter χ^2 . The distance between the primary vertex and a particle track (eventually extrapolated) is defined as impact parameter. The impact parameter χ^2 is defined as the difference between the χ^2 of the fit to the primary vertex with and without the track which the variable is referred. The IP χ^2 of a track coming from a secondary vertex is expected to assume high values.
- FD χ^2 : flight distance χ^2 . The flight distance of a particle is defined as the distance between its primary and its decay vertices. Requiring an high IP χ^2 selects particles which preferably are not produced at the primary vertex.
- DIRA χ^2 : the direction angle χ^2 is the χ^2 of the cosine of the angle between the momentum vector of the particle of interest and the direction defined by joining some reference vertex to the end-vertex of the particle.

- P_T : transverse momentum is the projection of the momentum on the beam direction.
- *track ghost probability*: a track is classified as ghost track as long as it has less than 70% of hits matching the hits of any final state MonteCarlo particle. This variable is defined as the probability that the track is a ghost track.

BOOSTED DECISION TREE

As mentioned, in order to avoid any bias in the measurement of the $\mathcal{B}(\Lambda_c \rightarrow pK\pi)$, it was necessary not to introduce any selection which could have different efficiencies for PartReco and FullReco samples.

For this reason, a check to ensure that the distributions relative to variables used in the BDT showed no differences in the two lines was performed.

A comparison between these distributions for PartReco and FullReco events for all these variables is shown in the following figures.

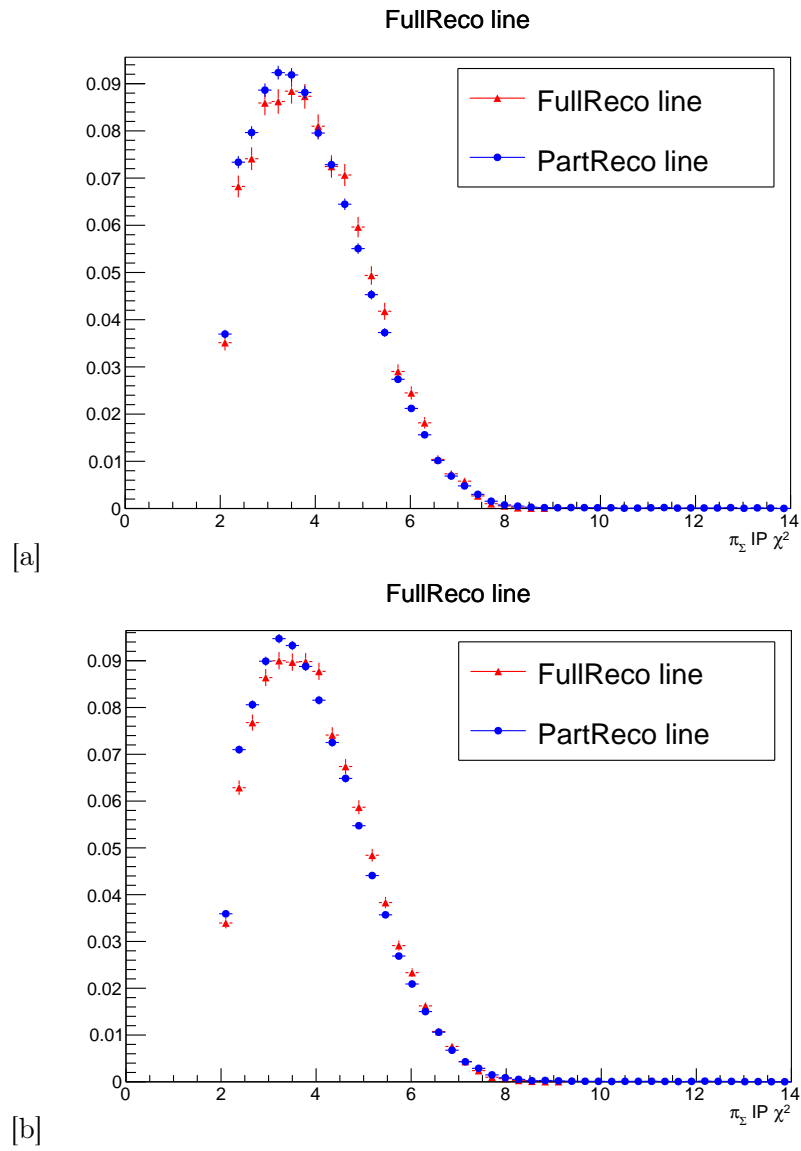


Figure B.1: $\log(\pi_\Sigma \text{ impact parameter } \chi^2)$ distribution for PartReco and FulReco samples in 2011 [a] and 2012 [b].

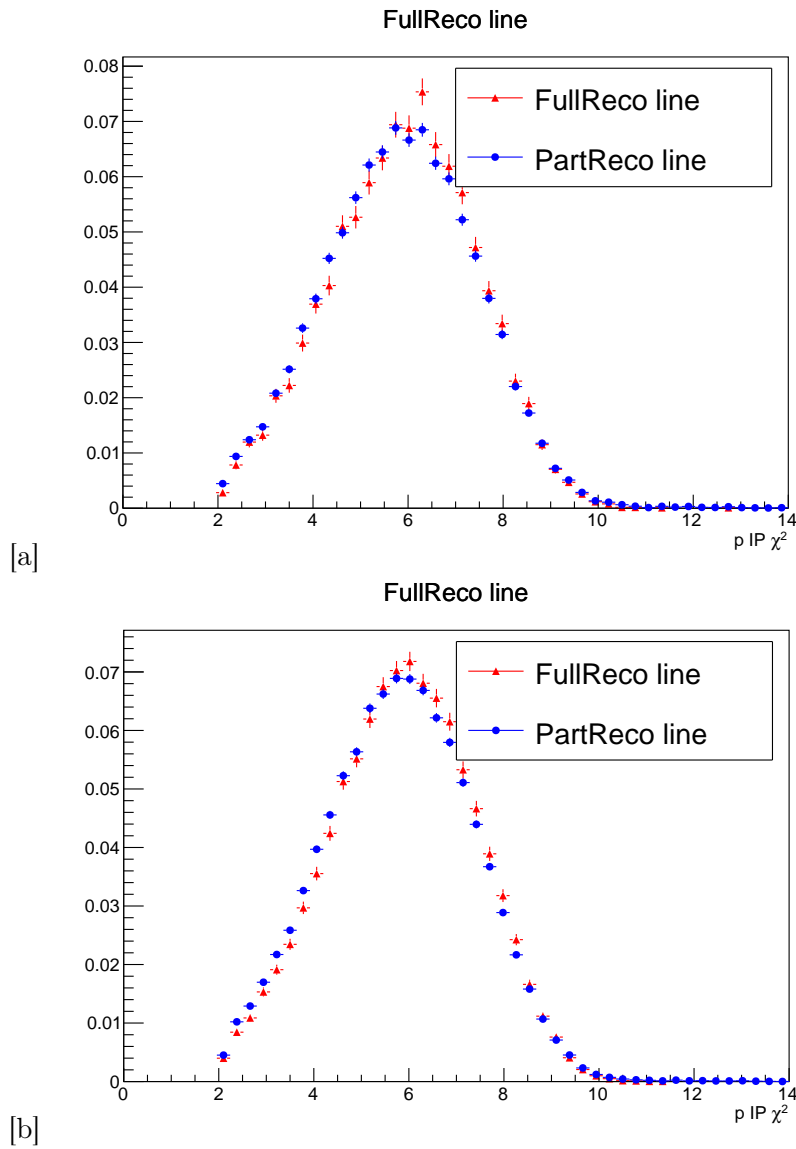


Figure B.2: $\log(p$ impact parameter $\chi^2)$ distribution for PartReco and FulReco samples in 2011 [a] and 2012 [b].

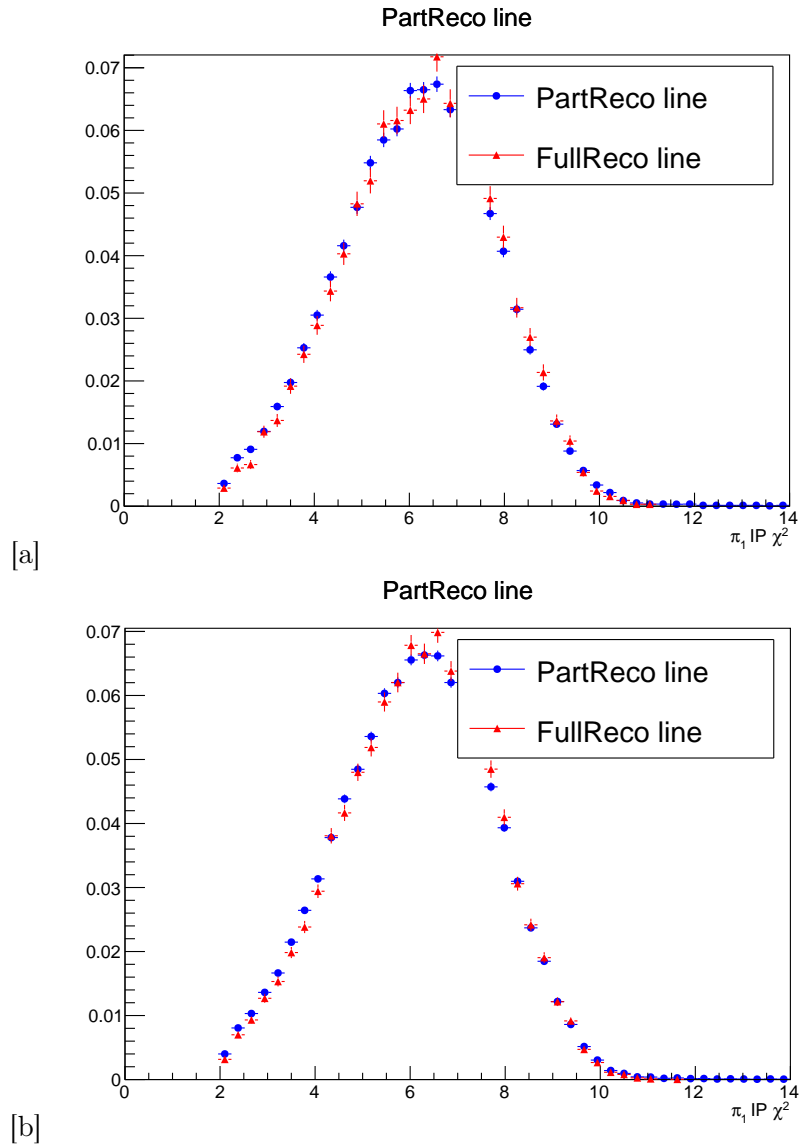


Figure B.3: $\log(\pi_1 \text{ impact parameter } \chi^2)$ distribution for PartReco and FulReco samples in 2011 [a] and 2012 [b].

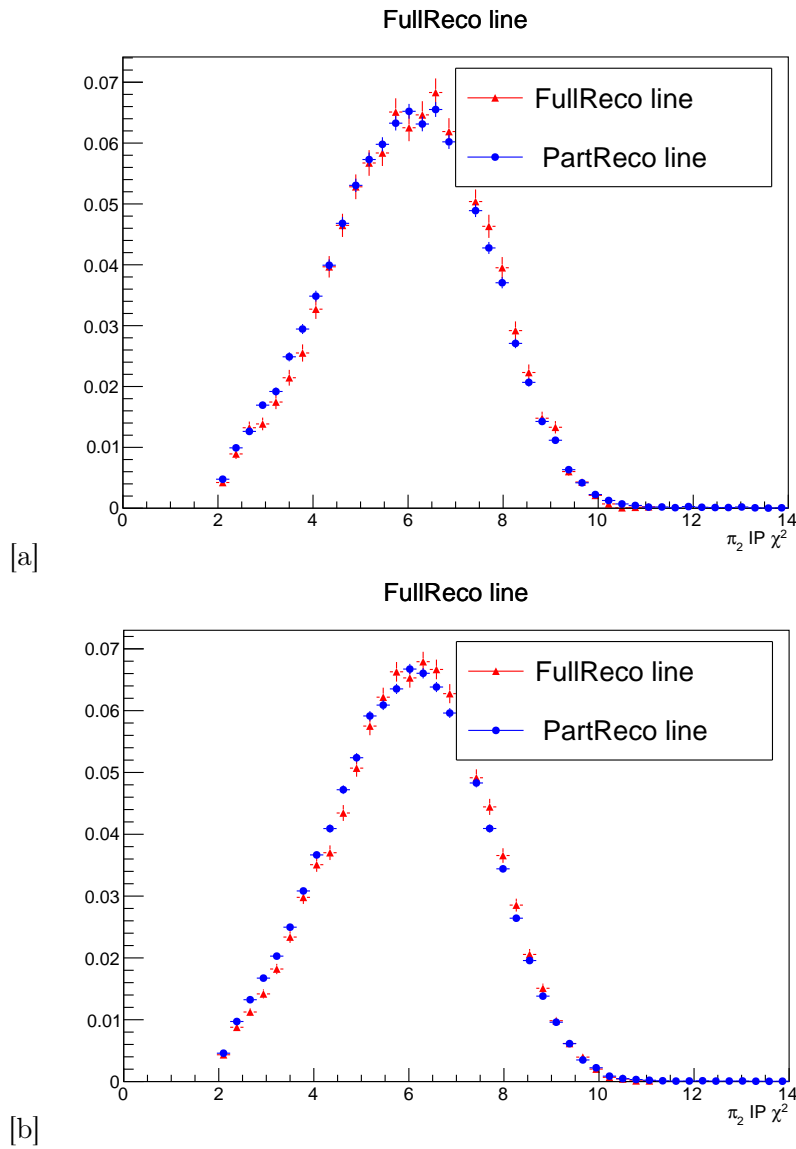


Figure B.4: $\log(\pi_2 \text{ impact parameter } \chi^2)$ distribution for PartReco and FulReco samples in 2011 [a] and 2012 [b].

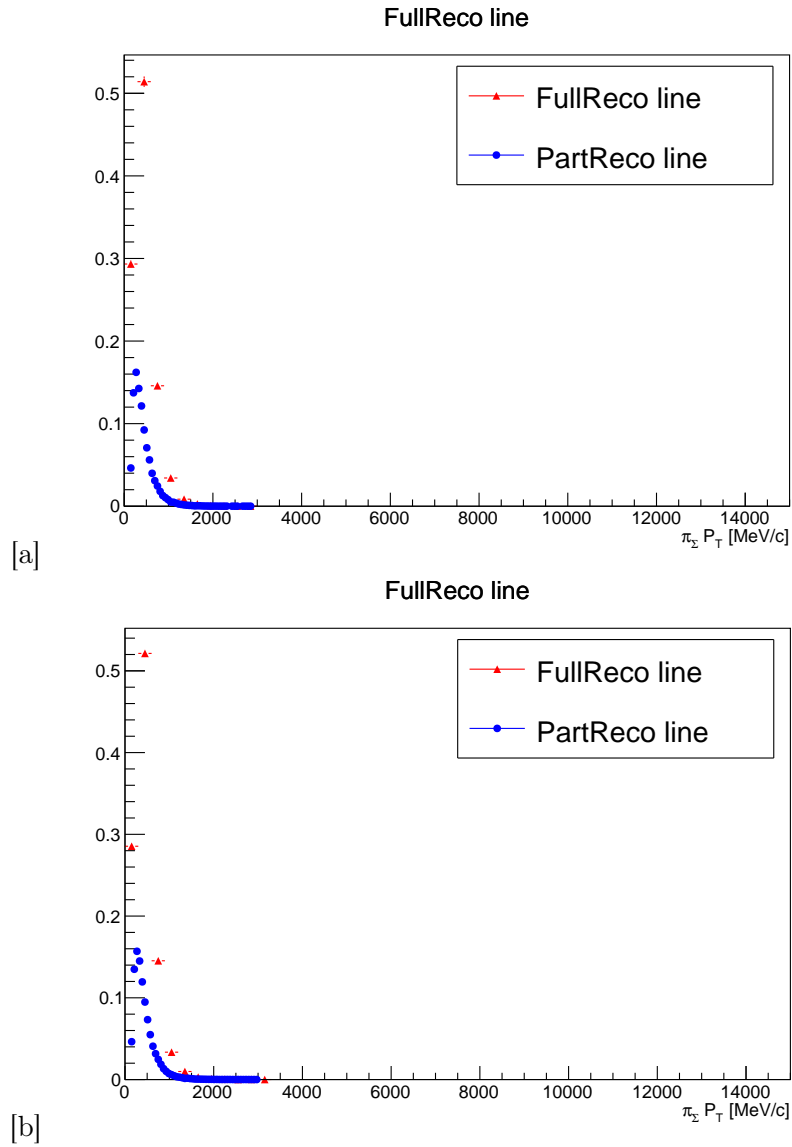


Figure B.5: $\pi_\Sigma P_T$ distribution for PartReco and FulReco samples in 2011 [a] and 2012 [b].

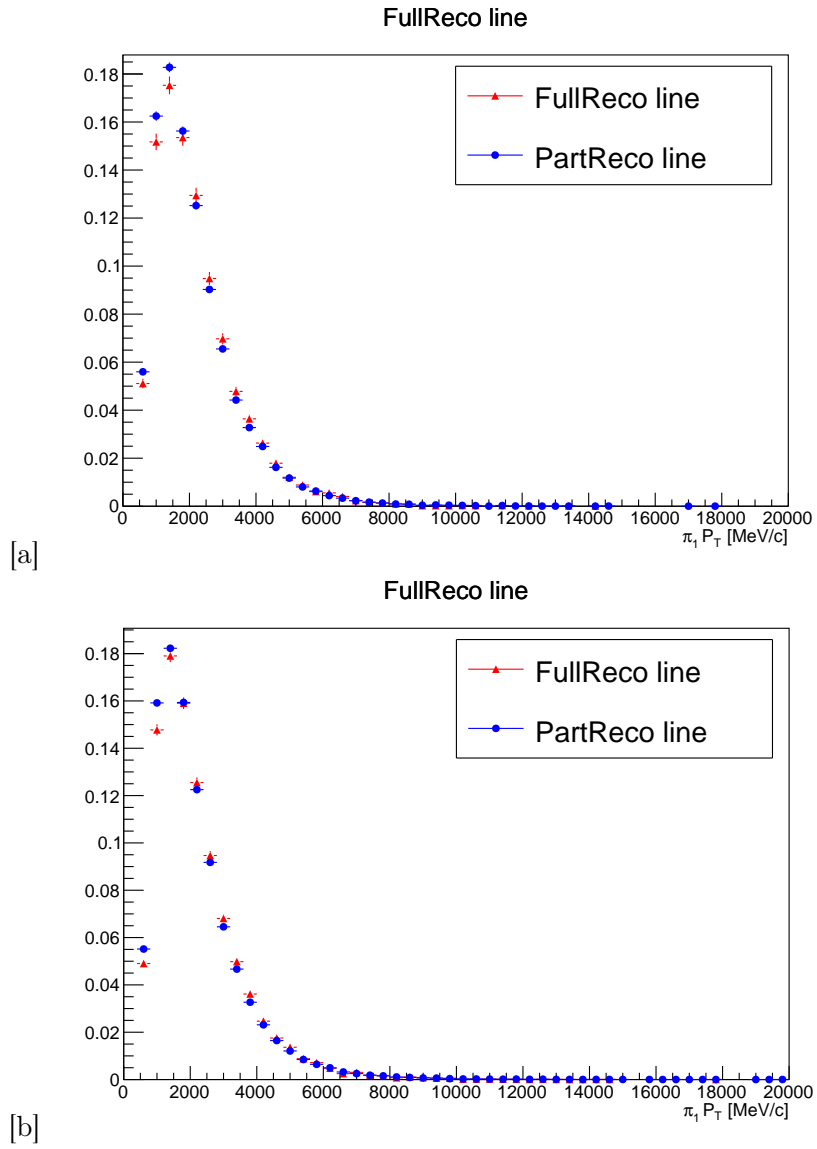


Figure B.6: $\pi_1 P_T$ distribution for PartReco and FulReco samples in 2011 [a] and 2012 [b].

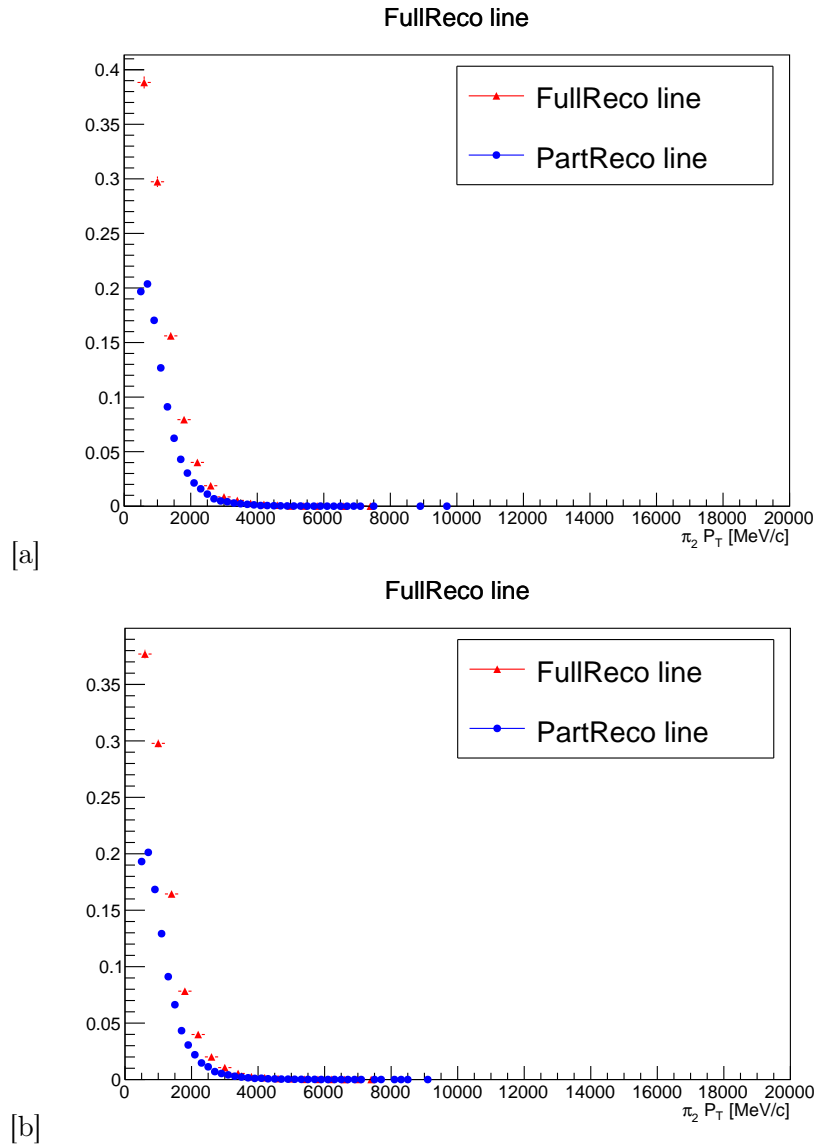


Figure B.7: $\pi_2 P_T$ distribution for PartReco and FulReco samples in 2011 [a] and 2012 [b].

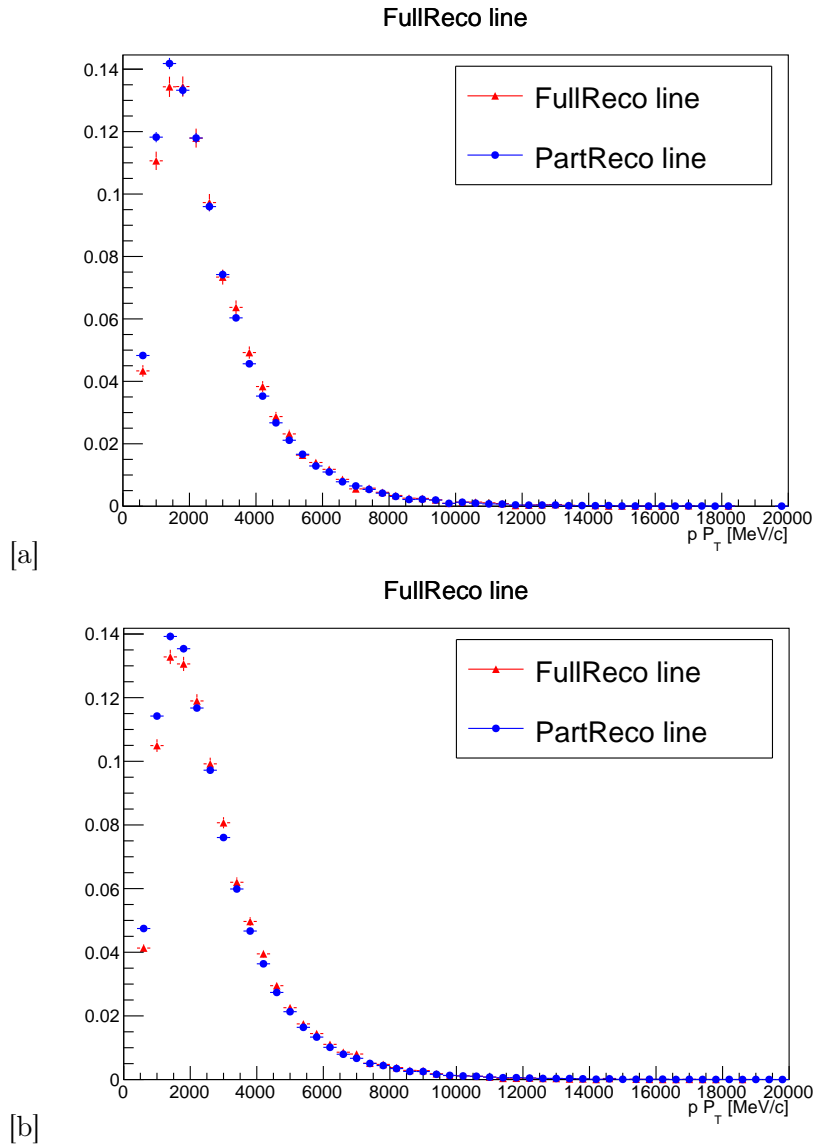


Figure B.8: $p P_T$ distribution for PartReco and FulReco samples in 2011 [a] and 2012 [b].

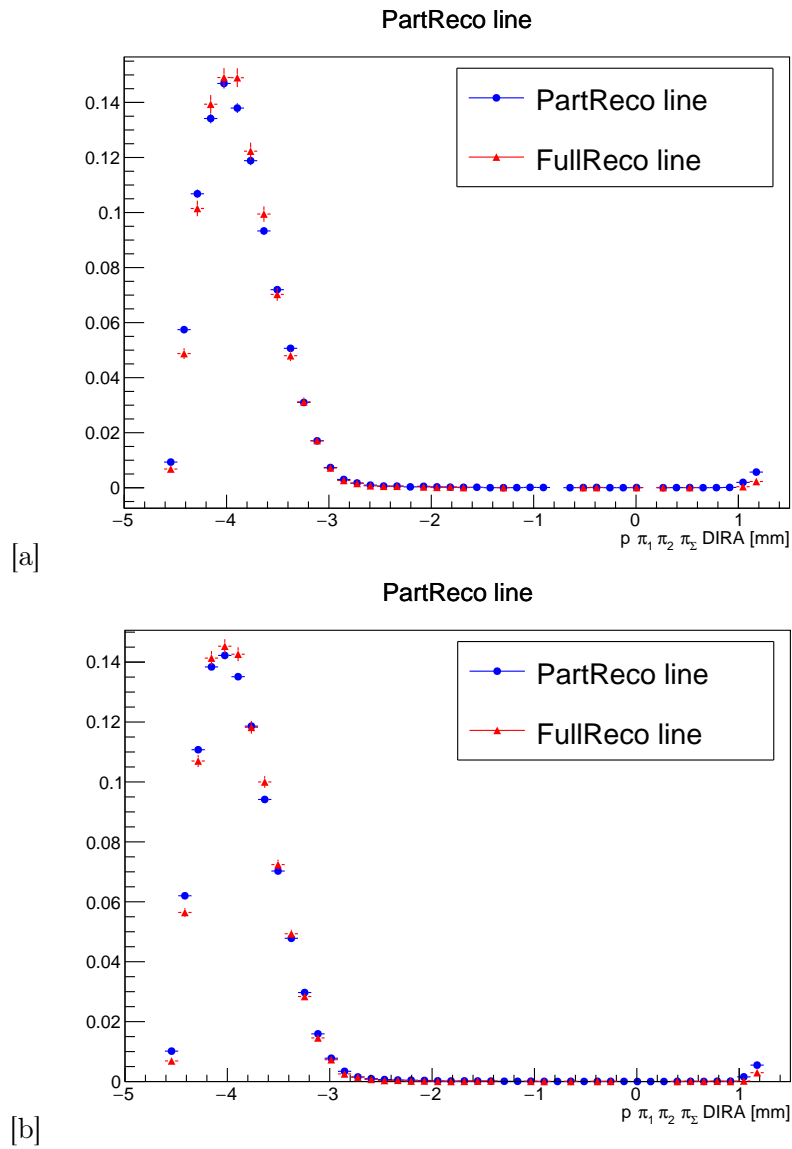


Figure B.9: $\log(0.01 + \text{acos}(p\pi\pi\pi_{\Sigma} \text{DIRA}))$ distribution for PartReco and FulReco samples in 2011 [a] and 2012 [b].

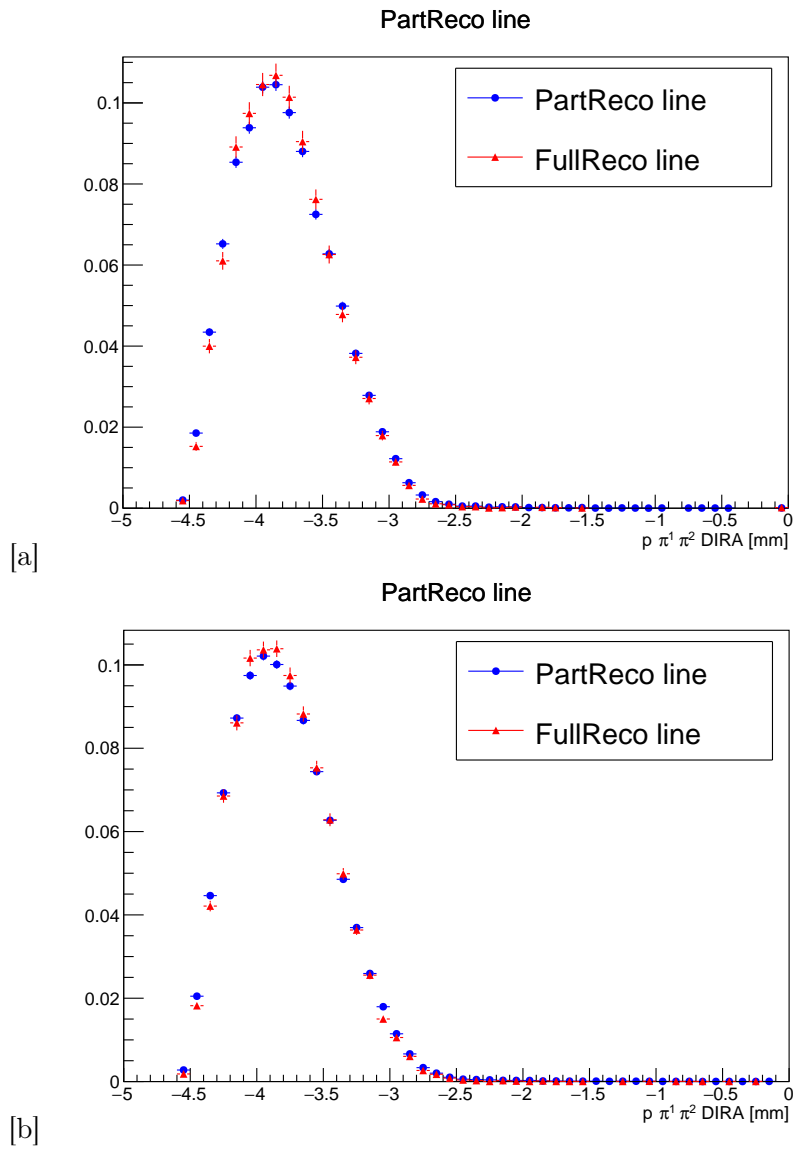


Figure B.10: $\log(0.01+\cos(p\pi\pi \text{ DIRA}))$ distribution for PartReco and FullReco samples in 2011 [a] and 2012 [b].

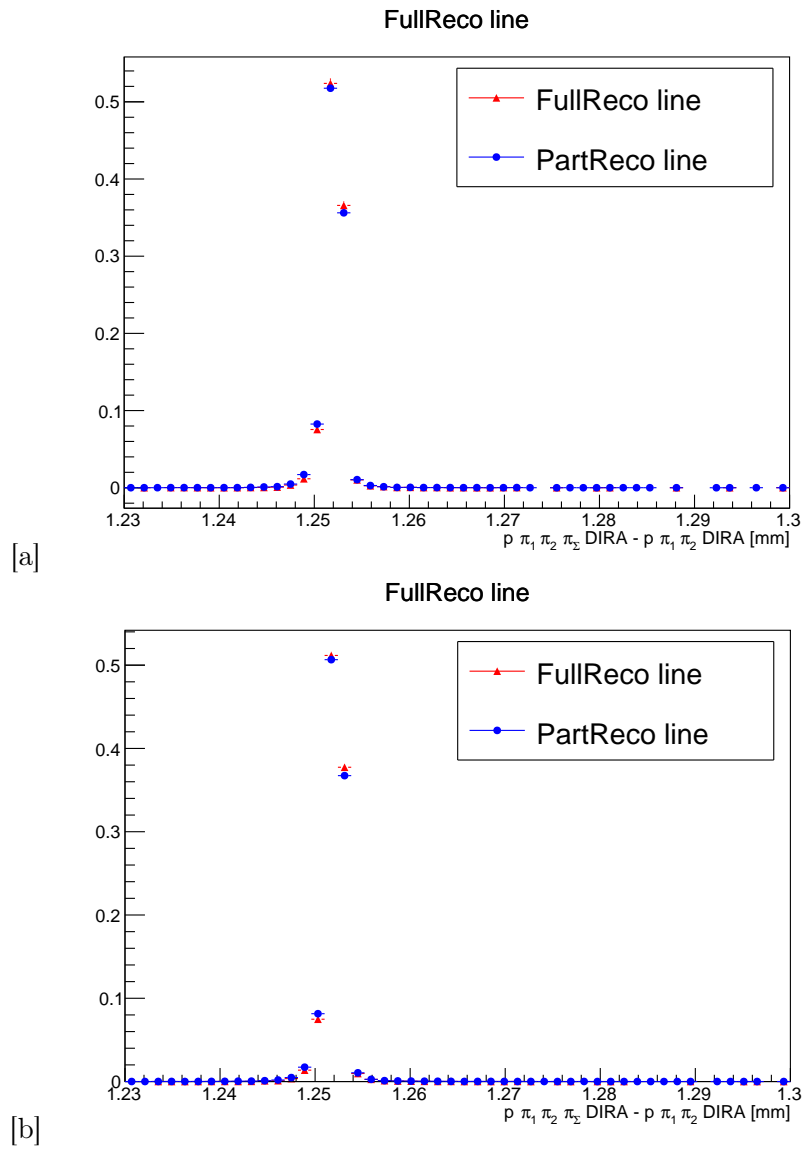


Figure B.11: $\log(3.5 + \text{acos}(p\pi\pi\pi_{\Sigma} \text{ DIRA}) - \text{acos}(p\pi\pi \text{ DIRA}))$ for PartReco and FullReco samples in 2011 [a] and 2012 [b].

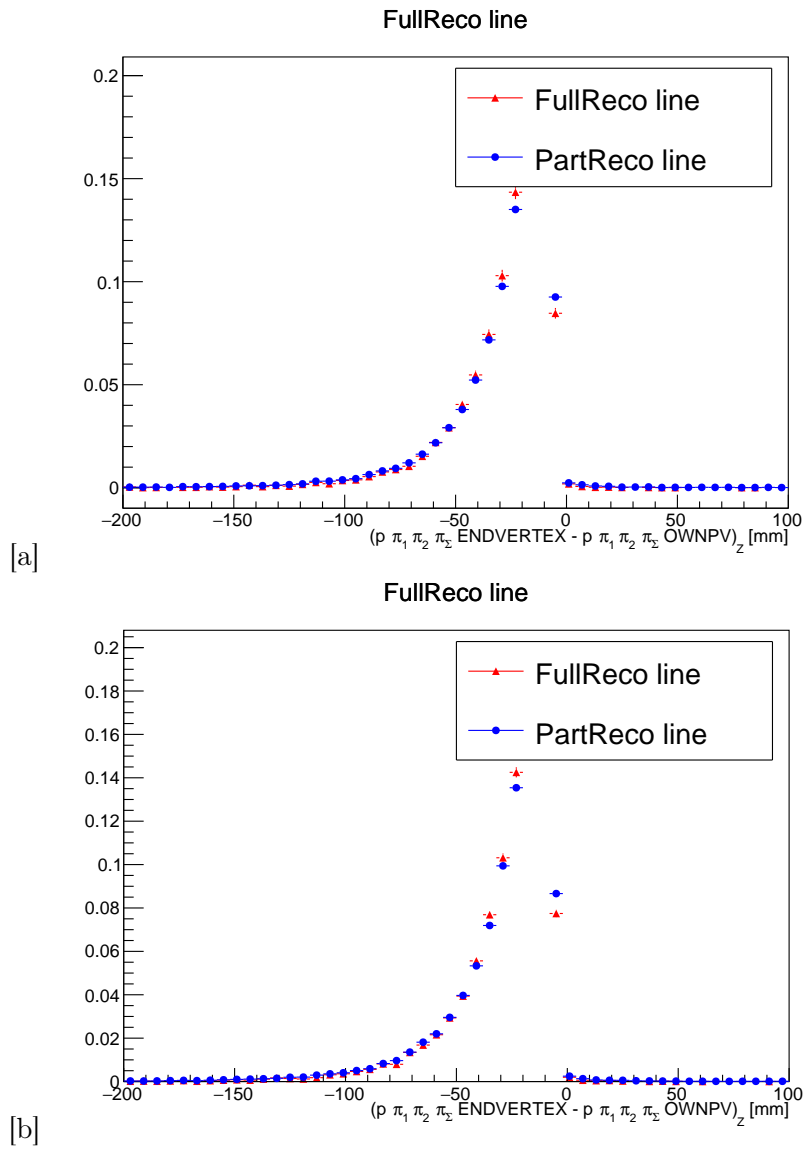


Figure B.12: $p\pi\pi\pi_\Sigma$ distance from primary vertex distribution on z-direction for PartReco and FulReco samples in 2011 [a] and 2012 [b].

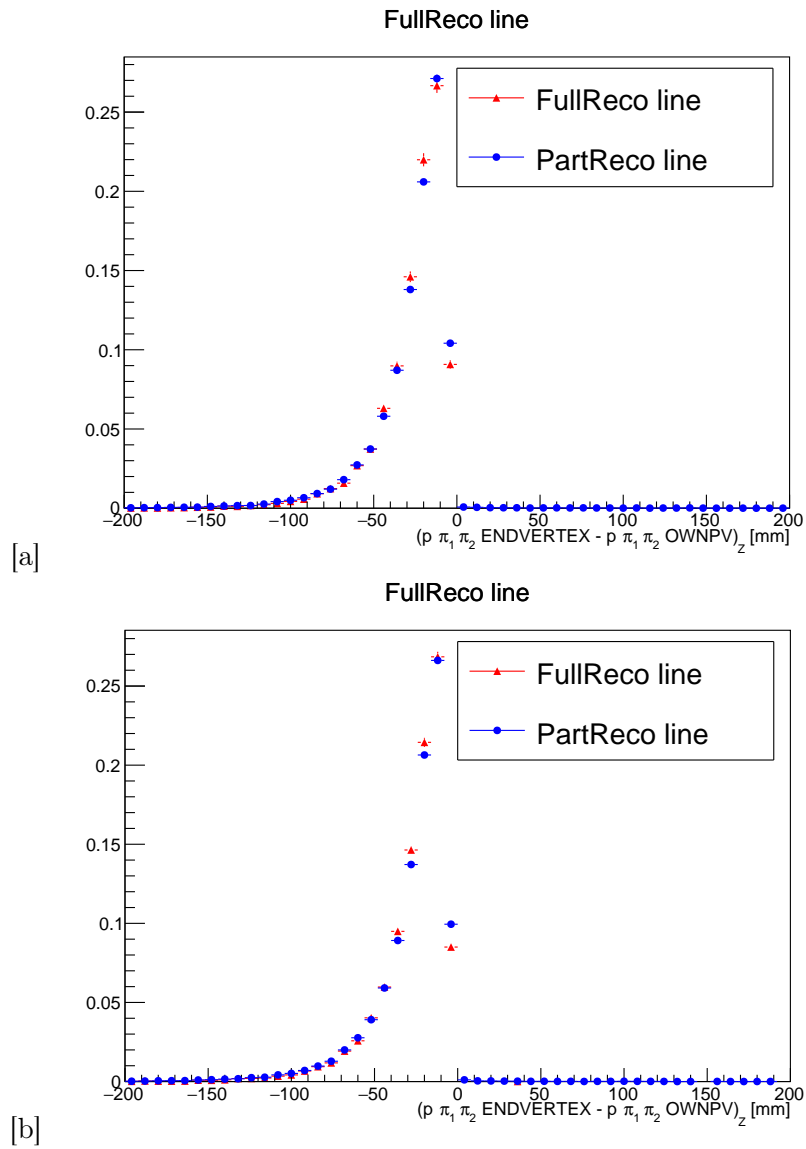


Figure B.13: $p\pi\pi$ distance from primary vertex distribution on z -direction for PartReco and FullReco samples in 2011 [a] and 2012 [b].

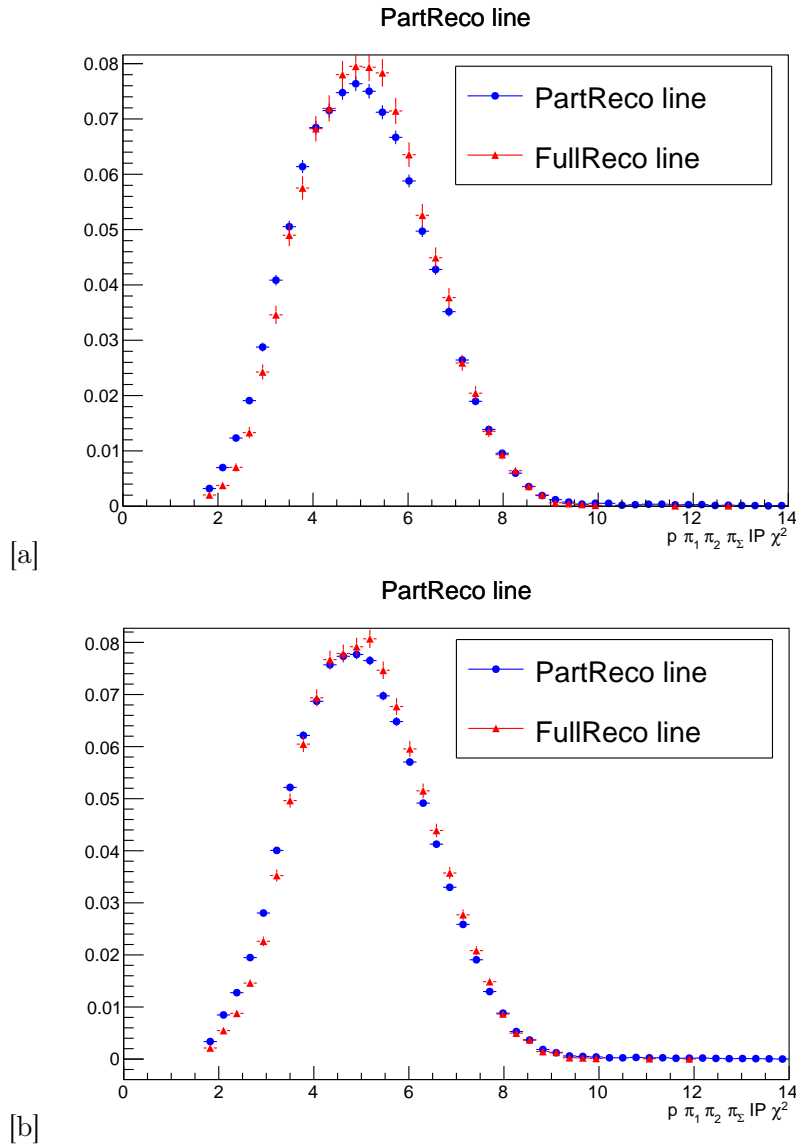


Figure B.14: $\log(p\pi\pi\pi_{\Sigma}$ impact parameter χ^2) distribution for PartReco and FullReco samples in 2011 [a] and 2012 [b].

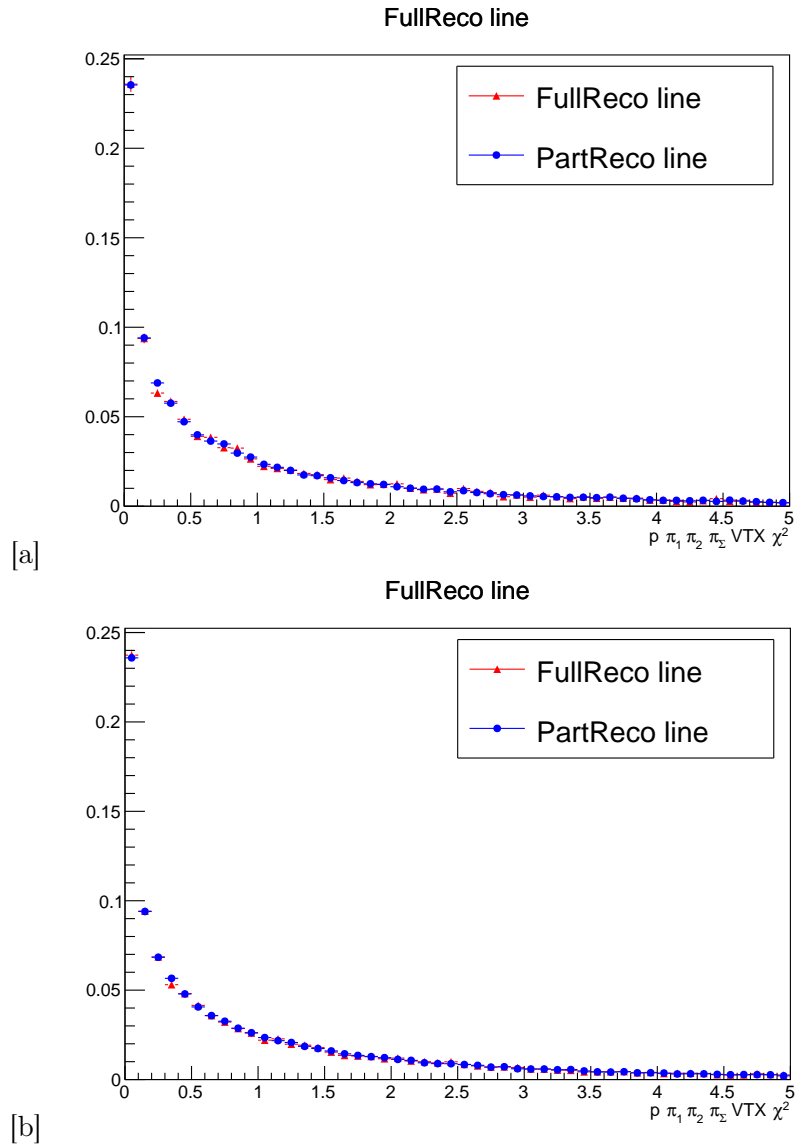


Figure B.15: $p\pi\pi\pi_\Sigma$ vertex χ^2 distribution for PartReco and FulReco samples in 2011 [a] and 2012 [b].

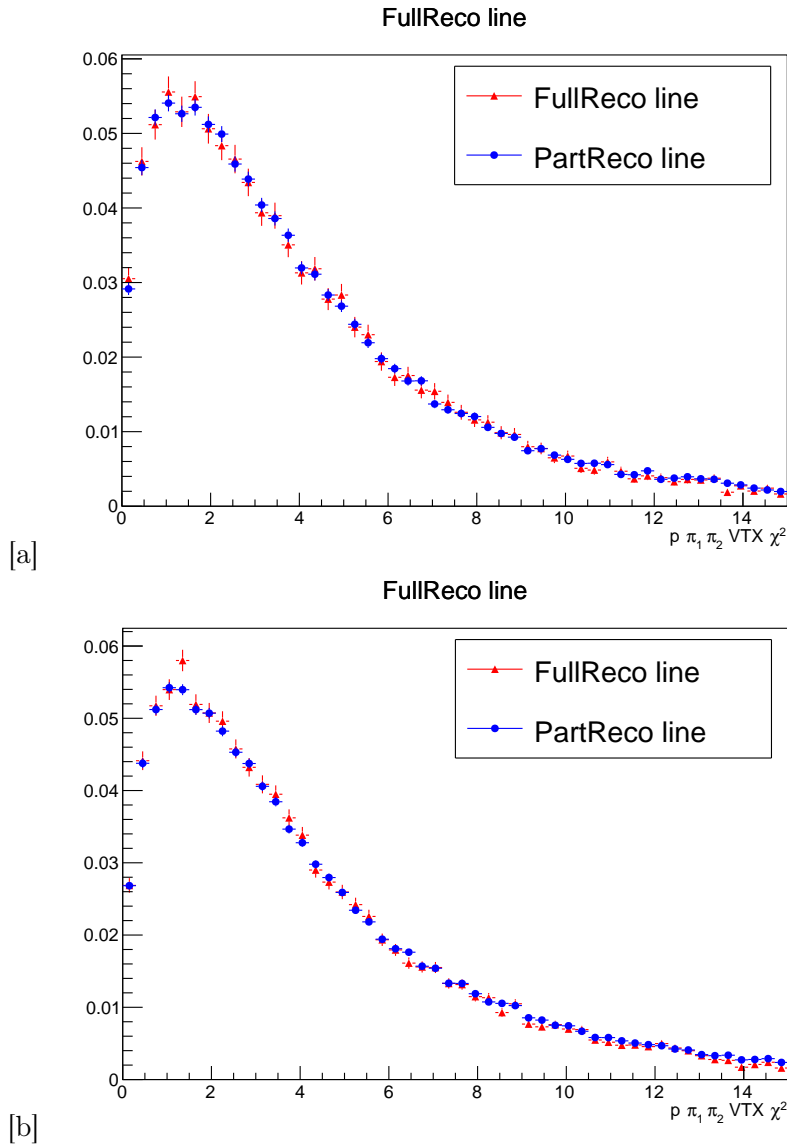


Figure B.16: $p\pi\pi$ vertex χ^2 distribution for PartReco and FulReco samples in 2011 [a] and 2012 [b].

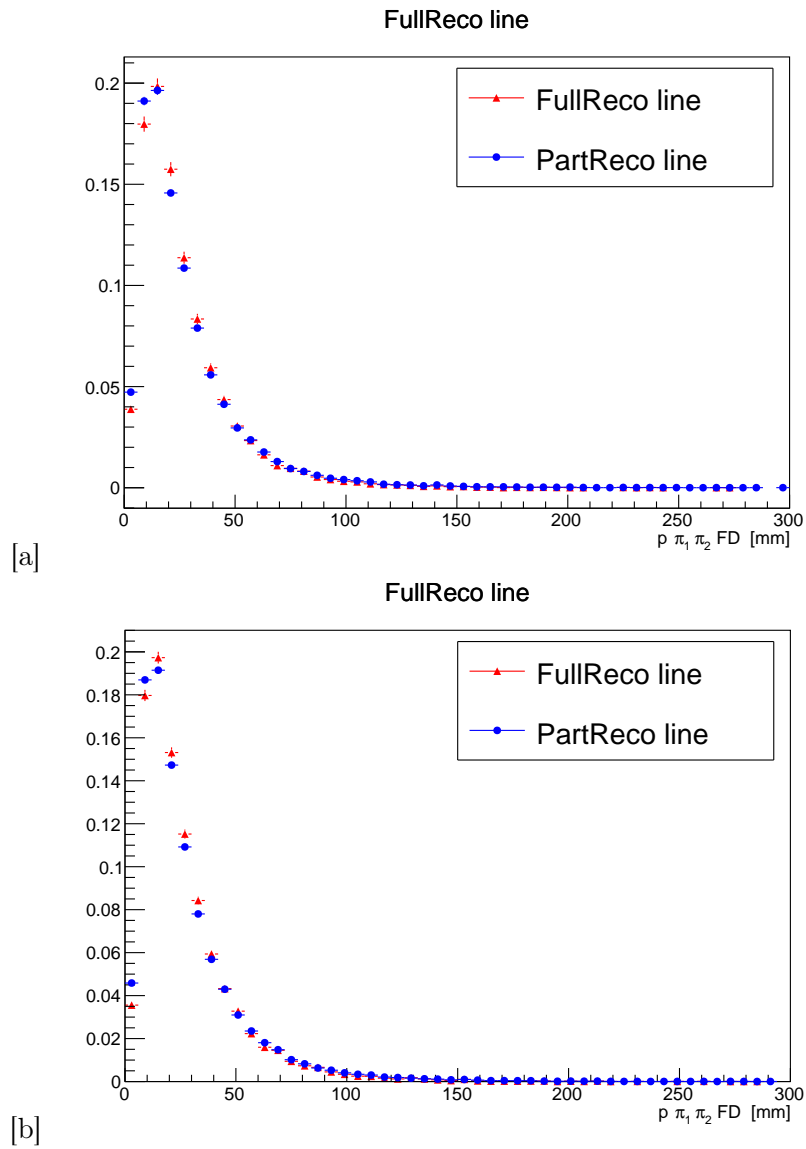


Figure B.17: $p\pi_1\pi_2 \chi^2$ flight distance distribution for PartReco and FulReco samples in 2011 [a] and 2012 [b].

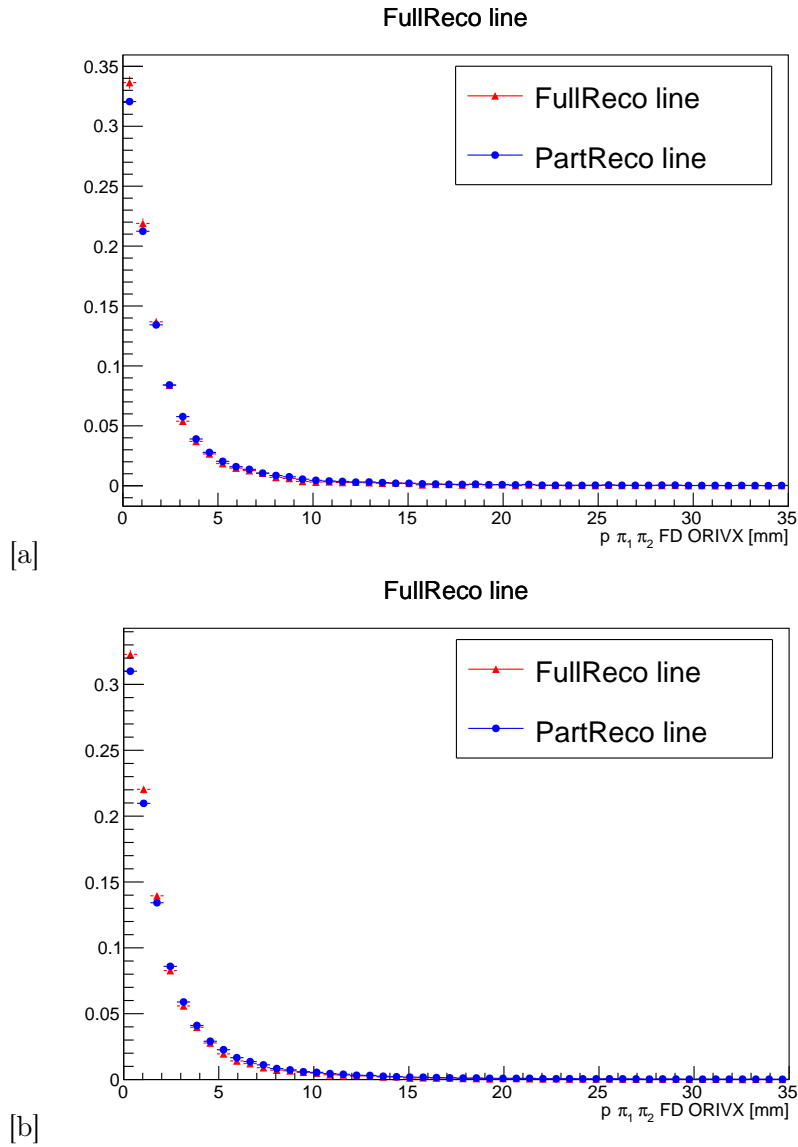


Figure B.18: $p\pi_1\pi_2 \chi^2$ flight distance from primary vertex distribution for PartReco and FullReco samples in 2011 [a] and 2012 [b].

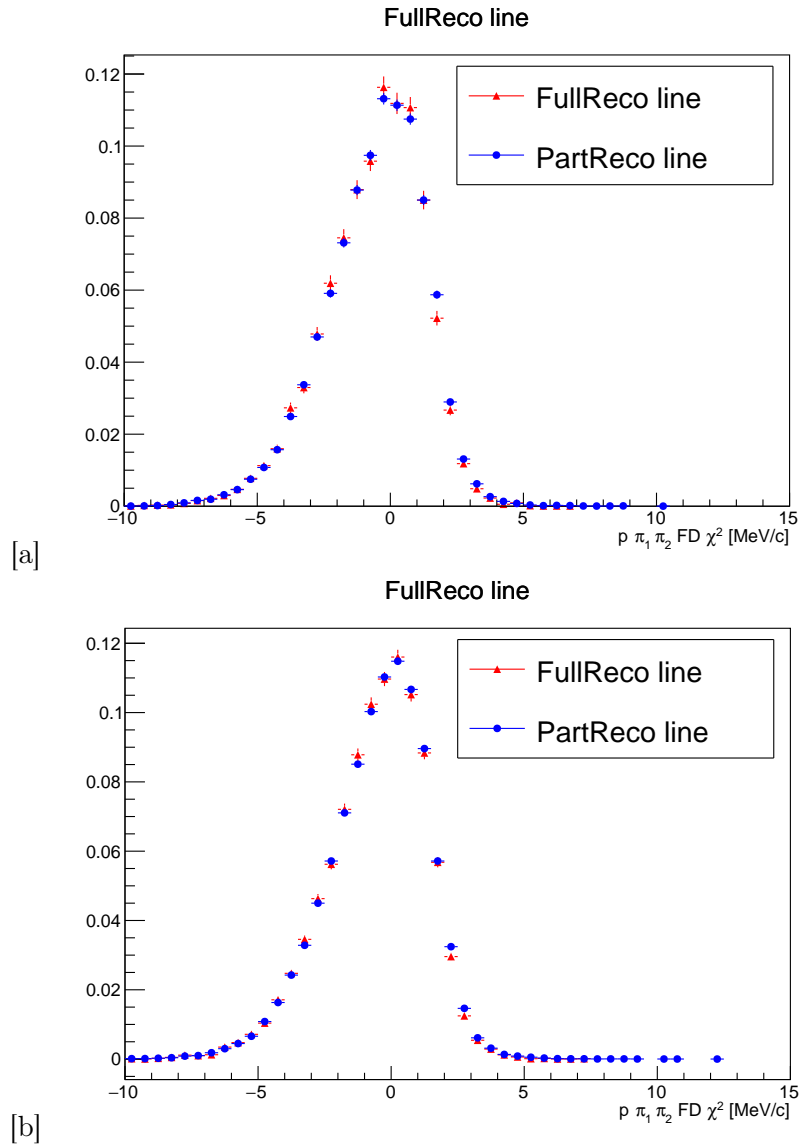


Figure B.19: $\log(p\pi_1\pi_2 \chi^2 \text{ flight distance})$ from primary vertex distribution for PartReco and FullReco samples in 2011 [a] and 2012 [b].

RELATIVISTIC BREIT WIGNER FUNCTION

The relativistic Breit-Wigner function is here reported:

if $x > \alpha$

$$P_{sign(2455)} = \gamma \cdot \frac{2\sqrt{2}}{\pi} \cdot \frac{\alpha \cdot \beta \cdot S \cdot \Gamma}{\sqrt{\alpha^2 + \Gamma} \cdot ((x^2 - \alpha^2)^2 + \alpha^2(\beta \cdot S^2))} \cdot S$$

if $x < \alpha$

$$P_{sign(2455)} = \gamma \cdot \frac{2\sqrt{2}}{\pi} \cdot \frac{\alpha \cdot \beta \cdot \Gamma}{\sqrt{\alpha^2 + \Gamma} \cdot ((x^2 - \alpha^2)^2 + \alpha^2\beta^2)}$$

where

$$\Gamma = \alpha \cdot \sqrt{\alpha^2 + \beta^2 \cdot S^2}$$

α is the mass of the resonance and S is a suppression factor, namely a power of the ratio of the momentum of each decay product (Λ_c, π) in the center of the mass calculated for the mass equal to x over the one calculated at the resonance.

$$S = \frac{\frac{\sqrt{(x^2 - x_{th}^2) \cdot (x^2 - x_o^2)}}{2\alpha}}{\frac{\sqrt{(\alpha^2 - x_{th}^2) \cdot (\alpha^2 - x_o^2)}}{2\alpha}}$$

where

$$x_{th} = m_\Lambda + m_\pi$$

and

$$x_o = m_\Lambda - m_\pi$$

PRELIMINARY STUDY ON THE LOW MASS BACKGROUND REGION

A preliminary study to establish the possible origin of the excess of events on the B_u invariant mass region below $5179 \text{ MeV}/c^2$ was performed.

In Figure D.1, a comparison between the $\Lambda_c^+\pi^+$ invariant mass spectrum in the "flat background" and the "low-background" regions is shown. An excess of events around $2455 \text{ MeV}/c^2$ is visible in the spectrum related to the low mass region. This is less visible in the corresponding plot for the flat background.

The same comparison is made on the $\Lambda_c^+\pi^-$ invariant mass spectrum (Figure D.2), where a clear suppression of the neutral Σ_c is observed in the flat-background region.

As further check, the Λ_c mass spectrum in the signal, flat-background and low-mass background regions is shown in Figure D.3.

Signal	Low mass background	Flat background
0.86	0.68	0.31

Table D.1: S/(S+B) ratio for the Λ_c mass distribution computed within $\pm 3\sigma$ from the Λ_c nominal mass, where the σ was obtained from the fitting of the distributions themselves.

The S/(S+B) ratio obtained as result of a fit is shown in Table D.1 for the three regions. In the low-mass background region this ratio is twice the one obtained for the flat background.

This corroborates the hypothesis of the physical origin of this "bump" and it is also plausible to attribute it to the $B_u^+ \rightarrow p\pi^+\pi^+\pi^-\pi^0\bar{\Lambda}_c^-$ decay, with its possible intermediate resonances, whose branching fraction is estimated to be $< 1.34\%$ in [1].

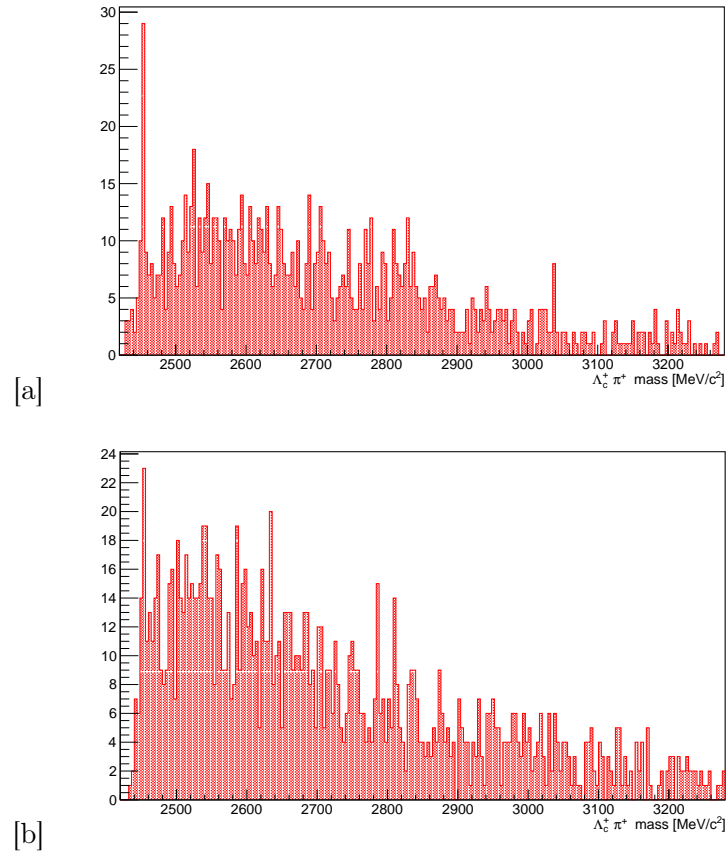


Figure D.1: Comparison between the $\Lambda_c^+ \pi^+$ invariant mass distribution for the low mass background region [a] and the flat background region.

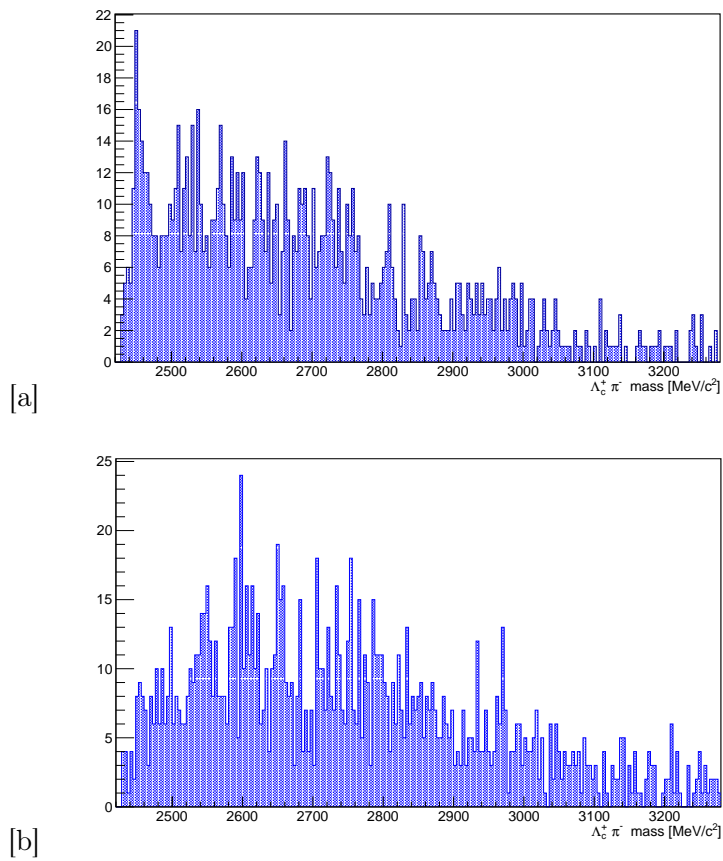


Figure D.2: Comparison between the $\Lambda_c^+ \pi^-$ invariant mass distribution for the low mass background region [a] and the flat background region.

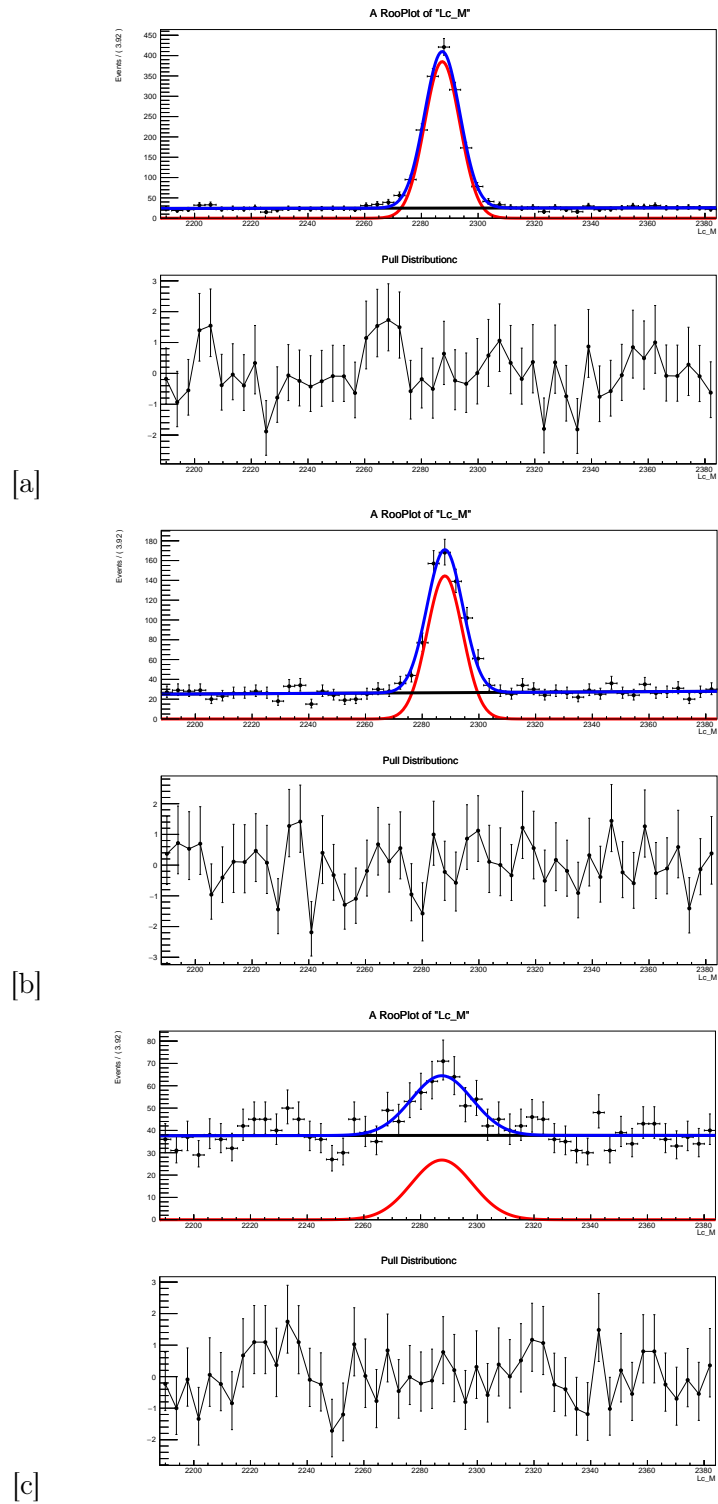


Figure D.3: Comparison between the Λ_c mass distribution for the signal region [a], the low mass background region [b] and the flat background region [c].

BIBLIOGRAPHY

- [1] K. A. Olive *et al.*, “Review of Particle Physics,” *Chin. Phys.*, vol. C38, p. 090001, 2014.
- [2] A. Contu, D. Fomesu, R. G. C. Oldeman, B. Saitta, and C. Vacca, “A method to measure the absolute branching fractions of Λ_c decays,” *The European Physical Journal C*, vol. 74, no. 12, p. 3194, 2014.
- [3] T. A. Collaboration, “The ATLAS Experiment at the CERN Large Hadron Collider,” *Journal of Instrumentation*, vol. 3, no. 08, p. S08003, 2008.
- [4] S. Chatrchyan *et al.*, “The CMS experiment at the CERN LHC,” *JINST*, vol. 3, p. S08004, 2008.
- [5] K. Aamodt *et al.*, “The ALICE experiment at the CERN LHC,” *JINST*, vol. 3, p. S08002, 2008.
- [6] A. A. Alves, Jr. *et al.*, “The LHCb Detector at the LHC,” *JINST*, vol. 3, p. S08005, 2008.
- [7] R. e. a. Aaji, “Measurement of b hadron production fractions in 7 TeV pp collisions,” *Phys. Rev. D*, vol. 85, p. 032008, Feb 2012.
- [8] R. e. a. Aaji, “Determination of the quark coupling strength $|V_{ub}|$ using baryonic decays,” *Nat. Phys.*, vol. 11, p. 032008, Sep 2015.
- [9] A. Zupanc *et al.*, “Measurement of the Branching Fraction $\mathcal{B}(\Lambda_c^+ \rightarrow pK^-\pi^+)$,” *Phys. Rev. Lett.*, vol. 113, no. 4, p. 042002, 2014.
- [10] T. B. et al., “Study of the decay $\Lambda_c \rightarrow \lambda l^+ \nu_l$,” *Physics Letters B*, vol. 323, no. 2, pp. 219 – 226, 1994.

- [11] H. A. et al., “Observations of Λ_c^+ semileptonic decay,” *Physics Letters B*, vol. 269, no. 1–2, pp. 234 – 242, 1991.
- [12] M. e. a. Ablikim, “Measurements of Absolute Hadronic Branching Fractions of the Λ_c^+ Baryon,” *Phys. Rev. Lett.*, vol. 116, p. 052001, Feb 2016.
- [13] L. Breiman, J. Friedman, R. Olshen, and C. Stone, *Classification and Regression Trees*. Monterey, CA: Wadsworth and Brooks, 1984.
- [14] R. Brun and F. Rademakers, “ROOT - An object oriented data analysis framework,” *Nuclear Instruments and Methods in Physics Research Section A: Accelerators, Spectrometers, Detectors and Associated Equipment*, vol. 389, no. 1, pp. 81 – 86, 1997.
- [15] A. Hoecker, P. Speckmayer, J. Stelzer, J. Therhaag, E. von Toerne, and H. Voss, “TMVA: Toolkit for Multivariate Data Analysis,” *PoS*, vol. ACAT, p. 040, 2007.
- [16] F. James and M. Roos, “MINUIT: a system for function minimization and analysis of the parameter errors and corrections,” *Comput. Phys. Commun.*, vol. 10, pp. 343–367. 38 p, Jul 1975.
- [17] T. Skwarnicki, *A study of the radiative CASCADE transitions between the Upsilon-Prime and Upsilon resonances*. PhD thesis, Cracow, INP, 1986.
- [18] L. Anderlini, A. Contu, C. R. Jones, S. S. Malde, D. Muller, S. Ogilvy, J. M. Otalora Goicochea, A. Pearce, I. Polyakov, W. Qian, B. Sciascia, R. Vazquez Gomez, and Y. Zhang, “The PIDCalib package,” Tech. Rep. LHCb-PUB-2016-021. CERN-LHCb-PUB-2016-021, CERN, Geneva, Jul 2016.
- [19] H. Albrecht *et al.*, “Observation of Inclusive B Meson Decays Into Λ_c^+ Baryons,” *Phys. Lett.*, vol. B210, pp. 263–266, 1988.
- [20] G. e. a. Crawford, “Measurement of baryon production in B -meson decay,” *Phys. Rev. D*, vol. 45, pp. 752–770, Feb 1992.
- [21] M. Suzuki, “Partial waves of baryon-antibaryon in three-body B meson decay,” *Journal of Physics G: Nuclear and Particle Physics*, vol. 34, no. 2, p. 283, 2007.
- [22] M. Jarfi, O. Lazrak, A. Le Yaouanc, L. Oliver, O. Pène, and J.-C. Raynal, “Pole model of B -meson decays into baryon-antibaryon pairs,” *Phys. Rev. D*, vol. 43, pp. 1599–1632, Mar 1991.
- [23] W. D. Hulsbergen, “Decay chain fitting with a Kalman filter,” *Nucl. Instrum. Meth.*, vol. A552, pp. 566–575, 2005.
- [24] S. Tolk, J. Albrecht, F. Dettori, and A. Pellegrino, “Data driven trigger efficiency determination at LHCb,” Tech. Rep. LHCb-PUB-2014-039. CERN-LHCb-PUB-2014-039, CERN, Geneva, May 2014.